Dissertation

submitted to the

Combined Faculty of Mathematics, Engineering and Natural Sciences

of Heidelberg University, Germany

for the degree of

Doctor of Natural Sciences

Put forward by

Antonia Schneider

born in: Mannheim

Oral examination: 06-07-2022

Measurement of the g-factors and zero-field hyperfine splitting of $^3He^+$ in a Penning trap

Referees: Prof. Dr. Klaus Blaum

Prof. Dr. Ulrich Uwer

Abstract

The ground-state hyperfine splitting of $^3He^+$ in a strong external magnetic field is investigated in a Penning-trap setup that was newly constructed in the context of this thesis. The nuclear g-factor of $^3He^+$ $g'_I = -4.255\,099\,606\,9(30)_{stat}(17)_{sys}$ was measured for the first time directly. This result is one order of magnitude more precise than previous indirect determinations and provides a calibration for ^3He NMR probes via the accurately calculated diamagnetic shielding parameters of $^3He^+$ and atomic ^3He. The experimental result for the bound electron g-factor of $^3He^+$ $g_e = -2.002\,177\,415\,79(34)_{stat}(30)_{sys}$ is consistent with the state-of-the-art theoretical value. Furthermore, the zero-field hyperfine splitting $E_{\mathrm{HFS}} = -8\,665\,649\,865.77(26)_{stat}(1)_{sys}$ Hz was extracted from the measurement and allows to calculate the Zemach radius $r_Z = 2.608(24)$ fm, which characterizes the electric and magnetic form factors of the nucleus.

Zusammenfassung

Die Hyperfeinstruktur des Grundzustandes von $^3He^+$ wurde in einem im Rahmen dieser Arbeit konstruierten Penningfallen-Aufbau untersucht. Der g-Faktor des Kerns von $^3He^+$ $g'_I = -4.255\,099\,606\,9(30)_{stat}(17)_{sys}$ wurde erstmalig direkt gemessen. Dieses Ergebnis stellt eine Verbesserung der Präzision um eine Größenordnung im Vergleich zu vorherigen indirekten Messungen dar und ermöglicht mithilfe der theoretisch exakt bestimmten Abschirmkonstanten von $^3He^+$ und atomarem ^3He die Kalibrierung von ^3He NMR Proben. Das experimentelle Ergebnis für den g-Faktor des gebundenen Elektrons in $^3He^+$ $g_e = -2.002\,177\,415\,79(34)_{stat}(30)_{sys}$ stimmt mit dem theoretisch Wert überein. Aus der gemessenen Hyperfeinkonstante $E_{\mathrm{HFS}} = -8\,665\,649\,865.77(26)_{stat}(1)_{sys}$ Hz folgt der Zemach Radius $r_Z = 2.608(24)$ fm, der die elektrischen und magnetischen Formfaktoren des Kerns charakterisiert.

Contents

List of Figures

List of Tables

Chapter 1

Motivation

Quantum-jump spectroscopy based on the continuous Stern-Gerlach effect in a Penning trap allows the measurement of the transition frequencies between the spin states of a single charged particle and the extraction of the corresponding g-factor. Applying this technique has led to the most precise measurement of the g-factors of free and bound electrons [1, 2], the positron [3], as well as the proton and anti-proton [4, 5]. These measurements probe free and bound-state quantum electrodynamics and through comparison of the g-factors of particles and anti-particles provide some of the most stringent constraints of CPT symmetry to date. This thesis discusses a newly constructed experiment which for the first time applies this technique to the $^3He^+$ ground-state hyperfine structure, leading to the first directly measured values for the nuclear g-factor of $^3He^+$, the zero-field hyperfine splitting and the bound electron g-factor.

Helium-3 can be hyper-polarized using laser optical pumping techniques, resulting in a very stable and sensitive probe to the magnetic field [6]. ^{3}He nuclear magnetic resonance (NMR) probes have been proposed as a new standard for high-precision absolute magnetometry [7, 8]. This application requires a high-accuracy value of the ^{3}He nuclear magnetic moment, which, however, has so far been determined indirectly and with a relative precision of 12 parts per billion (ppb), only [9, 10]. Combined with the accurately calculated shielding factors in ^{3}He [11], the measurement presented here provides the first direct calibration for ^{3}He probes independent of water probes and also improves the precision by one order of magnitude compared to the indirect results.

As opposed to superconducting quantum interference devices (SQUID), giant magnetoresistance sensors (GMR) or optical magnetometers, NMR probes allow measurements of the absolute magnetic field with high precision and ^{3}He NMR probes, in particular, offer a higher accuracy than standard water NMR probes. They require significantly smaller corrections due to systematic effects such as dependence on impurities, probe shape, temperature and pressure [8]. Moreover, the diamagnetic shielding σ of the bare

nuclear magnetic moment by the surrounding electrons is known more precisely for ^{3}He than water, for which it can only be measured. In case of atomic ^{3}He the factor $1-\sigma_{^3\mathrm{He}}$ correcting for the shielding by the two electrons has been calculated theoretically with a relative precision of 23 ppt [11]. Thus, ^{3}He probes with an independent high-precision calibration have a wide variety of possible applications including cryogenic NMR techniques for new experiments on the electron and positron magnetic moments [12, 13] and the muon $g-2$ experiments [14–16].

The muon $g-2$ experiments located at Fermilab and J-Parc are motivated by the 4σ discrepancy [16,17] between experimental and theoretical values of the muon's anomalous magnetic moment $a_\mu = (g_\mu - 2)/2$ as predicted by the Standard Model. Both experiments are based on the measurement of the anomaly frequency ω_a of the muon in a precisely tuned magnetic field [18] and the spin precession frequency ω_p' of protons in state-of-the-art water NMR probes [19] to extract a_μ via

$$a_\mu = \frac{\omega_a/\omega_p'}{\mu_\mu/\mu_p' - \omega_a/\omega_p'}, \tag{1.1}$$

aiming at an improved precision of 0.14 ppm. Here, all quantities on the right hand side of are determined experimentally, however, the experimental uncertainty of the ratio of the muon and shielded proton magnetic moments μ_μ/μ_p' is 0.12 ppm [20]. Alternatively, a_μ can be expressed without this factor as

$$a_\mu = \frac{g_e}{2}\frac{\omega_a}{\omega_{NMR}'}\frac{m_\mu}{m_e}\frac{\mu_{NMR}'}{\mu_e}, \tag{1.2}$$

where m_μ/m_e is the muon-to-electron mass ratio and g_e is the electron g-factor, which are known to 25 ppb and 0.76 ppt, respectively [1, 20]. Both of these approaches are applicable with water NMR probes, which using the independent value for the nuclear magnetic moment of ^{3}He presented here can now be calibrated using ^{3}He probes.
In the planned g-factor measurement of $^3\mathrm{He}^{2+}$ in a Penning trap [21, 22] the ratio

$$\frac{\omega_L}{\omega_c} = \mu_{^3\mathrm{He}}\left(\frac{q\hbar}{2m_{^3\mathrm{He}}}\right)^{-1} \tag{1.3}$$

will be determined directly and with high precision, so that the last factor in Eq. (1.2) follows from

$$\frac{\mu_{^3\mathrm{He}}'}{\mu_e} = \frac{m_u}{m_{^3\mathrm{He}}}\frac{m_e}{m_u}\frac{1}{g_e}(1-\sigma_{^3\mathrm{He}})\frac{\omega_L}{\omega_c}. \tag{1.4}$$

Here, m_u is the atomic mass unit so that the first two factors above are known to 14 ppt and 30 ppt, respectively [23, 24]. Thus, once the factor in Eq. (1.3) has been determined, this approach can be used for the determination of a_μ with ^{3}He NMR probes as an uncorrelated test of the results with water NMR probes.

Furthermore, the result presented in this thesis can be used to test diamagnetic shielding corrections in water by comparing the precisely measured ratio of ^{3}He and water NMR frequencies [9] to the ratio of the helion and proton magnetic moments [4]. The ratio of the molecular hydrogen and ^{3}He shielding parameters is

$$\frac{1-\sigma_{\mathrm{H2O}}}{1-\sigma_{\mathrm{3He}}} = \frac{\nu'_{\mathrm{H2O}}}{\nu'_{\mathrm{3He}}}\frac{\mu_{\mathrm{3He}}}{\mu_p}. \tag{1.5}$$

Here, ν'_{H_2} and $\nu'_{^3\mathrm{He}}$ are the nuclear resonance frequencies of molecular hydrogen and atomic ^{3}He, i.e. including electronic shielding.

Besides the nuclear magnetic moment, the zero-field hyperfine splitting is extracted from the measurement. Previously, the most precise measurement of the zero-field ground state hyperfine splitting of $^3\mathrm{He}^+$ studies the spin-dependent collision processes between a cloud of $^3\mathrm{He}^+$ ions stored in a radio-frequency quadrupole ion trap and a polarized beam of Cs atoms [25]. This measurement is limited to a relative precision of 10^{-9} by resonance line broadening due to the second order Doppler effect. For hydrogen-like systems the hyperfine splitting is given to leading order by the Fermi contact term E_F [26]. Corrections contributing to the energy splitting arise from QED effects δ_{QED}, the strong interaction δ_{hvp} and recoil effects δ_{rec}. In addition the nuclear polarizability as well as the spatial distribution of the charge and the magnetic moment within the nucleus δ_{nucl}, the latter known as Zemach radius, contribute:

$$\Delta E_{\mathrm{HFS}} = E_F(1+\delta_{\mathrm{QED}}+\delta_{\mathrm{rec}}+\delta_{\mathrm{hvp}}+\delta_{\mathrm{nucl}}). \tag{1.6}$$

The measurement of ΔE_{HFS} we are aiming for is highly sensitive to nuclear structure effects, as δ_{nucl} contributes at a relative precision of $2\cdot 10^{-4}$ and allows us to extract the Zemach radius.

Furthermore, the bound electron g-factor was measured with a precision of 6 ppb and agrees with the much more precise theoretical value, which serves as a systematic cross-check for the cyclotron measurement and therefore also the nuclear g-factor. If in the future the experimental uncertainty of g_e can be decreased by orders of magnitude a competitive determination of α would be possible, as He^+ is the only one-electron ion where uncertainties arising from nuclear structure are sufficiently small for this purpose [27].

This thesis is structured as follows: In chapter 2 the theoretical basics of the experiment are introduced, such as the working principle of Penning traps and the detection technique. Chapter 3 details the measurement procedure for the hyperfine structure of $^3\mathrm{He}^+$ in a Penning trap and the relevant transition lineshape. In chapter 4 the design of the cryogenic Penning-trap apparatus is described, including the internal ^{3}He source and microwave input. Chapter 5 discusses the characterization of the properties of the two

Penning traps used in the experiment. Finally, chapter 6 contains details on the data analysis and systematic effects, as well as the final results.

Chapter 2

Theoretical Background

2.1 Ideal Penning trap

An ideal Penning trap consists of a homogeneous magnetic field $\vec{B} = B_0\vec{e_z}$ in the axial direction and a superimposed quadrupolar electrostatic potential, which in cylindrical coordinates [z,ρ] is described by

$$V(z,\rho) = V_0 C_2 \left(z^2 - \frac{\rho^2}{2} \right). \tag{2.1}$$

Here, V_0 is the trapping voltage and C_2 characterizes the typical geometrical length scale of the potential. It can be created by hyperbolic electrodes as depicted in Fig. 2.1 (A). The electrostatic force $\vec{F_E} = -q\vec{\nabla}V$, acting on a trapped particle of mass m and charge q, leads to a harmonic oscillation in the axial direction with frequency

$$\nu_z = \frac{1}{2\pi}\sqrt{2\frac{q}{m}C_2 V_0}. \tag{2.2}$$

Radially, the particle is confined due to the Lorentz force $\vec{F_L} = q\vec{v} \times \vec{B}$, which in absence of the electric field would lead to a periodic circular orbit perpendicular to the magnetic field with the so-called free cyclotron frequency

$$\nu_c = \frac{1}{2\pi}\frac{q}{m}B_0. \tag{2.3}$$

Solving the equation of motion for the total force $\vec{F} = \vec{F_E} + \vec{F_L}$ leads to the two radial eigenfrequencies

$$\nu_\pm = \frac{1}{2}\left(\nu_c \pm \sqrt{\nu_c^2 - 2\nu_z^2}\right), \tag{2.4}$$

The magnetic and electric fields are typically chosen such that

$$\nu_c > \nu_+ \gg \nu_z \gg \nu_-. \tag{2.5}$$

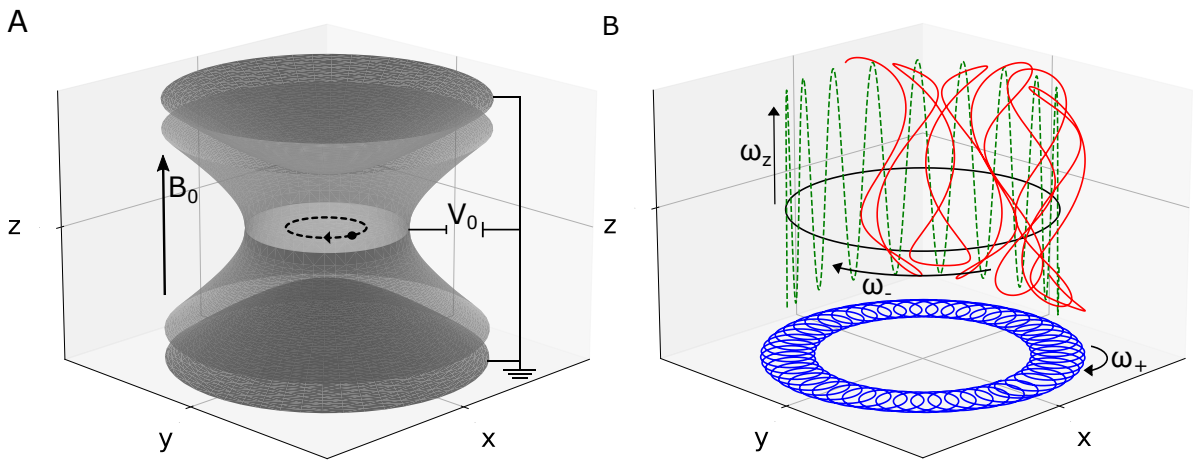

Figure 2.1. (A) Illustration of a Penning trap with hyperbolic electrodes placed in a magnetic field. (B) Trajectory of the trapped particle. The large black circle represents the magnetron motion with frequency ω_-. The superposition of the magnetron motion and the modified cyclotron motion with frequency ω_- is indicated by the blue line. Both radial motions are superimposed by the axial oscillation with frequency ω_z (red line).

A schematic of the three eigenmotions and their superposition is shown in Fig. 2.1 (B). the free cyclotron frequency follows from the eigenfrequencies via the so-called invariance theorem

$$\nu_c = \sqrt{\nu_+^2 + \nu_z^2 + \nu_-^2}, \tag{2.6}$$

where trap imperfections cancel to large extend [28]. In a g-factor measurement the invariance theorem is used to extract the magnetic field from the observable eigenfrequencies. Additionally the Larmor, or spin precession, frequency is determined, which for a spin 1/2 particle is

$$\nu_L = g\mu_{B/N} B_0/h. \tag{2.7}$$

Here, $\mu_{B/N}$ is the Bohr magneton or nuclear magneton in case of an electron or bare nuclear g-factor, respectively. Thus, for a single electron, positron or (anti-)proton the mass cancels in the ratio of both frequencies $g = 2\frac{\nu_L}{\nu_c}$, while for other particles the mass has to be inserted to determine the magnetic field.

Since the three eigenmotions are independent harmonic oscillators, the total energy of an ion in a Penning trap in the quantum mechanical picture is given by

$$E = \left(n_+ + \frac{1}{2}\right) h\nu_+ + \left(n_z + \frac{1}{2}\right) h\nu_z - \left(n_- + \frac{1}{2}\right) h\nu_- + m_s h\nu_L \tag{2.8}$$

where n_i is the quantum number of the corresponding motion and m_s the secondary spin quantum number. The magnetron energy $E_- = -\left(n_- + \frac{1}{2}\right) h\nu_-$ is dominated by potential energy and in the case of a reduction of motional quanta, e.g. through cooling

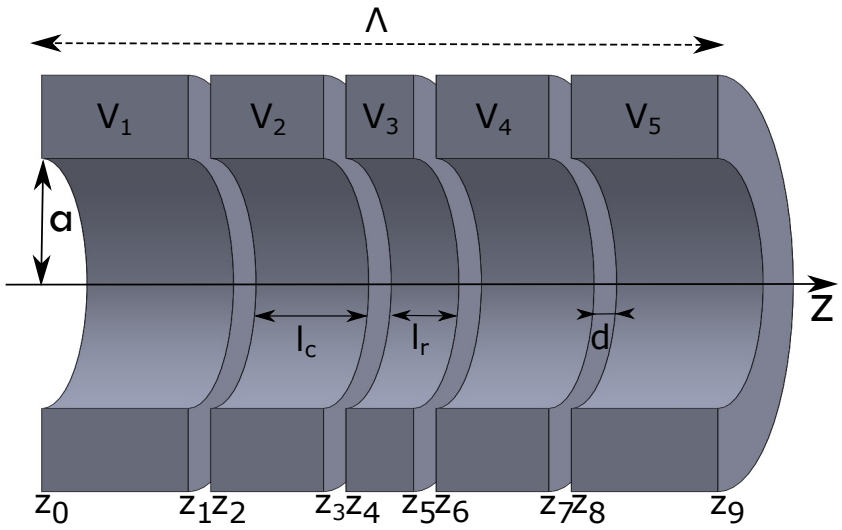

Figure 2.2. Sectional view of a Penning trap with five cylindrical electrodes, which create a quadrupolar electrostatic potential at the trap center if the voltages V_i and electrode lengths l_i are chosen appropriately.

mechanisms, the magnetron radius increases, i.e. the magnetron motion is metastable. At the temperatures reached through the cooling meachanisms described in Sec. 2.4.1, the quantum numbers are still on the order of 10^5 and allow a classical treatment of the ion motion. The axial energy E_z relates to the amplitude $z_{\max}$ of the axial motion via

$$E_z = \frac{1}{2} m\omega_z^2 z_{\max}^2 = m\omega_z^2 \langle z(t)^2 \rangle. \tag{2.9}$$

The axial motion is coupled to the detection system, which constitutes a heat bath and leads to a Boltzmann distributed amplitude $z_{\max}$, so that the axial temperature of the single particle can be defined via

$$\frac{1}{2} k_B T_z = \langle E_{\mathrm{z,kin}} \rangle = \frac{1}{2} \langle E_z \rangle \tag{2.10}$$

and thus

$$k_B T_z = m\omega_z^2 \langle z(t)^2 \rangle. \tag{2.11}$$

For the radial modes the radii follow from the mode energies through

$$E_\pm = \frac{1}{2} m\omega_\pm r_\pm^2 - \frac{1}{4} m\omega_z^2 r_\pm^2 \tag{2.12}$$

so that $E_- \approx -\frac{1}{4} m\omega_z^2 r_-^2$ and $E_+ \approx \frac{1}{2} m\omega_+ r_+^2$ and $k_B T_\pm = \langle E_\pm \rangle$ as above.

2.2 Cylindrical Penning trap

In practice, the axial potential is created by a stack of cylindrical electrodes [29], which compared to hyperbolic electrodes are easier to construct with high precision. A typical

five-polar trap consists of a central ring electrode with voltage V_0 surrounded by two identical correction electrodes with voltage V_c and two endcaps connected to ground, see Fig. 2.2. The voltages applied to the electrodes of inner radius a constitute Dirichlet boundary conditions $V(a,z)$ to the solution of the cylindrical Laplace equation in free space

$$0 = \nabla^2 V(z,\rho). \tag{2.13}$$

From the separation ansatz $V(z,\rho) = V_\rho(\rho)V_z(z)$ follows the solution

$$V(z,\rho) = \sum_{n=1}^{\infty} I_0(k_n\rho)A_n\cos(k_n z), \tag{2.14}$$

with the Bessel functions of first kind $I_m(\rho)$, the total trap length Λ and $k_n = \frac{n\pi}{\Lambda}$. The coefficients A_n follow from the boundary conditions by calculating $\int_0^\Lambda V(z,a)$, where the potential in the spacing d between neighbouring electrodes is linearly interpolated:

$$A_n = \frac{2}{\Lambda I_0(k_n a)}\left(\frac{V_1\cos(k_n z_0) - V_5\cos(k_n\Lambda)}{k_n} + \sum_{i=1}^{4}\frac{V_{i+1}-V_i}{k_n^2 d}(\sin(k_n z_{2i}) - \sin(k_n z_{2i-1}))\right). \tag{2.15}$$

The expansion of the potential in powers of the axial coordinate around the trap center is given by

$$V(z,0) = V_0\sum_j C_j z^j \tag{2.16}$$

with the coefficients

$$C_j = \frac{1}{j!V_0}\sum_n A_n\left(\frac{n\pi}{\Lambda}\right)^j \sin\left(\frac{\pi}{2}(n+j)\right). \tag{2.17}$$

In an ideal trap with symmetric electrode lengths and potentials $V_2 = V_4 = V_c$, $V_1 = V_5 = 0$ the coefficients C_j with odd j vanish. By choosing adequate electrode lengths, the trap can be designed to be "compensated" as well as "orthogonal". Compensation means that the first higher order corrections C_4 and C_6 of the multipolar potential expansion vanish at the same tuning ratio, defined as the ratio of the ring voltage and correction voltage:

$$TR = \frac{V_c}{V_0}. \tag{2.18}$$

Orthogonality means that the axial frequency ν_z of the particle is independent of the voltage applied to the correction electrodes, i.e. $D_2 = \frac{\partial\nu_z}{\partial TR} = 0$.

2.3 Field imperfections

The first anharmonic contributions to the electrostatic potential in a symmetric trap are determined by C_4 and C_6 and change the simple harmonic equation to a Duffing type

differential equation

$$\ddot{z} = -\frac{q}{m}\partial_z \left(V_0 \sum_{j=1}^{\infty} C_{2j} z^{2j} \right) = -\omega_z^2 (z + 2C_4/C_2 z^3 + 3C_6/C_2 z^5), \tag{2.19}$$

giving rise to energy dependent shifts of the axial frequency. Using a perturbation theory approach [30] the energy dependent shifts can be determined for the three eigenfrequencies:

$$\begin{pmatrix} \Delta\nu_+/\nu_+ \\ \Delta\nu_z/\nu_z \\ \Delta\nu_-/\nu_- \end{pmatrix} = \frac{3}{qV_0}\frac{C_4}{C_2^2} \begin{pmatrix} \frac{1}{4}\Omega^4 & -\frac{1}{2}\Omega^2 & -\Omega^2 \\ -\frac{1}{2}\Omega^2 & \frac{1}{4} & 1 \\ -\Omega^2 & 1 & 1 \end{pmatrix} \begin{pmatrix} E_+ \\ E_z \\ E_- \end{pmatrix}. \tag{2.20}$$

$$\begin{pmatrix} \Delta\nu_+/\nu_+ \\ \Delta\nu_z/\nu_z \\ \Delta\nu_-/\nu_- \end{pmatrix} = \frac{45}{16q^2V_0^2}\frac{C_6}{C_2^3} \begin{pmatrix} -\frac{1}{3}\Omega^6 & -\Omega^2 & -4\Omega^2 & 2\Omega^4 & 4\Omega^2 & -8\Omega^2 \\ \Omega^4 & \frac{1}{3} & 4 & -\frac{1}{2}\Omega^2 & -8\Omega^2 & 4 \\ 2\Omega^4 & 2 & \frac{8}{3} & -8\Omega^2 & -8\Omega^2 & 8 \end{pmatrix} \begin{pmatrix} E_+^2 \\ E_z^2 \\ E_-^2 \\ E_+E_z \\ E_+E_- \\ E_zE_- \end{pmatrix}. \tag{2.21}$$

Here, $\Omega = \nu_z/\nu_+$ is used. In order to quantify frequency shifts due to magnetic field imperfections, the magnetic field can be expanded into a polynomial

$$B(z) = \sum_{i=0}^{\infty} B_i^i z^i. \tag{2.22}$$

The radial modes with angular momenta $L_\pm$ produce magnetic moments in the axial direction

$$\vec{\mu}_\pm = \frac{q}{2m}\vec{L}_\pm = -q\rho_\pm^2 \pi \nu_\pm \vec{e}_z, \tag{2.23}$$

which lead to the additional force $F_z = \partial_z \left(\vec{\mu}_\pm \cdot \vec{B}(z) \right)$. Thus, B_1 shifts the central position of the ion in the trap by

$$\Delta z = \frac{-\mu_\pm B_1}{2qV_0C_2}, \tag{2.24}$$

while leaving the axial frequency unchanged. The second order contribution $F_z = -2zB_2\mu_\pm$ shifts the axial frequency by

$$\Delta\omega_z = \left(\sqrt{1 + \frac{2B_2\mu_\pm}{m\omega_z^2}} - 1 \right) \omega_z \approx \frac{B_2}{\omega_z}\frac{\mu_\pm}{m}. \tag{2.25}$$

All eigenfrequency shifts resulting from a quadratic inhomogeneity B_2 are given by [30]

$$\begin{pmatrix} \Delta\nu_+/\nu_+ \\ \Delta\nu_z/\nu_z \\ \Delta\nu_-/\nu_- \end{pmatrix} = \frac{1}{(2\pi\nu_z)^2 m}\frac{B_2}{B_0} \begin{pmatrix} -\Omega^2 & 1 & 2 \\ 1 & 0 & -1 \\ 2 & -1 & -2 \end{pmatrix} \begin{pmatrix} E_+ \\ E_z \\ E_- \end{pmatrix}. \tag{2.26}$$

2.4 Detection principle

The trapped particle's oscillation induces image charges in the trapping electrodes that can be read out by a current detector in order to non-destructively detect the particle's eigenfrequencies. The induced current for the axial motion

$$I = \frac{q}{D}\dot{z}, \tag{2.27}$$

depends on the particle's charge q and the effective electrode distance D, which follows from the trap geometry. If the axial signal is picked up on one of the correction electrodes of a cylindrical trap the effective electrode distance is given by [31]

$$D_z = \frac{\Lambda}{4}\left(\sum_n \sin(k_n l_c)\sin(k_n(l_c + l_e + 2d))/I_0(2k_n a)\right). \tag{2.28}$$

A superconducting coil is connected in parallel to the trap (Fig. 2.3) so that the coil's inductance L_{res}, self-capacitance C_{res}, effective resistance R_p and the trap capacitance C_T form an RLC circuit with resonance frequency

$$\omega_{res} = \frac{1}{\sqrt{L_{res}(C_T + C_{res})}}. \tag{2.29}$$

At ω_{res} the total resistance of the resonator $Z_{res} = \left(R_p^{-1} + (i\omega L_{res})^{-1} + i\omega(C_{res} + C_T)\right)^{-1}$ approaches $R_p = Q\omega_{res}L_{res}$. Here, Q is the quality factor of the tank circuit $Q = \omega_{res}/\Delta\omega$, experimentally accessible via the 3db-width $\Delta\omega$.

The trapped particle induces the voltage $U = Z_{res}(\omega)I$ in the trap electrodes, which leads to an additional term $F = -\frac{q}{D}U$ in the equation of motion (EOM). By inserting Eq. (2.27), this leads to the EOM of a damped harmonic oscillator

$$\ddot{z} + \gamma\dot{z} + \omega_0^2 z = 0, \tag{2.30}$$

with damping constant $\gamma(\omega) = q^2/(mD^2)Z_{res}(\omega)$, and thus cooling time constant $\tau(\omega) = 1/\,\mathbb{R}(\gamma(\omega))$. On resonance, the imaginary part of the damping constant vanishes and the shift of the eigenfrequency $\omega' = \sqrt{\omega_0^2 - \gamma^2/4} \approx \omega_0$ is negligible, while off resonance the imaginary part leads to the image current shift described in Sec. 6.3.

By inserting Eq. (2.27), the EOM can be expressed in terms of the induced current and takes the form of the differential equation of a series RLC circuit $L_{ion}\ddot{I} + Z_{res}\dot{I} + I/C_{ion} = 0$ with an effective capacitance and inductance of the ion:

$$C_{ion} = q^2/(\omega_z^2 mD^2) \qquad L_{ion} = mD^2/q^2. \tag{2.31}$$

The total resistance of the equivalent circuit (Fig. 2.3) is

$$Z_{tot} = \left(\frac{1}{i\omega L_{ion} + (i\omega C_{ion})^{-1}} + \frac{1}{Z_{res}}\right)^{-1} \tag{2.32}$$

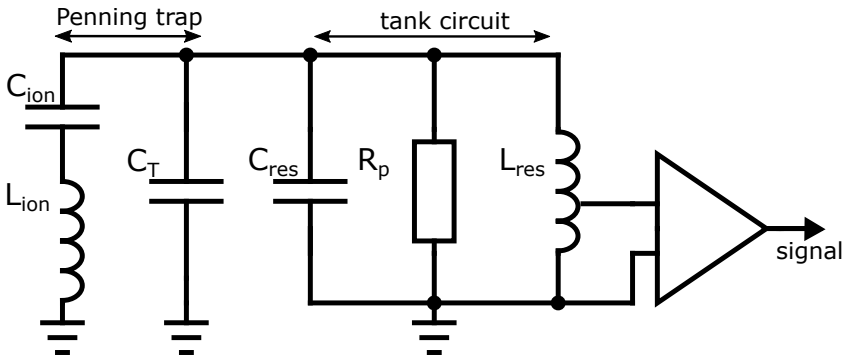

Figure 2.3. Schematic of particle detection in a Penning trap. The particle can be described by an effective inductance and capacitance L_{ion} and C_{ion}. The tank circuit consists of an inductance L_{res}, an effective resistance R_p and a parasitic capacitance C_{res}. The signal is coupled to a cryogenic amplifier.

with real part

$$\mathbb{R}(Z_{tot}) = R_p \left(1 + \left(\frac{\omega}{\tau(\omega^2 - \omega_z^2)} - Q\left(\frac{\omega}{\omega_{res}} - \frac{\omega_{res}}{\omega}\right)\right)^2\right), \tag{2.33}$$

where $\omega_z = 1/\sqrt{L_{ion}C_{ion}}$ was used. On resonance the particle acts as a short or dip with bandwidth $\Delta\omega = 1/\tau$.

2.4.1 Sideband coupling

In order to cool the radial modes and measure the radial eigenfrequencies $\omega_\pm$, an external driving field E_{RF} with frequency $\omega_{RF} = \omega_\pm \mp \omega_z$ is applied, which near the center of the trap is to lowest order given by

$$\vec{E}_{RF} = E_0 \cos(\omega_{RF} t)(z\vec{e}_x + x\vec{e}_z). \tag{2.34}$$

The resulting force $q\vec{E}_{RF}$ leads to two coupled simple harmonic oscillators and thus an energy exchange between axial and radial mode with the Rabi-frequency [32]

$$\Omega = \frac{qE_0}{2m\sqrt{\omega_z\omega_\pm}}. \tag{2.35}$$

The amplitude modulation of the axial mode $z(t) = z_0 \sin(\Omega t/2)\sin(\omega_z t + \phi_0)$ corresponds to two modified eigenfrequencies $\omega_{l/r} = \omega_z \mp \Omega/2$, so that two dips are observed in the noise spectrum of the axial resonator ("double-dip"). In case of an off-resonant excitation with frequency $\omega_{RF} = \omega_\pm \mp \omega_z + \delta$ these eigenfrequencies depend on the detuning δ:

$$\omega_l = \omega_z \mp \delta/2 - \sqrt{\Omega^2 + \delta^2}/2, \qquad \omega_r = \omega_z \mp \delta/2 + \sqrt{\Omega^2 + \delta^2}/2. \tag{2.36}$$

By measuring the double-dip frequencies, $\omega_\pm$ can be experimentally determined using

$$\omega_\pm = \pm\omega_l \pm \omega_r \mp \omega_z + \omega_{RF}, \tag{2.37}$$

where the shifts due to the detuning cancel.

The interaction with the photon of frequency ω_{RF} allows the transition $|n_z, n_\pm\rangle \rightarrow |n_z - 1, n_\pm \pm 1\rangle$, which heats the radial mode, or the transition $|n_z, n_\pm\rangle \rightarrow |n_z + 1, n_\mp \pm 1\rangle$, which cools the radial mode. While $n_\pm > n_z$, the rate of the latter transition dominates [33], so that in thermal equilibrium the quantum numbers of the coupled modes are equal $n_\pm = n_z$. As the axial mode is thermalized to the temperature T_z of the axial resonator $\hbar\omega_z\langle n_z\rangle = k_B T_z$, the energy of the radial mode is Boltzmann distributed with $\langle E_\pm\rangle = \pm\omega_\pm/\omega_z k_B T_z$.

2.4.2 Continuous Stern-Gerlach effect

Measuring the resonance frequencies of the hyperfine transitions requires determining the spin state, which can be achieved via the continuous Stern-Gerlach effect [34], i.e. the coupling of the spin magnetic moment to the axial frequency. For this purpose a magnetic bottle B_2 is superimposed on the homogeneous background field resulting in the total magnetic field

$$\vec{B}(z,\rho) = B_0\vec{e_z} + B_2\left(\left(z^2 - \frac{\rho^2}{2}\right)\vec{e_z} - \rho z\vec{e_\rho}\right). \tag{2.38}$$

As described in Sec. 2.3 the axial frequency is then shifted by

$$\Delta\nu_z \approx \frac{B_2}{4\pi^2\nu_z}\frac{\Delta\mu_z}{m_{\mathrm{He}}}, \tag{2.39}$$

where $\Delta\mu_z$ is the change is the z-component of the ion's magnetic moment $\mu_z = \mu_{z,s} + \mu_{z,+} + \mu_{z,-}$ that consists of the contributions from the total spin angular momentum and the two orbital angular momenta $\mu_\pm = E_\pm/B_0$. For a single spin 1/2 particle without hyperfine structure such as $^3He^{2+}$ this computes to

$$\Delta\nu_{\mathrm{z,SF}} = \pm\frac{h\nu_L}{4\pi^2 m\nu_z}\frac{B_2}{B_0}, \tag{2.40}$$

with Larmor frequency ν_L. The case of a hyperfine transition in $^3He^+$ is described in more detail in Sec. 3.1.

The magnetic bottle is created by placing a ferromagnetic electrode in one of the Penning traps, the analysis trap (AT), where the magnetic inhomogeneity allows for spin-state detection by detecting the axial frequency shift, while limiting the precision with which the ion's eigenfrequencies and the transition frequencies can be measured due to line-broadening [35]. The AT is therefore separated by several transport electrodes from the precision trap (PT), in which the magnetic inhomogeneity is sufficiently small to detect these frequencies with high precision.

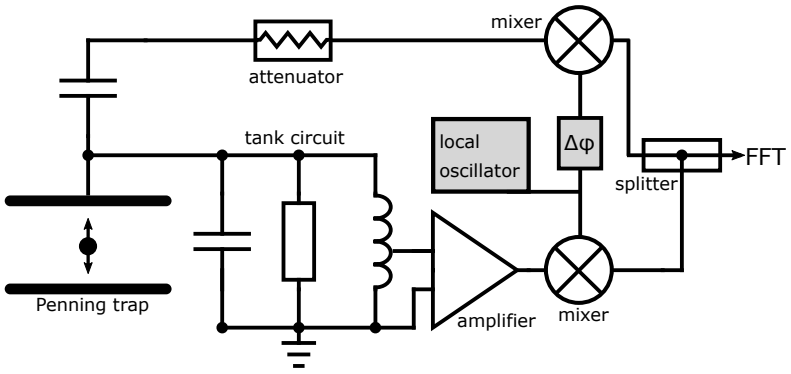

Figure 2.4. Schematic of active particle-temperature control using phase shifted feedback. The signal is amplified and phase-shifted and fed back. The feedback gain is adjusted with an attenuator.

2.4.3 Controlled feedback

Electronic feedback [36, 37] can be used to change the effective temperature of the detection system. Part of the signal is phase-shifted and fed back to the trap via weak capacitive coupling. The temperature is decreased and increased with negative or positive feedback, respectively. The gain is adapted using an attenuator, see Fig. 2.4. The temperatures with and without feedback, T_{FB} and T_0, are related to the quality factors as follows:

$$\frac{T_{FB}}{T_0} = \frac{Q_{FB}}{Q_0}. \tag{2.41}$$

The lowest achievable temperature is limited by the noise added by the amplifier, which causes additional heating.

Chapter 3

g-Factor and E_{HFS} Measurement Principle

3.1 Hyperfine states of $^3He^+$ in an external magnetic field

The hyperfine splitting of the level structure of an atom or ion with non-vanishing nuclear spin is due to the interaction of the spin magnetic moment of the nucleus with the total magnetic moment of the electrons. For a hydrogen-like system with electronic orbital angular momentum $L = 0$, which is exposed to an external magnetic field $\vec{B}$, the Hamiltonian up to linear-order Zeeman effect then reads [38]

$$H = A\,(\vec{\sigma_e} \cdot \vec{\sigma_I}) - (\mu_e \vec{\sigma_e} + \mu_I \vec{\sigma_I})\,\vec{B}. \tag{3.1}$$

Here, A is a constant describing the spin-spin interaction, which is negative in case of $^3He^+$ due to its negative nuclear magnetic moment. $\vec{\sigma_I}$ and $\vec{\sigma_e}$ are the Pauli matrices $\vec{\sigma_{I/e}} = \sigma_{x,I/e}\vec{e}_x + \sigma_{y,I/e}\vec{e}_y + \sigma_{z,I/e}\vec{e}_z$ referring to the nuclear or electronic spin, respectively, and μ_I and μ_e the nuclear and electron spin magnetic moment. The latter are given by $\mu_e = g_e\mu_B/2$ and $\mu_I = g'_I\mu_B/2$, where μ_B and μ_N are the Bohr magneton and nuclear magneton. In the ion, the diamagnetic shielding of the nucleus by the electron effectively modifies the bare nuclear g-factor g_I to the shielded nuclear g-factor $g'_I = g_I(1-\sigma_{^3He^+})$. The shielding constant and the bound electron g-factor can calculated theoretically with high accuracy [11,39]. Expressed in the basis $\{|{+}{+}\rangle, |{+}{-}\rangle, |{-}{+}\rangle, |{-}{-}\rangle\}$, where $|m_j, m_I\rangle = |m_j\rangle \otimes |m_I\rangle$ is a product state of electron and nuclear spin state with $|+\rangle$ or $|-\rangle$ denoting spin up or

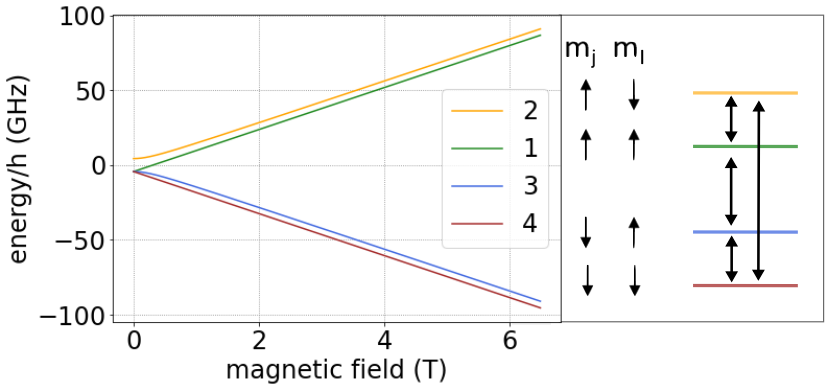

Figure 3.1. Energies of the hyperfine states E_1, E_2, E_3 and E_4 as function of the magnetic field according to Eq. (3.4). The four double-headed arrows indicate the hyperfine transitions measured in this work.

spin down, the Hamiltonian above reads:

$$H = \begin{pmatrix} A + B\mu & 0 & 0 & 0 \\ 0 & -A + B\mu' & 2A & 0 \\ 0 & 2A & -A - B\mu' & 0 \\ 0 & 0 & 0 & A - B\mu \end{pmatrix}, \tag{3.2}$$

using the abbreviations $\mu = -(\mu_e + \mu_I)$ and $\mu' = -\mu_e + \mu_I$. By diagonalizing this Hamiltonian one finds the eigenstates

$$|1\rangle = |{+}{+}\rangle\,, \quad |2\rangle = r_+\,|{-}{+}\rangle - r_-\,|{+}{-}\rangle\,, \quad |3\rangle = r_-\,|{-}{+}\rangle + r_+\,|{+}{-}\rangle\,, \quad |4\rangle = |{-}{-}\rangle\,, \tag{3.3}$$

where $r_\pm = \sqrt{(1 \pm \tanh(\theta))/2}$ and $\sinh(\theta) = B\mu'/(2A)$ was defined. The corresponding eigenenergies (Breit-Rabi equation) are:

$$E_{1,4} = A \mp (\mu_I B + \mu_e B)\,, \quad E_{2,3} = -A \pm 2\sqrt{A^2 + \frac{1}{4}(\mu_e B - \mu_I B)^2}\,. \tag{3.4}$$

Thus, the hyperfine splitting at zero magnetic field is $E_{\mathrm{HFS}} = 4A < 0$, using the definition $E_{\mathrm{HFS}} = E(F = 1) - E(F = 0)$ with total angular momentum quantum number F. Corrections due to the quadratic Zeeman shift are identical for all states involved and have therefore no influence on the transition frequencies [40]. For large magnetic fields the factor r_- in Eq. (3.3) approaches 1 while r_+ vanishes. At the magnetic field 5.72 T in the experiment, they evaluate to $r_+ = 0.0270$ and $r_- = 0.9996$, so that $|2\rangle \approx |{+}{-}\rangle$ and $|3\rangle \approx |{+}{-}\rangle$, see also Fig. 3.1. Accordingly, the transitions $|1\rangle \leftrightarrow |2\rangle$ and $|3\rangle \leftrightarrow |4\rangle$ are referred to as nuclear transitions and the transitions $|1\rangle \leftrightarrow |3\rangle$ and $|2\rangle \leftrightarrow |4\rangle$ as electronic transitions. Using the Breit-Rabi formula, one can extract the two parameters g_I' and E_{HFS} from the combined fit to the resonance curves of both nuclear transitions and g_e from one of the electronic transition.

A magnetic bottle with $B(t) = B_0 + B_2 z(t)^2$ results in an additional contribution to the Hamiltonian above [41]

$$H_{B_2} = -B_2 z(t)^2 \begin{pmatrix} -\mu & 0 & 0 & 0 \\ 0 & \tanh(\theta)\mu' & 2r_+ r_- \mu' & 0 \\ 0 & 2r_+ r_- \mu' & -\tanh(\theta)\mu' & 0 \\ 0 & 0 & 0 & \mu \end{pmatrix}, \tag{3.5}$$

expressed in the basis $\{|1\rangle, |2\rangle, |3\rangle, |4\rangle\}$. With the the diagonal entries $\mu_i \, (i = 1, ..., 4)$, the axial frequency shift in case of a hyperfine transition $|i\rangle \leftrightarrow |j\rangle$ thus follows from $\Delta\mu = \mu_i - \mu_j$ in Eq. (2.39). With an inhomogeneity of $B_2 = 110 \text{ kT m}^{-2}$ in the analysis trap, an electronic or nuclear transition leads to a $\Delta\nu_z = \pm 22$ Hz or $\Delta\nu_z = \pm 43$ mHz jump of the axial frequency, respectively.

3.2 Nuclear spin state detection scheme

Direct detection of nuclear spin-flips has so far been demonstrated only for protons and anti-protons [4, 5]. Compared to a proton, ^{3}He has a larger mass and smaller nuclear magnetic moment so that the axial frequency jump indicating a spin-flip is smaller by a factor of 4 and not detectable using state of the art techniques. Broadband voltage noise on the trap electrodes [42, 43] induce cyclotron quantum number jumps which according to Eq. (2.39) lead to axial frequency fluctuations. As the angular momentum due to the radial motion is $\mu_\pm = E_\pm / B_0 \propto n_\pm$, this noise can be suppressed by reducing the cyclotron energy E_+. In the case of $^3\text{He}^{2+}$, deterministic sympathetic laser cooling [44] to much lower temperatures than by state of the art techniques would be necessary.
However, in case of $^3\text{He}^+$ a novel method can be employed which deduces the nuclear spin state from more easily detectable electronic transitions. As shown in Fig. 3.1, if the ion is in hyperfine state $|1\rangle$ or $|3\rangle$ the nuclear spin state is $|\uparrow\rangle$, while states $|2\rangle$ and $|4\rangle$ imply that the nuclear spin state is $|\downarrow\rangle$. Thus, depending on the nuclear state only one of the two electronic transitions $|1\rangle \leftrightarrow |3\rangle$ and $|2\rangle \leftrightarrow |4\rangle$ can be driven. In the experiment at 5.7 T, these transitions are separated by several GHz and thus easy to distinguish. The nuclear state can therefore be found by exciting both electronic transitions alternatingly until a spin-flip occurs.
A measurement cycle starts with determining the initial hyperfine state in the AT. The ion is then transported adiabatically to the PT, where the cyclotron frequency is first measured to determine the expected hyperfine transition frequency. It is afterwards measured again while a microwave excitation drives one of the four hyperfine transitions at a random frequency offset with respect to the expected resonance frequency. Whether

a spin-flip was successfully driven in the PT is then assessed after transporting the ion back to the AT. This process is repeated several hundred times for each of the four transitions so as to measure the spin-flip probability in the magnetic field of the PT as a function of the microwave frequency offset.

3.3 Transition lineshape

In the quadratic magnetic inhomogeneity B_2 the axial oscillation $z(t)$ leads to a time-dependent shift $\delta\omega_{ij}(t)$ of the resonance frequency ω_{ij} of the HFS transition $|i\rangle \leftrightarrow |j\rangle$

$$\delta\omega_{ij} = z(t)^2 B_2(\mu_i - \mu_j) \tag{3.6}$$

with μ_i as given above. The average is the linewidth parameter

$$\Delta\omega_{ij} = \langle z(t)^2\rangle B_2(\mu_i - \mu_j) = \frac{k_B T_z}{m\omega_z^2} B_2(\mu_i - \mu_j), \tag{3.7}$$

with the axial temperature T_z according to Eq. (2.11). The spin-state transition probability $P_{1/2}(\Delta_{MW})$ as a function of the detuning

$$\Delta_{MW} = \omega_{MW} - \omega_{ij}(B_0) \tag{3.8}$$

of the applied drive frequency ω_{MW} from the resonance frequency $\omega_{ij}(B_0)$ for the magnetic field at $z = 0$ is derived in [45] to be

$$P_{SF}(\Delta_{MW}) = \frac{1}{2}\left(1 - e^{-\pi\Omega^2 T_{\mathrm{exc}}\chi(\Delta_{MW})}\right). \tag{3.9}$$

Here, Ω is the Rabi frequency and T_{exc} the excitation time. The lineshape χ is defined as the Fourier transform

$$\chi(\Delta_{MW}) = \frac{1}{2\pi}\int_{-\infty}^{\infty} \exp(i\Delta_{MW}t)\tilde{\chi}(t)\,dt \tag{3.10}$$

of the correlation function

$$\tilde{\chi}(t) = \left\langle \exp\left(i\int_0^t \delta\omega(t')\,dt'\right)\right\rangle, \tag{3.11}$$

where the angle brackets denote a statistical averaging over the random axial amplitude. In [45] the general result

$$\chi_1(\Delta_{MW}, \gamma, \Delta\omega) = \frac{4}{\pi}\,\mathbb{R}\left(\frac{\gamma'\gamma}{(\gamma'+\gamma)^2}\sum_{n=0}^{\infty}\left(\frac{\gamma'-\gamma}{\gamma'+\gamma}\right)^{2n}\frac{1}{(n+0.5)\gamma' - 0.5\gamma - i\Delta_{MW}}\right) \tag{3.12}$$

is derived, where $\gamma' = \sqrt{\gamma^2 + i4\gamma\Delta\omega}$ and γ is the coupling of the ion to the resonator. This expression can be simplified in the cases of strong coupling $\Delta\omega/\gamma \ll 1$, which is fulfilled for nuclear transitions in the PT, as

$$\chi_1(\Delta_{MW}, \Delta\omega) = \delta(\Delta_{MW} - \Delta\omega) \tag{3.13}$$

or weak coupling $\Delta\omega/\gamma \gg 1$, which is fulfilled for nuclear and electronic transitions in the large magnetic bottle of the analysis trap, as

$$\chi_1(\Delta_{MW}, \Delta\omega) = \frac{\theta(\Delta_{MW})}{\Delta\omega} \exp\left(-\frac{\Delta_{MW}}{\Delta\omega}\right). \tag{3.14}$$

An alternate derivation is given in [46], where the probability for a spin-flip after time t is described by the Rabi-equation

$$P(\Delta) = \frac{\Omega^2}{\Omega^2 + \Delta^2} \sin^2\left(\frac{t}{2}\sqrt{\Omega^2 + \Delta^2}\right), \tag{3.15}$$

replacing the sine function by the average 1/2 as the transition is driven incoherently. Because of the magnetic inhomogeneity the detuning is shifted in dependence on the axial energy

$$\begin{aligned} \Delta(E_z) &= \omega_{MW} - (\omega_{ij}(B_0) + \delta\omega) \\ &= \omega_{MW} - \left(\omega_{ij}(B_0) + \Delta\omega\frac{E_z}{k_B T_z}\right), \end{aligned} \tag{3.16}$$

so that the above expression for P is convoluted with the Boltzmann-distribution of the axial energy due to the coupling to the resonator:

$$\chi'(\Delta) = \frac{1}{2k_B T_z} \int_0^\infty \exp\left(\frac{-E_z}{k_B T_z}\right) \frac{\Omega^2}{\Omega^2 + \Delta(E_z)^2}\, dE_z. \tag{3.17}$$

Using the lower incomplete gamma function

$$\Gamma(a, x) = \int_x^\infty t^{a-1} e^t\, dt \tag{3.18}$$

the integral above can be expressed as

$$\chi'(\Delta_{MW}, \Omega, \Delta\omega) = \frac{b}{4}\, \mathbb{R}\left(ie^{b(i-a)}\Gamma(0, b(i-a)) - ie^{-b(i+a)}\Gamma(0, -b(i+a))\right), \tag{3.19}$$

defining $a = \Delta_{MW}/\Omega$ and $b = \Omega/\Delta\omega$. The lineshape χ in Eq. (3.9) then is

$$\chi_2(\Delta_{MW}, \Omega, \Delta\omega) = 2/(\pi\Omega)\chi'(\Delta_{MW}, \Omega, \Delta\omega) \tag{3.20}$$

with the normalization

$$\int_{-\infty}^{\infty} \chi(\Delta_{MW}, \Omega)\, d\Delta_{MW} = 1. \tag{3.21}$$

The magnetic field B_{meas} follows from the double-dip measurement during which the magnetic bottle shifts the average magnetic field by $\delta\nu_+/\nu_+ = \langle z^2\rangle B_2/B_0$ (compare Eq. (2.26)) so that $\omega_{ij}(B_{\mathrm{meas}}) = \omega_{ij}(B_0) + \Delta\omega$ and thus

$$\Delta_{MW} = \omega_{MW} - \omega_{ij}(B_0) = \omega_{MW} - \omega_{ij}(B_{\mathrm{meas}}) + \Delta\omega \tag{3.22}$$

is inserted in Eq. (3.9). Furthermore, the measured cyclotron frequency is normally distributed with a relative width of $\sigma_B/B_0 = 1.7{\cdot}10^{-9}$. The underlying function describing the spin-flip probability is therefore convoluted with the Gaussian of the magnetic field measurement:

$$\begin{aligned}\tilde{P}_{SF}(\omega_{MW}, \omega_{ij}(B_{\mathrm{meas}}), \Omega, \Delta\omega) =& \frac{1}{\sqrt{2\pi}\sigma_B}\int_{-\infty}^{\infty} P_{SF}(\omega_{MW} - \omega_{ij}(B_{\mathrm{meas}}) + \Delta\omega - y, \Omega) \\ & \times \exp\left(\frac{-(y/\omega'_{ij})^2}{2\sigma_B^2}\right)\frac{dy}{\omega'_{ij}}\,.\end{aligned} \tag{3.23}$$

Here, ω'_{ij} is the derivative $\omega'_{ij} = d\omega_{ij}/dB(B_0)$ for transition $|i\rangle \leftrightarrow |j\rangle$. The two lineshape models and spin-flip probabilities are plotted in Figs. 3.2, 3.3 and 3.4 for the trap parameters γ and B_2 in the AT and PT and Rabi-frequencies used in the experiment. For low Rabi frequencies the jitter of the magnetic field measurement dominates and the spin-flip probability $\tilde{P}$ for both lineshape models approaches a Gaussian centered at $\omega_{MW} - \omega_{ij}(B_{\mathrm{meas}}) = 0$, see Fig. 3.2 (E) and (F).

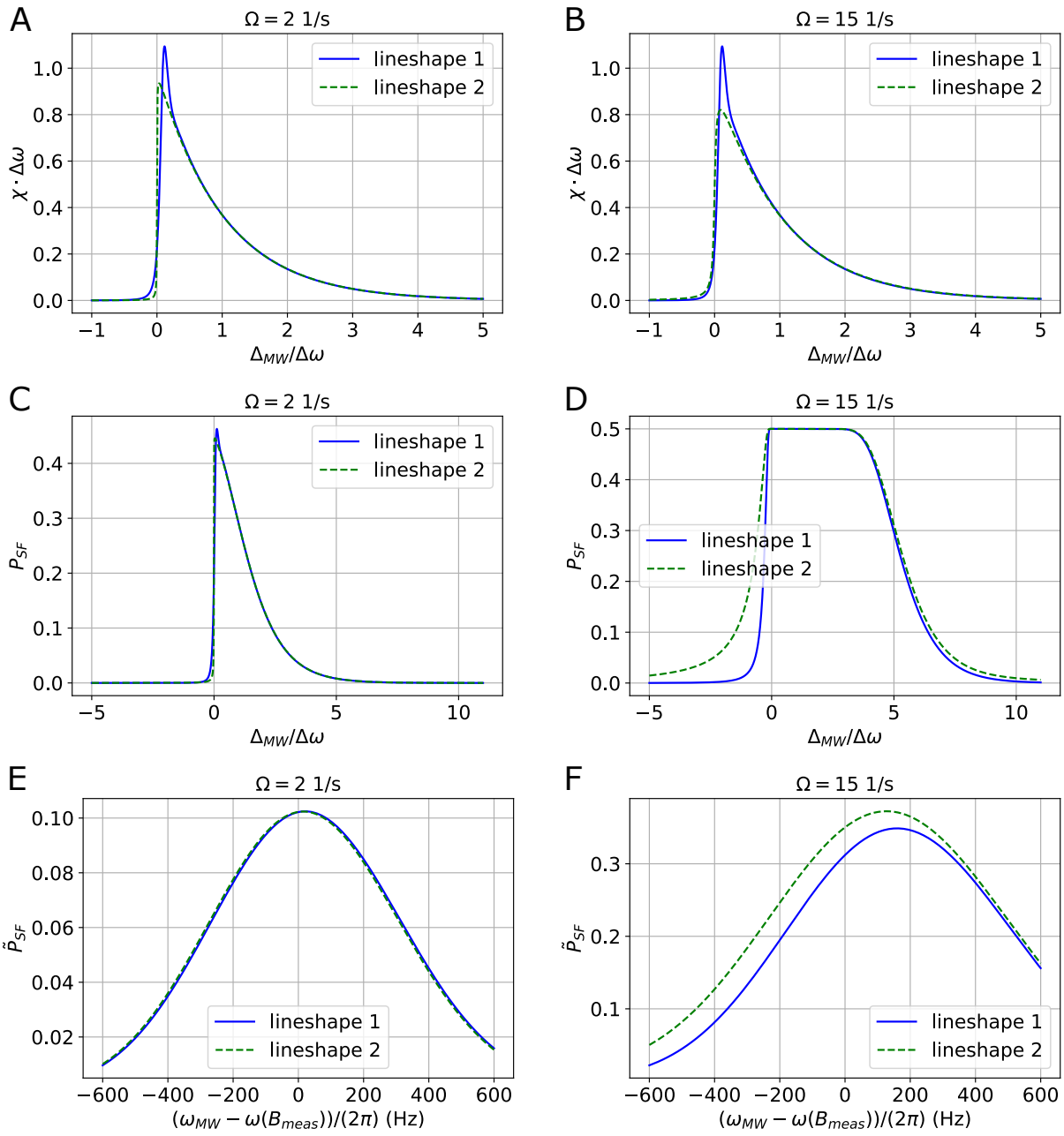

Figure 3.2. Lineshape and spin-flip probability for both lineshape models for an electronic transition in the PT with linewidth $\Delta\omega = 634\ \mathrm{s}^{-1}$. The x-axis in (A)-(D) is $\Delta_{MW}/\Delta\omega = (\omega_{MW} - \omega_{ij}(B_0))/\Delta\omega$, while in (E) and (F) it is given by $\omega_{MW} - \omega_{ij}(B_{\mathrm{meas}}) = \Delta_{MW} - \Delta\omega$, compare Eq. (3.22).
(A) and (B): lineshapes $\chi_1(\Delta_{MW}, \gamma, \Delta\omega)$ and $\chi_2(\Delta_{MW}, \Omega, \Delta\omega)$ given in Eqs. (3.12) and (3.20) for two Rabi frequencies. (C) and (D): spin-flip probability (Eq. (3.9)). (E) and (F): spin-flip probability convoluted with the Gaussian distribution describing the double dip measurement, see Eq. (3.23).

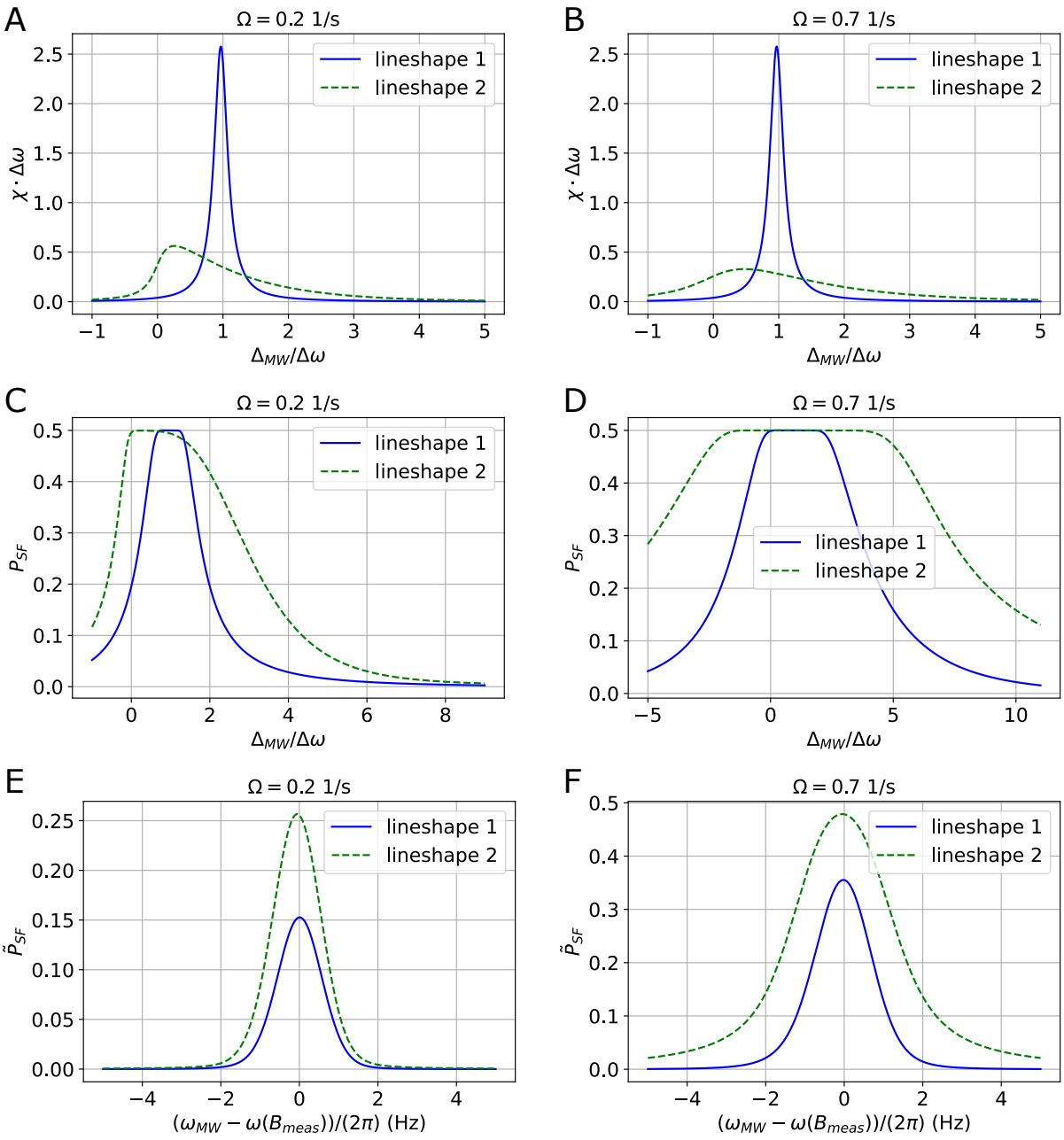

Figure 3.3. Lineshape and spin-flip probability for both lineshape models for a nuclear transition in the PT with linewidth $\Delta\omega = 1.2\ \mathrm{s}^{-1}$. The x-axis in (A)-(D) is $\Delta_{MW}/\Delta\omega = (\omega_{MW} - \omega_{ij}(B_0))/\Delta\omega$, while in (E) and (F) it is given by $\omega_{MW} - \omega_{ij}(B_{\mathrm{meas}}) = \Delta_{MW} - \Delta\omega$, compare Eq. (3.22).

(A) and (B): lineshapes $\chi_1(\Delta_{MW}, \gamma, \Delta\omega)$ and $\chi_2(\Delta_{MW}, \Omega, \Delta\omega)$ given in Eqs. (3.12) and (3.20) for two Rabi frequencies. (C) and (D): spin-flip probability (Eq. (3.9)). (E) and (F): spin-flip probability convoluted with the Gaussian distribution describing the double dip measurement, see Eq. (3.23).

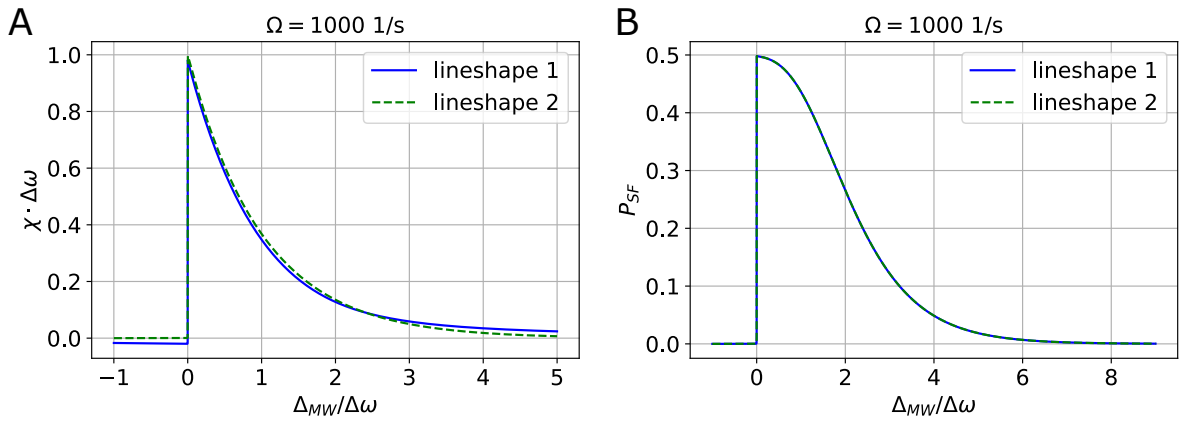

Figure 3.4. Lineshape and spin-flip probability for both lineshape models for an electronic transition in the AT with $\Delta\omega = 673 \cdot 10^5$ s^{-1}. (A): lineshapes $\chi_1(\Delta_{MW}, \gamma, \Delta\omega)$ and $\chi_2(\Delta_{MW}, \Omega, \Delta\omega)$ given in Eqs. (3.12) and (3.20). (B): spin-flip probability (Eq. (3.9)).

Chapter 4

Design of the Experiment

4.1 Overview

The Penning-trap system is located at the center of the vertical cold bore of a superconducting magnet with a magnetic field $B = 5.72$ T. The coils of the superconducting magnet are thermalized by a 160 l liquid helium reservoir connected to the cold bore filled with about 14 l liquid helium. The helium reservoir is surrounded by an insulation vacuum and an additional liquid nitrogen reservoir to reduce the heat load at the 4 K stage.

A sectional view of the setup inside the magnet is shown in Fig. 4.1. On top of the vacuum apparatus, a CF60 double-cross with separate flanges for the DC supply-, HV supply-, excitation- and detection-line feedthroughs as well as the turbopump and a window flange is placed. Above the window, the microwave setup that emits the microwaves for electronic spin-flip excitation through the window is screwed onto a bredboard. The electronic lines are lead into the prevacuum chamber through two CF16 stainless steel tubes, to which aluminium plates serving as heat shields are fixed. The spaces in between the shields are stuffed with cotton such that the vaporized helium is forced to rise slower out of the setup, cooling it while the helium heats up from 4 K to room temperature.

The prevacuum chamber, which contains the axial frequency detectors, the 70 K filter stage for the electronic lines and the trap chamber, is continuously pumped by the turbopump during the experiment. Before inserting the setup into the magnet, the flanges of the trap chamber are indium sealed and the trap chamber is baked out and pumped for several days to around 10^{-6} mbar through a copper tube soldered in the trap chamber which is finally pinched-off to seal the inner volume. When the setup is inserted into the magnet, the residual gas freezes due to the cryogenic temperature, leading to ion storage times of several months in the trap [47]. The magnetic field in the trap chamber is additionally stabilized by a shielding coil consisting of a superconducting NbTi wire

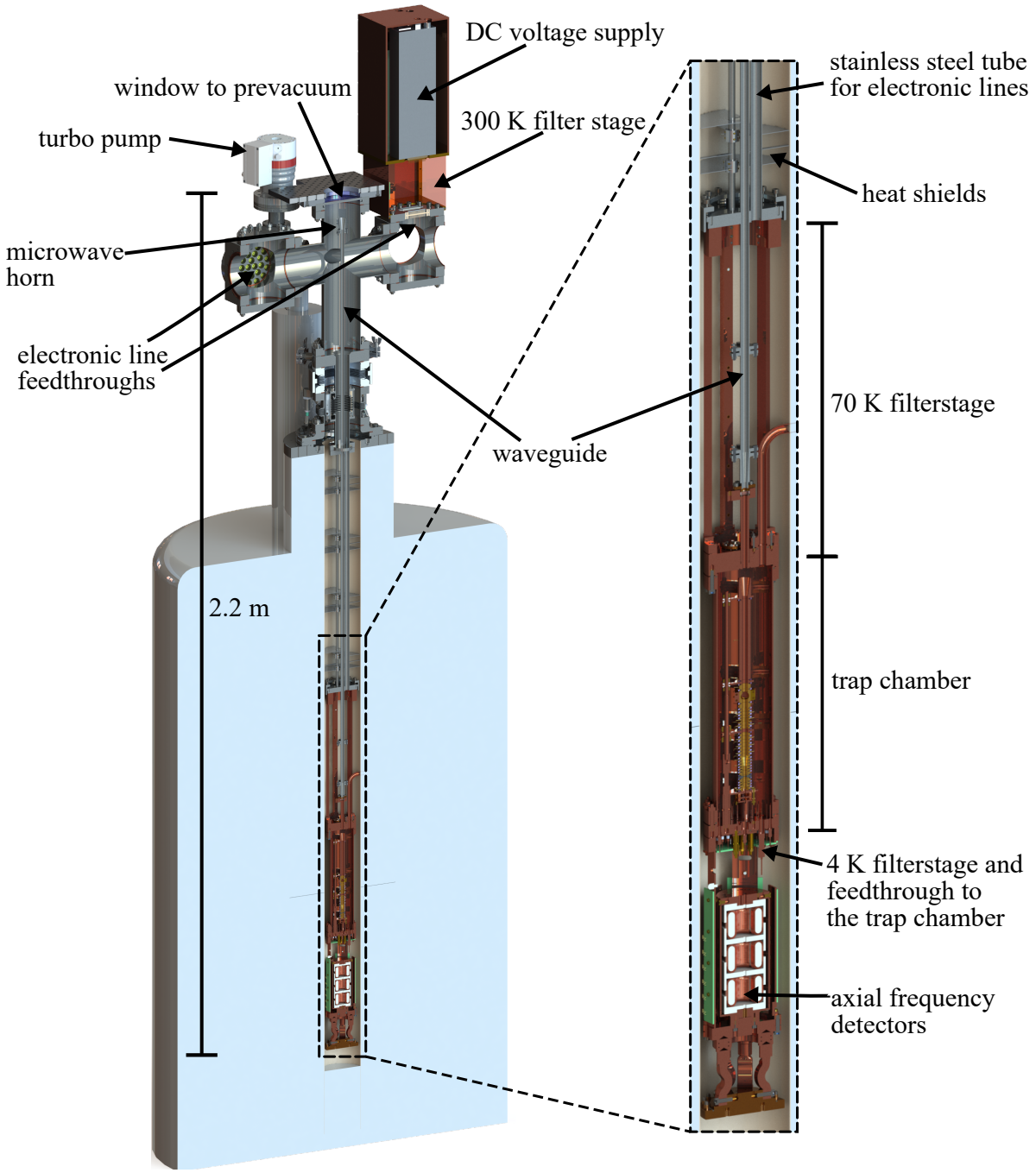

Figure 4.1. Computer-aided design (CAD) model of the experimental setup. On the right side the prevacuum chamber containing the trap chamber, detection system and the DC filters at 70 K and 4K is shown in more detail.

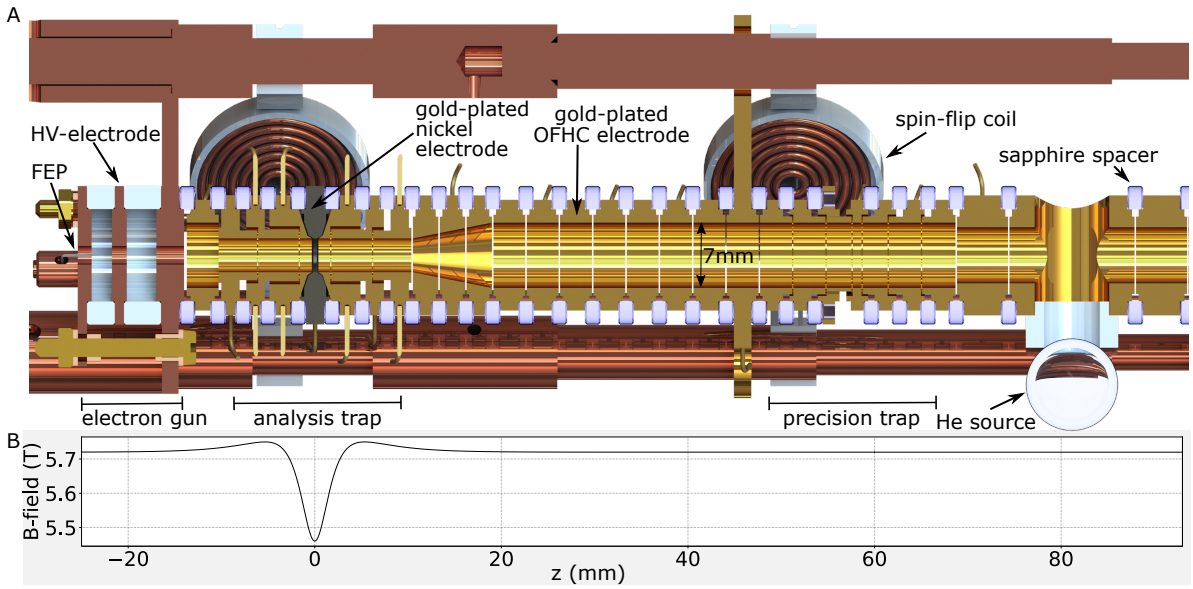

Figure 4.2. (A) Sectional view of the trap tower. The gold-plated nickel electrode is depicted in grey. The microwaves for driving nuclear transitions are radiated from the depicted copper spin-flip coils, while the 150 GHz microwaves for driving electronic transitions are transmitted through a waveguide from the top of the right side. The field-emission-point (FEP) on the left side is used to ionize the atoms emitted by the resistively heated ^{3}He filled glass sphere. (B) Spatial variation of the magnetic field inside the trap tower along the z-axis.

wound around the trap chamber [48].

4.2 Trap tower

A cross sectional view of the assembled trap tower is shown in Fig. 4.2 and a photograph in Fig. 4.3. It consists of the electrode gun, the analysis trap, transport electrodes, the precision trap, the target electrode where the ^{3}He source is attached and on top a 8 cm long electrode as part of the microwave guide, see Sec. 4.4. The stack of electrodes is pressed together and suspended by copper rods inside a 10 cm diameter trap chamber. The electrodes are made of oxygen-free high thermal conductivity (OFHC) copper with a tolerance of a few micrometers and then galvanically gold plated with a layer of 8 µm gold on top of 7 µm silver. The electrodes are kept at a distance of 0.14 mm from each other by sapphire rings.

The PT consists of five cylindrical electrodes with inner radius 3.5 mm and the electrode lengths were optimized to achieve $C_4 = C_6 = 0$ at the same optimal tuning ratio $TR_4 = TR_6$ as well as $D_2 = 0$ by solving these equations with the analytical expression for the potential coefficients C_i given in Sec. 2.2. Because of the limited precision with

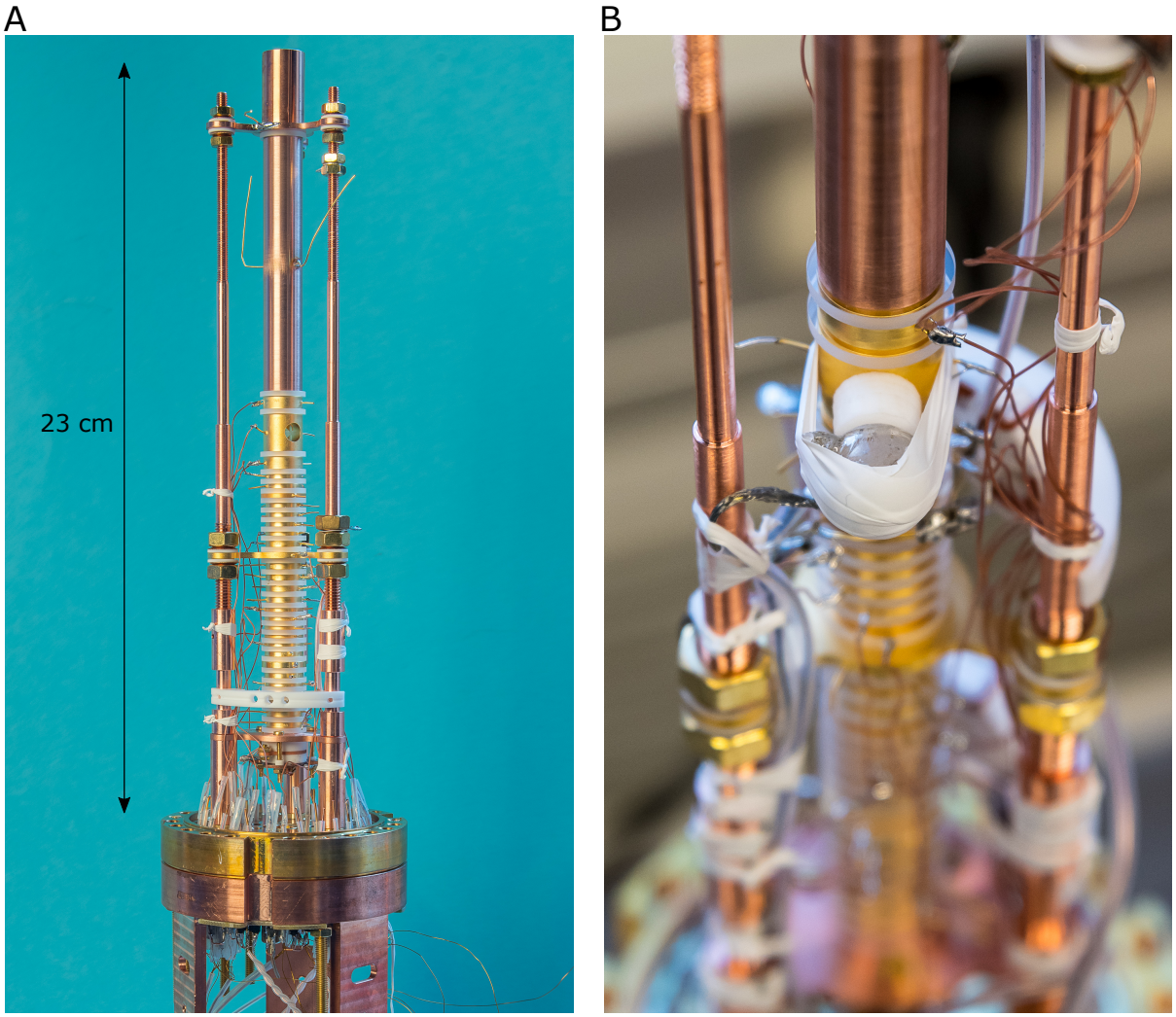

Figure 4.3. (A) Photograph of the assembled trap tower. (B) Glass sphere serving as ^{3}He source mounted on the trap tower with thermally insulating PTFE.

which the electrodes can be produced, the optimal trap length are then rounded to 1 µm, which leads to the non-zero D_2 and $\Delta TR = TR_4 - TR_6$ given in Tab. 4.1. One of the correction electrodes in the PT is split and the halves are isolated from each other with sapphire spacers to allow for the creation of quadrupolar fields that couple the ion's axial and radial modes via sideband coupling and also the direct detection of the modified cyclotron frequency via image current detection.

The shape of the ferromagnetic ring and the correction electrodes of the AT, see Fig. 4.2, was optimized in [49] for the creation of a large magnetic bottle as well as a compensated and orthogonal electrostatic potential by finite element method (FEM) calculations, as the analytical expression for the potential of cylindrical electrodes is not an adequate approximation in this case. For this experiment, the ring electrode of the AT is made of ferromagnetic Ni, rather than a material with higher magnetization such as Co/Fe, as it creates a sufficiently strong inhomogeneity B_2 at the chosen trap radius of 1.8 mm to easily detect electronic spin-flips via axial frequency jumps of $\Delta\nu_z = 22.5$ Hz.

The centers of the two traps are separated by 6 cm with transport electrodes to achieve a theoretical magnetic inhomogeneity $B_2 = 0.12\ \mathrm{T\,m^{-2}}$ in the PT, small enough for the shifts of the measured frequencies to be negligible.

Table 4.1. Theoretical parameters of the PT and AT as designed.

	PT	AT
inner radius a (mm)	3.5	1.8
ring length l_r (mm)	0.988	0.386
correction electrode length l_c (mm)	2.715	1.359
potential coefficient C_2 ($\mathrm{mm^{-2}}$)	−30586.6	−114310
orthogonality parameter D_2 ($\mathrm{mm^{-2}/Unit}_{TR}$)	5.6	22
optimal tuning ratio TR_4 for $C_4 = 0$	0.880964	0.8797
optimal tuning ratio TR_6 for $C_6 = 0$	0.880940	0.8801
magnetic field at the center B_0 (T)	5.72	5.46
magnetic bottle at the center B_2 ($\mathrm{T/m^2}$)	0.12	$87 \cdot 10^3$

4.3 Ion source

As described above, the trap chamber is hermetically sealed from the surrounding pre-vacuum and the ^{3}He can therefore not be introduced into the trap by an external gas inlet. Instead, a ^{3}He filled SO_2 glass sphere with an attached heating resistor inside

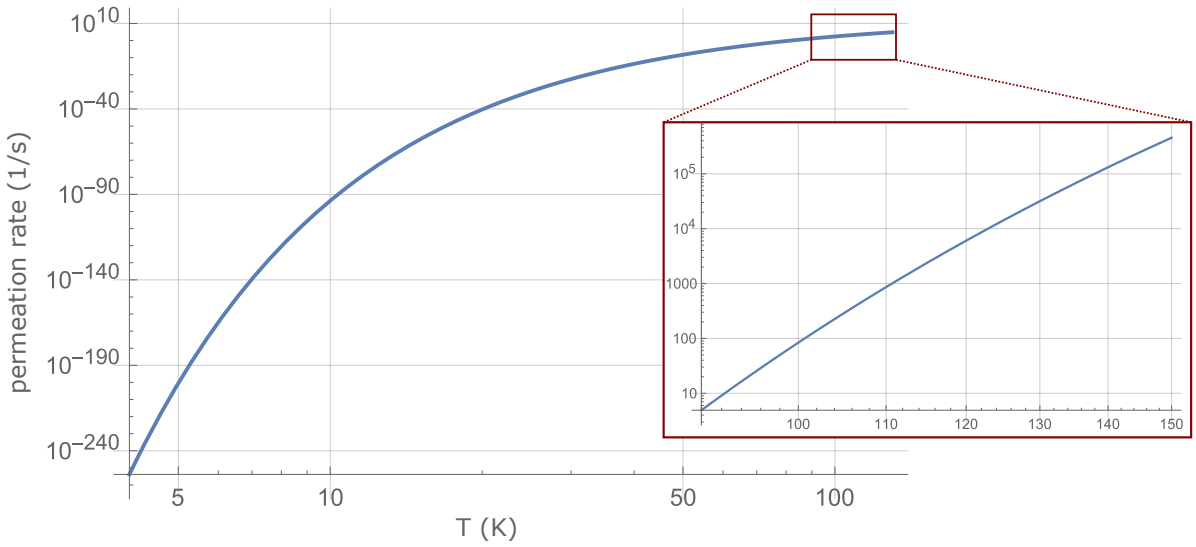

Figure 4.4. Number of helium atoms per second which diffuse out of the quartz sphere with diameter 1 cm and wall thickness 1 mm as function of the temperature [50, 51].

the trap chamber serves as an internal ^{3}He source (Fig. 4.2 and Fig. 4.3 B). Except for rubber, glass and in particular fused silica SO_2 is the material most easily permeated by helium [52] and has a strongly temperature dependent permeability (Fig. 4.4). Thus, at 4 K the rate of released atoms is negligible and does not compromise the vacuum while at approximately 100 K the permeation rate is sufficient to ionize of the order of 1 atom per second [50]. The target electrode, placed above the PT, has two opposing holes of diameter 7 mm where the glass sphere with diameter 1 cm is attached via a 5 mm long PTFE ring for thermal insulation. Three 200 Ω SMD thinfilm resistors are mounted around the sphere with thermally conductive glue (*Electrolube* TBS20S) and connected with copper wire in series. They are used to create a heating power of 1 W for around 10 s to reach the necessary temperature in the sphere. Afterwards, the released He atoms are ionized by electron impact using an electron gun (Fig. 4.2) consisting of a high-voltage electrode above a field-emission-point (FEP) made of tungsten wire with the etching method described in [53]. When a high voltage of around 1 kV is applied at the high-voltage electrode, an electron beam is emitted from the tip of the FEP and accelerated along the magnetic field lines through the trap tower. During loading, the electrodes above the PT where the glass sphere is placed and the upper endcap of the PT are biased with a voltage slope guiding positive ions into the PT. Simultaneously a negative voltage is applied to the FEP so that the emitted electrons reach at least 24.6 eV, the first ionization energy of helium, in the electrode potentials or $\sim$ 100 eV to maximize the cross-section [54, 55].

4.4 Microwave transmission

The microwaves for spin-flip excitation need to be transmitted inside the experiment over a distance larger than 1.5 m from the CF60 cross to the trap chamber at the center of the magnet, see Fig. 4.1. For the nuclear transitions at about 4.5 GHz this can be achieved by semi-rigid coaxial cables with low heat conductivity that lead directly to the feedthrough flange of the trap chamber. Inside the trap chamber cables lead to two copper coils next to the analysis and precision trap, which produce a radial magnetic field component at the center of the trap. However, microwaves at the higher frequencies of the electron spin transitions at 150 GHz can only be efficiently transmitted through waveguides not cables. The waveguides and horns used for this purpose were designed to optimise for low microwave power losses in [41].
The microwave signal is provided by an Anritsu MG3692C signal generator and fed into the signal generator extension (SGX) from VDI, which multiplies the input frequency by a factor of 12. In order to reduce the magnetic field that the microwave generator is exposed to, it is placed around 30 cm above the CF window flange held up by rods attached to the bredboard placed there. From the SGX module, the microwaves pass through a standard straight WR6 waveguide piece to a microwave horn that transmits the microwaves through the window to the prevacuum stage, where an oversized waveguide consisting of a 1.5 m long stainless steel pipe with a radius of 4 mm picks them up. With this oversized stainless steel waveguide the heat load can be reduced drastically compared to standard copper waveguides. It is flanged to a 5.7 cm long transition section that adapt the inner radius from 4 mm to the 2.5 mm radius of the following window flange that leads into the trap chamber. The fused silica window flange that is cryogenically sealed with indium separates the vacuum inside the trap chamber from the prevacuum. In the trap chamber, the microwaves are coupled in through a copper horn with a small opening angle connected to a 8 cm long electrode which bridges the gap to the trap stack.

4.5 Detection system

The detection system consists of a cryogenic low-noise amplifier and a high-Q tank circuit in form of a coil wound around a PTFE core and surrounded by a cylindrical OFHC housing. For this experiment three axial detectors and one cyclotron detector were designed [56]. Fig. 4.5 shows CAD models of the axial and cyclotron detectors and Tab. 4.2 shows the results of their characterization in a cryocooler test and in the final setup. In the cryocooler a test version of trap electrodes was used as capacitive load and the self-inductance as well as self-capacitance were deduced from the measured resonance

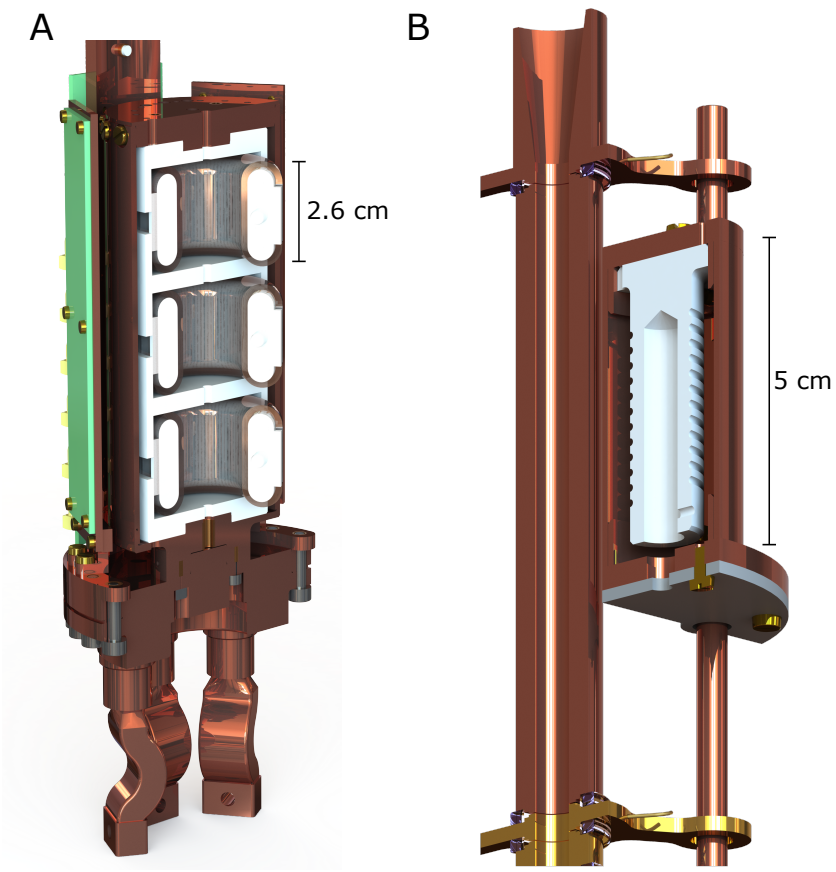

Figure 4.5. (A) CAD model of the assembled axial detection system. The amplifier boards are arranged around the copper housing holding the three coils. (B) Sectional view of the cyclotron resonator housing with amplifier board at the bottom and coil body inside. The resonator is attached next to the trap tower.

frequencies with different additional parallel capacitances [56].

The axial resonators consist of a toroidal PTFE core around which approximately 1000 windings of formvar-insulated NbTi wire with a diameter of 0.075 mm are wrapped in three layers. Formvar and PTFE are chosen due to their low loss tangents to improve the signal-to-noise ratio of the detectors. The toroidal geometry additionally reduces eddy current losses induced by the magnetic field in the surrounding material as it confines most of the coil's magnetic field inside the PTFE core. Each coil is on one end connected to ground and after N of the total N_{tot} windings a tap leads to a cryogenic amplifier. The other end of the coil is connected to the trap electrode. In this way an autotransformer is created so as to suppresses limitations of the coil's effective parallel resistance due to the input resistance of the amplifier [31, 57]. The coupling factor $\kappa = N/N_{tot}$ modifies the signal-to-noise ratio and linewidth of the dip and is chosen to be $\kappa = 0.2$ for this setup.

The axial resonators are placed in an OFHC copper housing below the trap chamber so that both the resonators and their amplifiers are thermalized near 4 K. Copper braided

Table 4.2. Self-inductance L, self-capacitance C and Q-values determined in the cryocooler test setup and resonance frequency and Q-value in the final setup inserted in the magnet.

resonator	ν_{res}	L	C	Q (cryocooler)	Q (magnet)
axial PT	515.3 kHz	3.56(1) mH	12.0(1) pF	7000(500)	5100(200)
axial AT	472.2 kHz	3.33(1) mH	12.9(1) pF	7000(500)	4200(200)
axial spare	780.8 kHz	1.49(1) mH	6.60(1) pF	13500(500)	12400(500)
cyclotron PT	28.96 MHz	1.08(1) μH	2.35(1) pF	610(20)	600(150)

hoses additionally connect the bottom of the copper housing to the lower flange of the prevacuum chamber to improve the thermal coupling to the liquid helium bath. The copper housing can hold three toroidal coils, one for each trap and a spare resonator which is additionally attached to the AT. The number of windings $N \propto \sqrt{L}$ is adjusted to reach the resonance frequency of $^3He^+$ in the 14 V range of the voltage source for the C_2 of the particular trap, taking into account the coil's self-capacitance of approximately 10 pF and another 15 pF from the trap and the feedthroughs.

In the PT, a cyclotron resonator is additionally installed which is used for the ion preparation and detuned from the ion frequency by means of a tunable parallel capacitance during the HFS measurements. For the cyclotron detector the optimization of the Q-value is not as critical as in case of the axial detectors which have to allow for effective dip detection. The coil of the cyclotron detector was therefore made from 99.99% pure copper with a diameter of 0.4 mm instead of a superconducting material to avoid thermalization problems. As the effective parallel resistance of the cyclotron resonator is only 120 kΩ, no decoupling of the amplifier via an inductive tab as for the axial detectors is necessary. In order to reduce the parasitic capacitances between the hot end of the resonator and ground, the wires between the resonator and the trap and the amplifier are kept short. Therefore, the amplifier is attached directly on top of the resonator's OFHC housing which is placed inside the trap chamber close to the PT. Because of the limited space in the trap chamber, a solenoid coil instead of a toroidal coil is chosen here. The number of windings $N = 38$ was adapted to achieve a resonance frequency slightly larger than the ion's eigenfrequency, as the resonance frequency can be easily decreased but not increased after the characterisation by an additional parallel capacitor.

The cryogenic amplifier design generally used for this application, described in [31], consists of a first amplifier stage with one dual-gate MESFET in common-source layout (cascode) and a source follower as second stage. The latter matches the high output

impedance of the first stage to the impedance of the rf-lines, while the cascode serves to provide a high voltage gain at high input impedance. This layout requires four supply lines, the two gates of the first MESFET (G_1 and G_2), the gate of the source follower (G_{sf}), and a shared terminal for the drain of both transistors (D). The cyclotron amplifier design is similar to that of the axial amplifier but has an additional fixed capacitor and a tunable capacitor in form of a varactor diode to adjust the resonance frequency. The amplifier boards were manufactured from PTFE laminate milled circuit boards using low loss SMD components with the cryogenic GaAs MESFETs *NEC* NE25139 and *Siemens* CF739 as cascode and source follower, respectively. They were afterwards tested and characterized in a cryocooler setup [56].

4.6 Wiring

From outside the vacuum setup, the electronic lines are guided through feedthrough flanges to the prevacuum stage and via another feedthrough flange at the bottom of the trap chamber to the trap. Here, alumina vacuum feedthrough are used except for the lines connecting the axial resonators placed outside the trap chamber to the trap electrodes, where sapphire feedthroughs are utilized to reduce losses.

The complete connection diagram is shown in Fig. 4.6. On the left side, the instruments connected to the setup at room temperature are shown. The electrode biases are supplied by two *Stahl-Electronics* UM1-14 high-precision voltage sources, where the channels 'A', 'B' and 'C' are the high-precision channels used for the ring and correction electrodes. The DC lines are filtered at room temperature, 70 K and again at 4 K with surface-mounted device (SMD) RC low-pass filters. These consist of a $R = 820$ kΩ resistor and a $C = 4.7$ nF capacitance or for the central trap electrodes a $C = 20$ nF capacitance. The cryogenic amplifier requires 5 DC supplies, one of which connected to the drain (D) of the transistors and is therefore filtered with a smaller resistor, $C = 1$ µF and $R = 50$ Ω, to reduce the heating power due to the ~ 3 mA drain current. The layout of the 70 K and 4 K filter boards are depicted in Fig. 4.7. The 4 K board is attached directly on top of the feedthrough flange of the trap chamber. At the 70 K stage, the lines coming from room temperature or 4 K are attached with plug connections, so that the trap chamber can be removed from the rest of the setup in assembly.

The AC lines, high-voltage lines and the line for the heater of the ^{3}He source are guided by cryogenic coaxial cables. Inside the trap chamber all lines are connected to the electrodes by copper wire. The coaxial cables for the quadrupole and dipole excitation lines are attached with a twisted pair to the 4 K filter board, where external noise is reduced using a capacitive voltage divider and the DC line connected to the same electrode

is blocked by a $R = 500$ kΩ resistor. The PT quadrupole excitation line is connected to one of the two halves of the split correction electrode of the PT. The two halves are connected by a $R = 27$ MΩ resistor and the second half leads to the cyclotron detector, which is placed inside the trap chamber to minimize the wire length. In the AT, the spin-flip coil can be used for quadrupole excitation. Both traps have a dipole excitation line connected to one of their endcaps. The signals for quadrupole and dipole excitation are created by a *Keysight* 33600A Waveform Generator and the nuclear spin-flip drive by a *Systron Donner* Microwave Synthesizer.

The three axial resonator coils and the cyclotron resonator coil are shown as grey boxes in Fig. 4.6. The feedback line is mounted in close proximity to the axial detection line of the PT to achieve capacitive signal coupling. The axial and cyclotron detection signals coming from the cryogenic amplifiers are additionally amplified at room temperature by *Mini-Circuits* ZFL-500LN amplifiers and down-mixed by a single-sideband down converter [56, 58] into the 10 kHz range so that it can be digitized by a *National Instruments* NI-9250 module and then analyzed via Fast Fourier Transformation (FFT). All frequency generators and signal analyzers are locked with a *Stanford Research Systems* FS725 Rubidium 10 MHz frequency standard, which is itself locked to a GPS pps signal to allow for absolute frequency determinations as necessary to measure the zero-field splitting E_{HFS}.

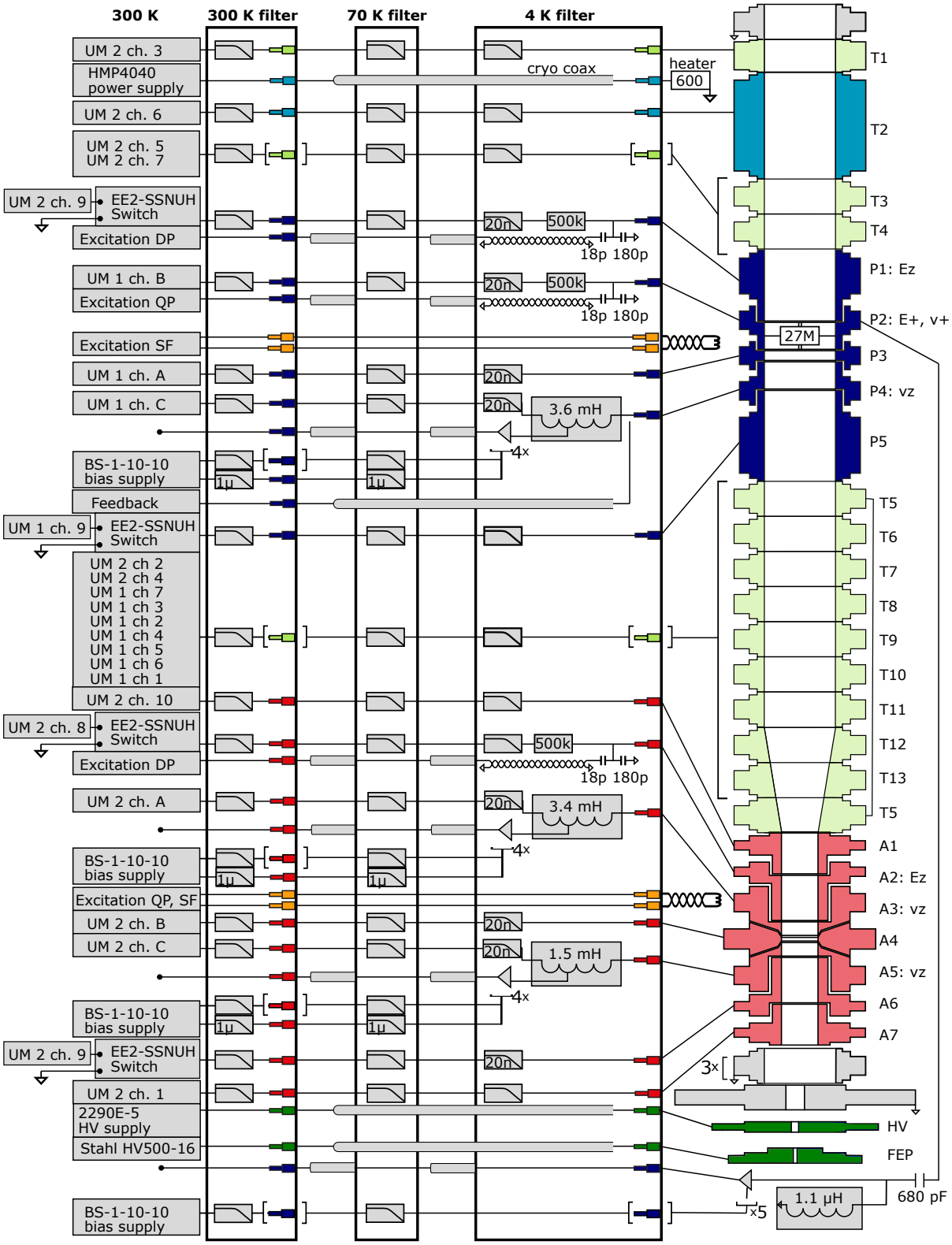

Figure 4.6. Connection diagram of the setup. Where not indicated differently, the RC low-pass filters consist of a $R = 820$ kΩ resistor and a $C = 4.7$ nF capacitance. Otherwise they consist of $C = 20$ nF and $R = 820$ kΩ or $C = 1$ µF and $R = 50$ Ω.

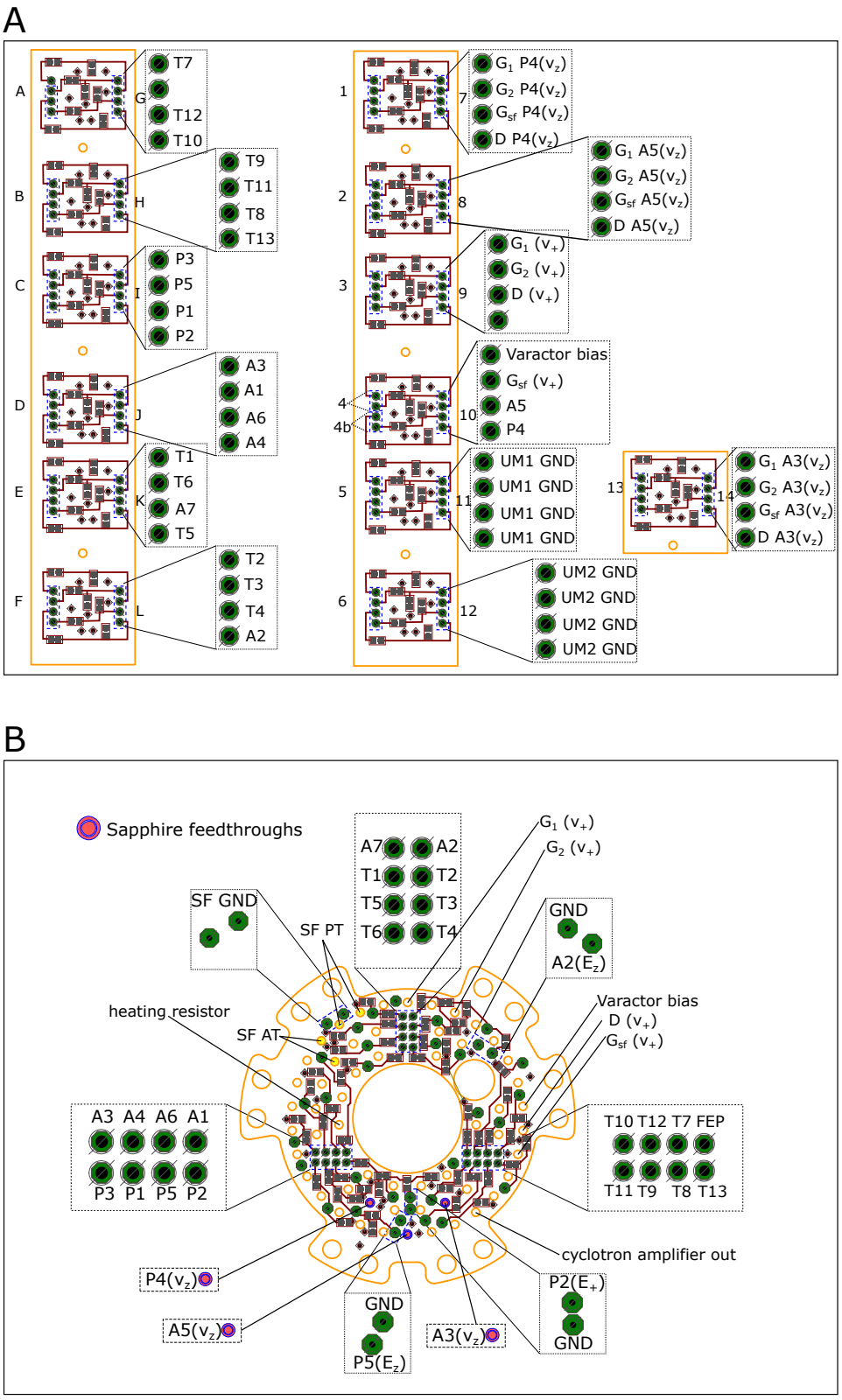

Figure 4.7. Schematics of the filter boards, where G_1, G_2, G_{sf} and D refer to the cryogenic amplifier supply lines and UM GND connects ground of the high-precision voltage supply to ground on the 4 K board. (A) 70 K filter boards. The cables coming from the trap chamber or from room temperature are connected with plugs to simplify the assembly. (B) 4 K filter board, designed to fit directly on top of the flange containing the feedthroughs to the trap chamber. The sapphire feedthroughs connect the axial resonators outside the trap chamber to the electrodes.

Chapter 5

Trap Characterization

5.1 Precision trap

5.1.1 Ion preparation

After first inserting the experiment into the superconducting magnet, the magnetic field in the PT is determined from double-dip spectra using $^{12}C^{4+}$ ions, to then be able to unambiguously identify $^{3}He^{+}$ via its cyclotron frequency. The carbon frozen on the walls of the trap chamber allows loading $^{12}C^{4+}$ ions into the trap independently of whether the ^{3}He source is heated simultaneously, using the electron gun with a FEP bias of around -90 V. The cyclotron frequencies of $^{12}C^{4+}$ and $^{3}He^{+}$ are different by $\nu_c^{^3He^+} - \nu_c^{^{12}C^{4+}} = -156$ kHz, so that $^{12}C^{4+}$ can also be observed via peaks on the cyclotron detector calibrated for $^{3}He^{+}$. When loading ^{3}He ions, as described in Sec. 4.3, a lower FEP bias of -60 V is applied to avoid contamination with $^{12}C^{4+}$, thereby simplifying the cooling and cleaning process as both species have a similar axial frequency $\nu_z^{^3He^+} - \nu_z^{^{12}C^{4+}} = -1.4$ kHz. An axial dip spectrum with several 10 $^{3}He^{+}$ ions then becomes visible after cooling the magnetron mode by sideband coupling. Unwanted ion species in the trap, such as protons and low charge states of ^{12}C and ^{16}O, are afterward removed from the trap by exciting their axial modes, while leaving $^{3}He^{+}$ unaffected, and subsequently lowering the axial potential to a minimal value around -0.1 V for 1 s. For this purpose, a broadband signal with notches around the $^{3}He^{+}$ eigenfrequencies is applied using an arbitrary waveform generator (Stored waveform inverse Fourier transform, SWIFT), while the axial frequency of the $^{3}He^{+}$ ions is in resonance with the axial detector for cooling. A single $^{3}He^{+}$ ion is finally prepared by heating the modified cyclotron mode with rf-sweeps until only a single peak is observed on the cyclotron resonator. Due to the relativistic mass increase the modified cyclotron frequency of the hot ions is reduced significantly, so that they can be selectively excited further before lowering the trapping potential to remove the most

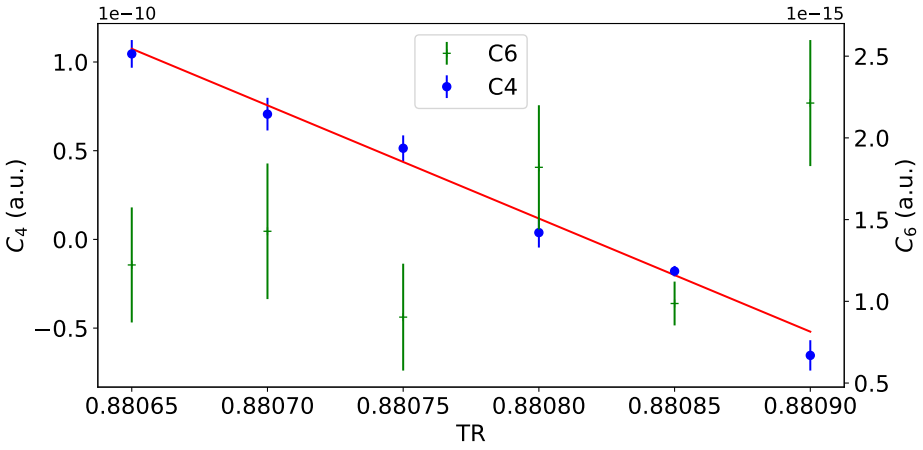

Figure 5.1. C_4 and C_6 fitted to the axial frequency shift after magnetron excitation to different energies.

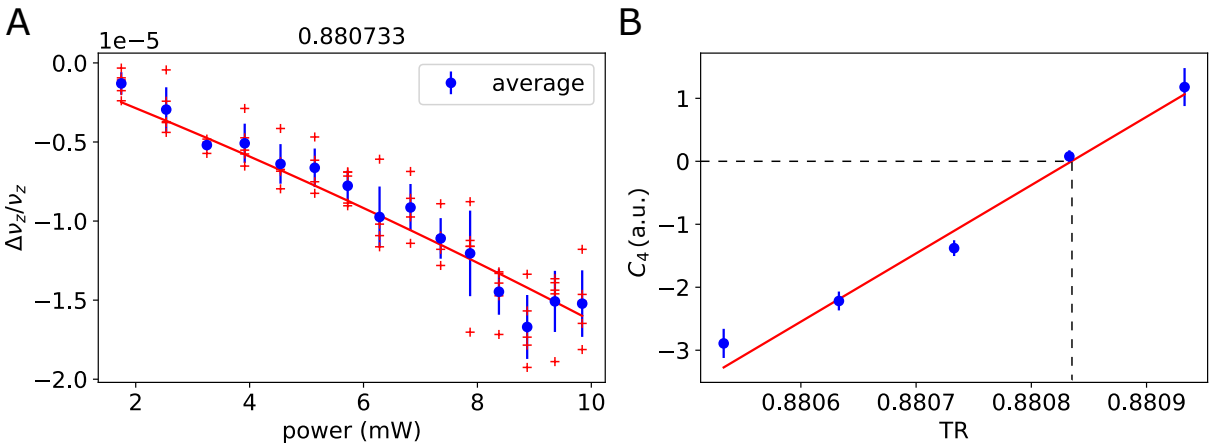

Figure 5.2. Tuning-ratio optimization with axial noise. (A) Relative axial frequency shift as function of excitation power for one of the tuning ratios. (B) Fitted slope as function of the tuning ratio.

excited ions. Whether the observed signal is due to only a single $^3He^+$ ion can be afterward verified by measuring the 3 db width of the axial dip signal, which is proportional to the number of ions

$$\frac{\Delta\nu_{\mathrm{z,dip}}}{N_{\mathrm{ions}}} = 1.3(1)\ \mathrm{Hz}. \tag{5.1}$$

5.1.2 Tuning ratio

The frequency dependent shifts caused by anharmonicities of the electrostatic potential are minimized by optimizing the tuning ratio TR $= V_c/V_0$ to reach $C_4 = 0$, and the residual value of C_6 at this tuning ratio is characterized. For this purpose, the magnetron mode is excited with bursts of N cycles to different energies $\Delta E_- \propto N^2$ for different

tuning ratios and the resulting shift

$$\frac{\delta\nu_z}{\nu_z} \approx (a_1 C_4 + a_2 B_2)\,\Delta E_- + a_3 C_6 (\Delta E_-)^2 \tag{5.2}$$

of the axial frequency is measured, with a_1, a_2 and a_3 according to Sec. 2.3. The B_2-dependent term is negligible assuming the measured value of $B_{2,PT}$, see below. From the shifts $\delta\nu_z(N)$ at different tuning ratios follows the result plotted in Fig. 5.1 and thus the optimized tuning ratio $TR_{\mathrm{opt}} = 0.880833(3)$. In order to determine the residual anharmonic contributions and associated systematic corrections, the proportionality constant $\Delta E_-/N^2$ is determined by inserting the theoretical value

$$D_{4,theo} = -3.5 \cdot 10^9 \mathrm{m}^{-4}\mathrm{Unit}_{TR}^{-1} \tag{5.3}$$

for the measured slope $D_4 = dC_4/dTR$. It follows $C_4 = 0(5) \cdot 10^4$ m^{-4} and $C_6 = 2(1) \cdot 10^{-6}$ mm^{-6} at the optimized tuning ratio. From the same measurement follows the axial frequency shift per unit tuning ratio in the PT $D_2 = -2.0(2) \cdot 10^3$ Hz/Unit$_{TR}$.

As a cross-check, the tuning ratio was additionally optimized by heating the axial mode with white noise applied to the dipolar excitation line and measuring the axial frequency, see Fig. 5.2. The resulting shift of the axial frequency [30]

$$\frac{\delta\nu_z}{\nu_z} = \frac{3}{4}\frac{1}{qV_0}\frac{C_4}{C_2^2}E_z \tag{5.4}$$

is independent of $B_{2,PT}$ and the optimal tuning ratio found by this method $TR = 0.880834(13)$ agrees well with the value above.

5.1.3 Axial and cyclotron temperature

During the double-dip measurements of the cyclotron frequency in the PT, the coupling of the axial and modified cyclotron mode thermalizes the modified cyclotron mode with the axial detection system at

$$T_+ = T_z \frac{\nu_+}{\nu_z}. \tag{5.5}$$

These temperatures are determined by transporting the ion to the AT and measuring the axial frequency scatter. Due to the magnetic bottle in the AT, the axial frequency is shifted proportional to the Boltzmann-distributed cyclotron energy E_+. A similar measurement without cyclotron thermalization in the PT showed that the additional energy spread due to heating during transport from the PT to the AT is negligible. A maximum likelihood fit of a Boltzmann-distribution to the axial frequencies therefore gives the temperature $T_+ = \langle E_+ \rangle$ and thereby $T_z = 11.7(7)$ K, see 5.3 A and B.

At this temperature, the average spread of axial frequencies in the AT is 2.3 kHz. During the double-trap measurement of the HFS transition frequencies, the cyclotron

mode is therefore cooled in the PT ahead of each transport into the AT to reduce the voltage range that has to be scanned in order to detect the dip signal. Because of the large cooling time constant of the cyclotron resonator $\tau_{cyc} = 396(13)$ s, this is implemented instead by coupling the axial and cyclotron mode while reducing the axial temperature with negative feedback to $T_z = 2.5(5)$ K, see Fig. 5.3 C and D.

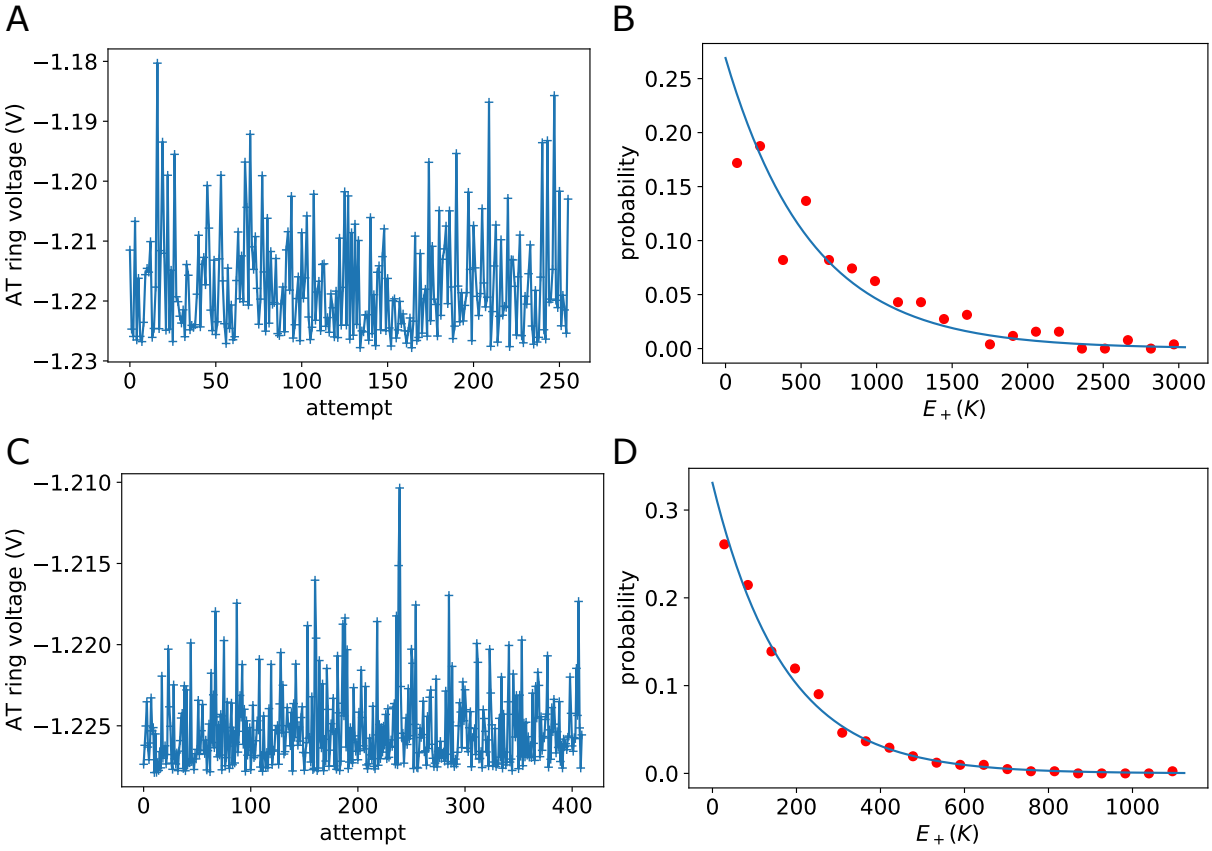

Figure 5.3. (A) Ring voltages that center the ion on the AT resonator after thermalizing the cyclotron mode in the PT. (B) Boltzmann-distribution of cyclotron temperatures in the PT following from the ring voltages in the AT. (C) and (D): Cyclotron energy distribution after feedback cooling in the PT.

Furthermore, the cyclotron temperature is determined from the C_4 and $B_{2,\mathrm{PT}}$ induced shifts of the axial frequency in the PT. After thermalizing the cyclotron mode at T_+ with sideband coupling, these shifts are amplified by directly exciting the modified cyclotron mode and subsequently the axial frequency in the PT is measured. This process is repeated 200 times with excitation pulses of fixed cycle number N and amplitude. The expectation value of the axial frequency fluctuations $\Delta\nu_{z,i} = \nu_{z,i} - \nu_{z,i+1}$ then is

$$\begin{aligned}\langle\Delta\nu_z\rangle &= \sqrt{2}(a_1C_4 + a_2B_2)\langle E_+\rangle \\ &= P_1(C_4, B_2)\langle\rho_+^2\rangle,\end{aligned} \tag{5.6}$$

using $E_+ = \rho_+^2 m_{^3He^+}\omega_+^2/2$ with constants $a_{1/2}$ as given in Eqs. (2.26) and (2.20). The cyclotron radius ρ_+ after applying the excitation pulse depends on the initial thermal cyclotron radius and the phase difference $\Delta\phi$ between excitation pulse and ion motion

$$\rho_+^2 = \rho_{\text{exc}}^2 + \rho_{\text{thermal}}^2(T_+) + 2\rho_{\text{exc}}\rho_{\text{thermal}}(T_+)\cos(\Delta\phi). \tag{5.7}$$

This leads to the expectation value and standard deviation as function of the excitation radius $\rho_{\text{exc}} \propto N^2$ [59]:

$$\begin{aligned}\langle\Delta\nu_z\rangle &\approx P_1(C_4, B_2)\rho_{\text{exc}}^2 \\ \delta\Delta\nu_z &\approx \sqrt{(P_2(C_4, B_2, T_+)\rho_{\text{exc}})^2 + P_0},\end{aligned} \tag{5.8}$$

with

$$P_2(C_4, B_2, T_+) = 2P_1(C_4, B_2)\sqrt{\frac{\pi k_B T_+}{2m_{^3He^+}\omega_+^2}}\sqrt{\frac{4}{\pi} + \frac{1}{2}}. \tag{5.9}$$

Here, P_0 is the energy independent contribution to the fluctuations of the axial frequency, mainly due to the electrode voltage supply and the axial dip fits. For this setup, the proportionality constant $\kappa = \rho_{\text{exc}}/N^2$, relating the excitation radius and the number of cycles N of the applied drive, is not calibrated independently so that the values for C_4 and $B_{2,\text{PT}}$ have to be inserted to then deduce κ and T_+ from the experimental results for $P_1\kappa^2$ and $P_2\kappa$. The magnetic bottle $B_{2,\text{PT}}$ was measured as described in the next section, while the value of C_4 at a given tuning ratio is deduced from the theoretical result for $D_4 = dC_4/dTR$ given in Eq. (5.3). The results for the standard deviation and average of the axial frequency fluctuations as function of the number of excitation pulse cycles N is plotted Fig. 5.4. This was repeated with two different values for C_4 by changing the tuning ratio by $1 \cdot 10^{-4}$, giving the results $T_z = 12.4(1.4)$ K at $C_4 = 0(52500)$ 1/m^4 and $T_z = 14.4(1.1)$ K at $C_4 = 350000(52500)$ 1/m^4. These agree with the result $T_z = 11.7(7)$ from the Boltzmann-distribution in the AT within 1 σ and 2 σ, respectively.

5.1.4 Magnetic field

The cyclotron frequency is determined from double dip spectra at different ions positions along the z-axis, see Fig. 5.5 A, by shifting the ion using asymmetric offsets on one correction electrode. Here, the ion position at a given offset voltage was calculated using the analytical expression of the potential of a cylindrical trap. From this measurement, the linear inhomogeneity $B_{1,PT} = 14.1(6)$ mT/m could be determined while the effect of the quadratic inhomogeneity $B_{2,PT}$ is too small in this range. The magnetic bottle $B_{2,PT}$ was instead measured by exciting the modified cyclotron mode and measuring the resulting shift of the axial frequency

$$\frac{\delta\nu_z}{\nu_z} = \frac{1}{m_{^3He^+}(2\pi\nu_z)^2}\frac{B_2}{B_0}E_+, \tag{5.10}$$

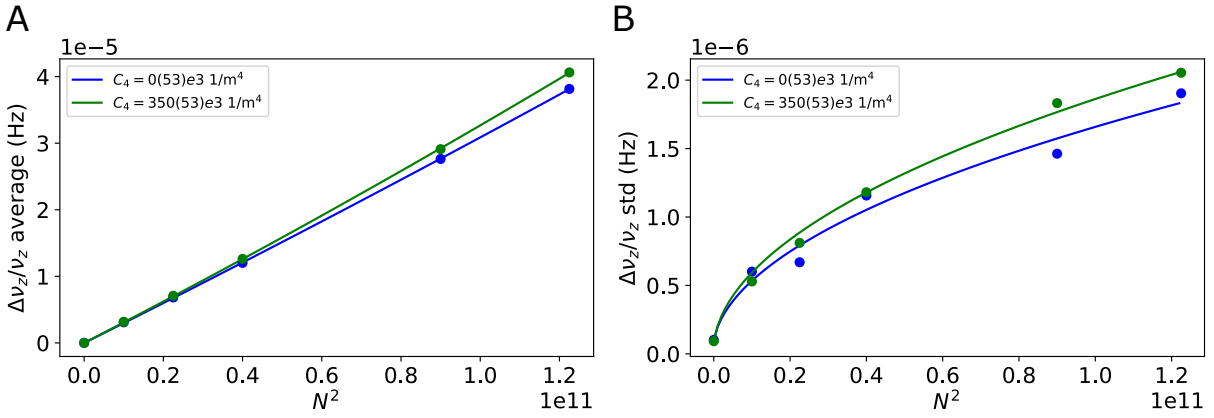

Figure 5.4. (A) Average and (B) standard deviation of 200 measurements of the axial frequency fluctuations after cyclotron excitation in the PT as function of the square of the number N of the excitation cycles at two different tuning ratios TR_{opt} and $TR_{\mathrm{opt}} - 1{\cdot}10^{-4}$.

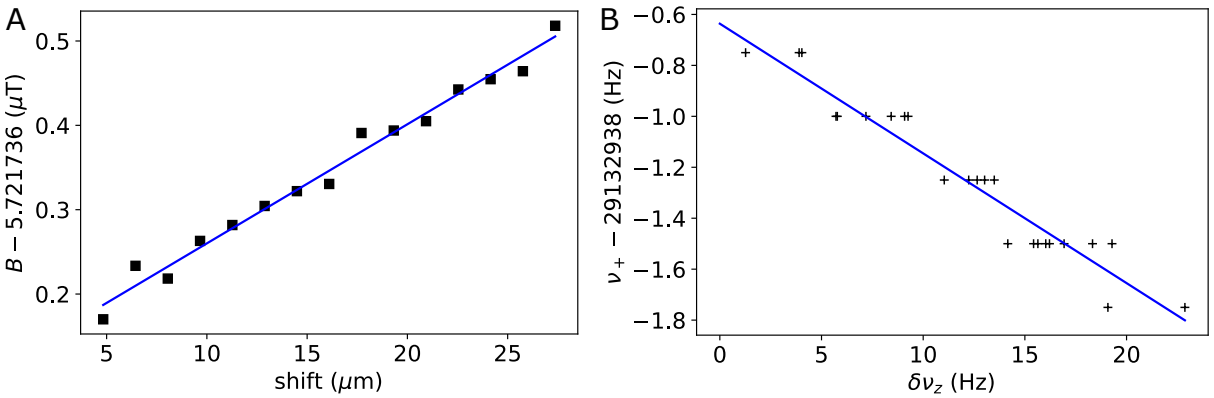

Figure 5.5. (A) Magnetic field in the PT for different offset voltages that lead to the plotted shifts of the ion positions along the z-axis. (B) Modified cyclotron frequency versus shift of the axial frequency after excitation of the modified cyclotron mode.

as well as the simultaneous shift of the modified cyclotron frequency

$$\frac{\delta\nu_+}{\nu_+} = \left(-\frac{1}{m_{^3He^+}c^2} - \left(\frac{\nu_z}{\nu_+}\right)^2 \frac{1}{m_{^3He^+}(2\pi\nu_z)^2}\frac{B_2}{B_0} \right) E_+. \tag{5.11}$$

The latter was determined by detecting the peak on the cyclotron resonator with an averaging time of 4 s $\ll \tau_{cyc} = 396(13)$ s, before detuning the cyclotron resonator via the varactor voltage to average the axial FFT signal without cooling the cyclotron mode. The second expression, Eq. (5.11), includes an additional $B_{2,PT}$ independent term accounting for the relativistic mass increase, which allows to extract $B_{2,PT}$ from the slope $\delta\nu_+/\delta\nu_z$ fitted in Fig. 5.5 B. Here, the uncertainty of the shifts of both frequencies due to the uncertainty of C_4 is negligibly small. The result $B_{2,PT} = 1.17(4)$ T m^{-2} is significantly larger than the value expected from the nickel AT ring electrode at the position of the PT $B_2 = 0.12$ T m^{-2}, due to either the trap placement in the superconducting magnet or other ferromagnetic components in the setup. This magnetic bottle leads to a spread of the modified cyclotron frequency

$$\Delta\nu_{+,B2} = \frac{\nu_+}{m_{^3He^+}(2\pi\nu_z)^2}\frac{B_{2,\mathrm{PT}}}{B_0}k_B T_z = 18(1) \text{ mHz}. \tag{5.12}$$

The stability of the measured cyclotron frequency can be seen in Fig. 5.6. The cyclotron frequencies plotted here result from taking alternating single-dip and double-dip spectra in the PT over a span of 12 h, where the axial frequency is determined by averaging the values measured before and after the sideband coupling. In this time frame no magnetic field drift is observed and the cyclotron frequency could be determined with a relative statistical uncertainty of $\Delta\nu_c/\nu_c = 1.8 \cdot 10^{-9}$, or $\Delta\nu_c = 41$ mHz, which is limited by the axial frequency determination. Here, the standard deviation of the fluctuations of the two axial frequencies $\nu_{z,1} - \nu_{z,2}$ measured before and after the sideband coupling is $\Delta(\nu_{z,1} - \nu_{z,2}) = 65$ mHz, see Fig. 5.6 B. The statistical uncertainty of a single axial frequency determination is therefore $\Delta\nu_{z,1/2} = \Delta(\nu_{z,1} - \nu_{z,2})/\sqrt{2} = 46$ mHz, where the dominant contribution is due to the voltage fluctuations of the high-precision voltage supply UM-1-14. According to the specifications these are limited to ≤ 1.1 µV $\equiv 50$ mHz in the ± 0.10 K temperature stabilized laboratory. As the two axial frequencies before and after the double-dip spectrum are measured at different cyclotron energies, the frequency shift due to the residual magnetic bottle in the PT quadratically contributes to the fluctuations

$$\Delta\nu_{z,B2} = \frac{1}{m_{^3He^+}(2\pi)^2\nu_z}\frac{B_{2,\mathrm{PT}}}{B_0}k_B T_+ = 18(1) \text{ mHz}. \tag{5.13}$$

In the cyclotron measurement with the double-dip method the axial frequency shifts due to $B_{2,\mathrm{PT}}$ cancel, see also next chapter.

Long term magnetic field drifts observed in the PT during the double-trap measurements over several days are $\Delta\nu_c/\nu_c < 1.5 \cdot 10^{-9}$ per hour, see for example Fig. 5.7. This is

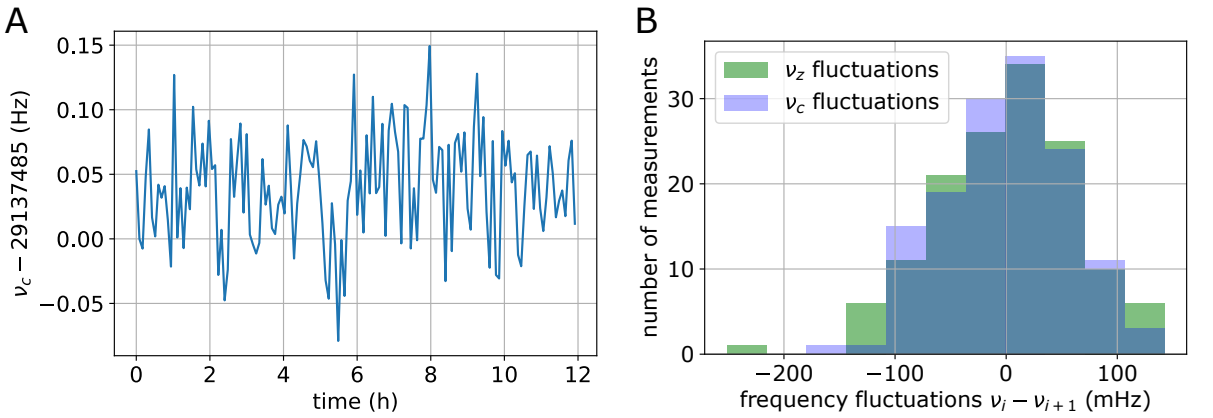

Figure 5.6. Continuous measurement of the cyclotron frequency in the PT. (A) Cyclotron frequency as function of time. (B) Histogram of the difference of subsequent determinations of the axial frequency (green) and cyclotron frequency (blue).

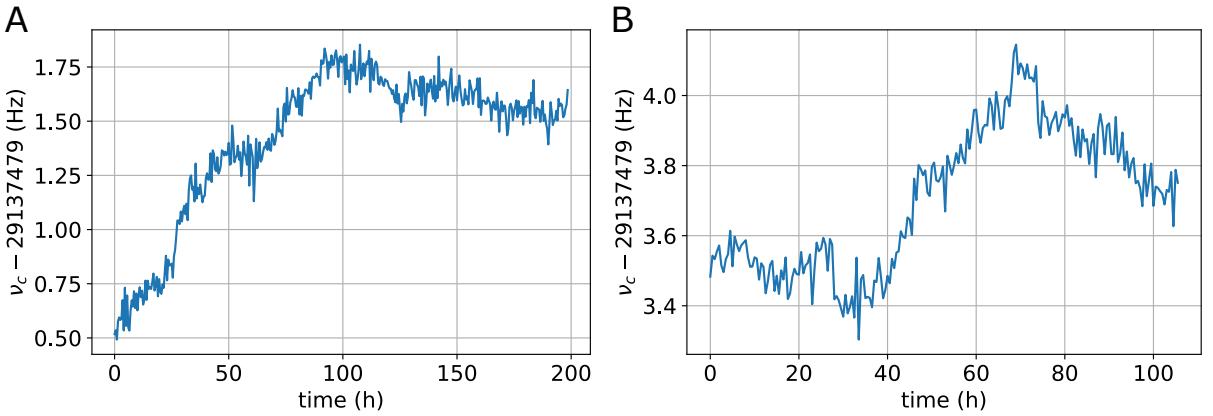

Figure 5.7. Long term drift of the magnetic field in the PT detected during two long doubletrap-measurement runs.

equal to $\Delta\nu_c/\nu_c < 4 \cdot 10^{-11}$ per double-dip averaging time of 180 s and thus not limiting the uncertainty of the measured g-factors and E_{HFS}.

5.1.5 HFS resonances

The linewiths due to $B_{2,\mathrm{PT}}$ of the electronic transitions ($|1\rangle \leftrightarrow |3\rangle$ and $|2\rangle \leftrightarrow |4\rangle$) and nuclear transitions ($|1\rangle \leftrightarrow |2\rangle$ and $|3\rangle \leftrightarrow |4\rangle$) are

$$\frac{\Delta\omega_e^{\mathrm{PT}}}{2\pi} = 101(10)\ \mathrm{Hz} \text{ and } \frac{\Delta\omega_n^{\mathrm{PT}}}{2\pi} = 0.19(2)\ \mathrm{Hz}, \tag{5.14}$$

respectively. As described in the chapter 3, the total width of the lineshape at low microwave power is therefore dominated by the Gaussian profile of the cyclotron measurement, and has a width $2 \cdot 10^{-9}$ for the electronic transitions and $1.5 \cdot 10^{-9}$ for the nuclear transitions, respectively, due to the different scaling with the magnetic field.

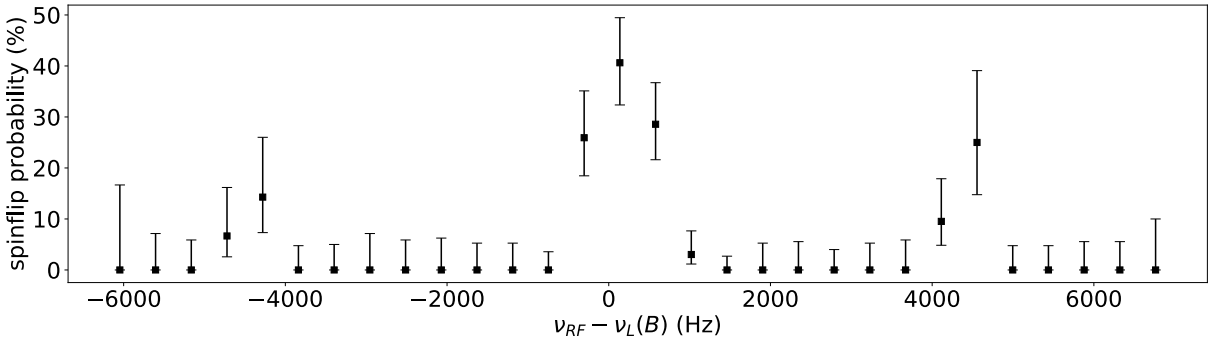

Figure 5.8. Resonance of the transition $|1\rangle \leftrightarrow |3\rangle$ in the PT with magnetron sidebands. The x-axis is the difference of the applied microwave drive frequency and the theoretically expected resonance frequency for the simultaneously measured magnetic field.

The HFS transition resonance curves in the PT are determined around the expected resonance frequency for the measured magnetic field using the double-trap method described in Sec. 3.2. Initially, this requires approximate theoretical values for the electronic and nuclear magnetic moments and zero-field hyperfine splitting appearing in the Breit-Rabi equation Eq. (3.4), taking into account bound QED corrections due to the small linewidths. From the ^{3}He NMR measurements [10] and the theoretical shielding due to both electrons [60] follows the bare nuclear magnetic moment with a precision of 12 ppb. The correction factors for the bare nuclear magnetic moment and the free electron magnetic moment in the $^3He^+$ ion, which are of the order 10^{-5}, were then calculated using the expression given in [61]. From the results, $\mu'_e \approx -9.284\,106\,759 \cdot 10^{-24}$ J/T and $\mu'_I \approx -1.074\,579\,37 \cdot 10^{-24}$ J/T, and the only previous measurement for the ^{3}He zero-field splitting $E_{\mathrm{HFS}} = -8\,665\,649\,867(10)$ Hz [62] follow the expected resonance frequencies in the PT at the measured cyclotron frequency. The first resonance, plotted in Fig. 5.8, was scanned with a wider range of excitation frequencies compared to the rest of the data discussed in the next chapter. As seen in Fig. 5.8, sidebands are visible at $\nu_{res} \pm \nu_-$, possibly due to a radial magnetic field inhomogeneity causing a frequency modulation of the transition frequency with the magnetron frequency.

5.2 Analysis trap

5.2.1 Tuning ratio

In the analysis trap, the ring voltage at which the ion is in resonance with the detector as well as the optimal tuning ratio are dependent on the radial energy. This is due to the inhomogeneities B_2 and B_4, which due to the ion's magnetic moment along the z-axis $\mu_\pm = E_\pm/B_0$ effectively contribute to C_2 and C_4, respectively, see Sec. 2.3. The ring

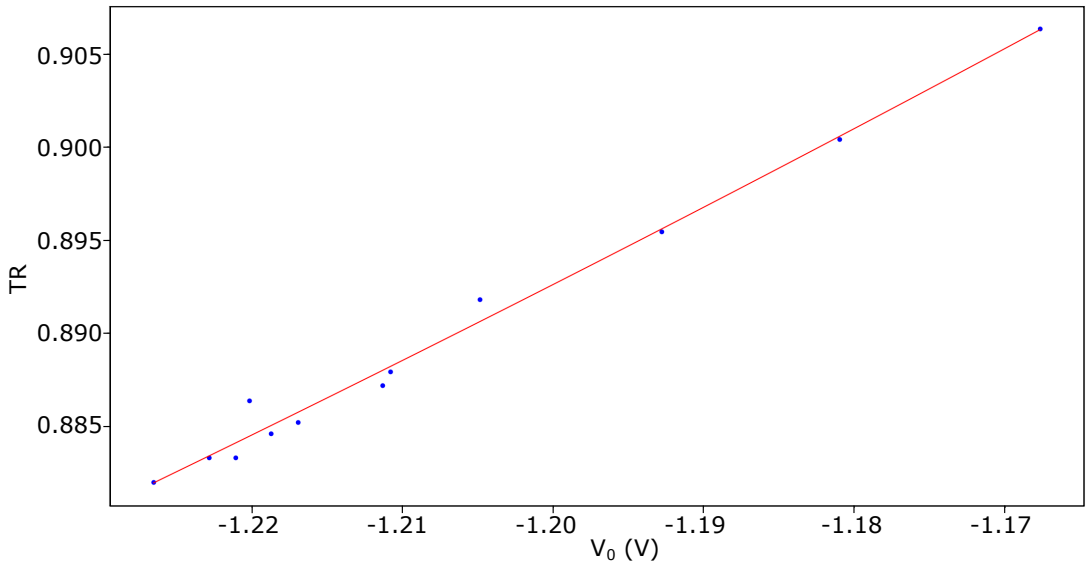

Figure 5.9. Optimized tuning ratio TR and ring voltage V_0 for different cyclotron energies in the AT.

voltages and tuning ratios at different cyclotron energies were characterized by optimizing the signal-to-noise ratio of the dip in the AT after thermalizing the cyclotron mode by sideband coupling in the PT, see Fig. 5.9. The ring voltage V_{min} at minimal cyclotron energy corresponds to $C_{2,\mathrm{AT}} = 112342(1)$ mm^{-2}. In each cycle of the double-trap measurements of the g-factors and E_{HFS}, the ring voltages V_0 with the tuning ratio $TR(V_0)$ according to Fig. 5.9 are scanned after transport to the AT. With the feedback cooling mentioned above, the spread of axial frequencies is reduced to $\Delta\nu_z(T_+) = 600$ Hz. The ion is first located within ≤ 300 Hz by scanning the voltages starting at $V_{min} = -1.23$ V while applying parametric excitation of the axial mode close to the $2 \cdot \nu_{res}$, until a peak is detected on the axial detector. The ring voltage is then further increased until a dip can be fitted and centered on the resonator.

5.2.2 Magnetic field and electronic transition resonances

The ion's axial motion in the magnetical field $B(z) = B_{0,\mathrm{AT}} + B_{2,\mathrm{AT}}z^2$ of the AT leads to a relative linewidth of the cyclotron frequency as well as the resonance frequencies of both electronic transitions of $\Delta\nu/\nu = 10^{-4}$. The modified cyclotron frequency is measured by exciting this mode directly at a low amplitude, which leads to an observable jump of the axial frequency when energy is absorbed resonantly. The excitation frequencies ν_{exc} are scanned from low to high frequencies, starting below the value for ν_+ estimated for the center of the AT from the magnetic field in the PT and the magnetic bottle. As seen in Fig. 5.10 A, an axial frequency jump is observed at the modified cyclotron frequency $\nu_+ \approx 27.6658$ MHz corresponding to $B_{0,\mathrm{AT}}$ and at higher frequencies due to the cyclotron

linewidth. Fig. 5.10 A shows an additional smaller jump at the lower magnetron sideband around $\nu_{exc} \approx \nu_+ - 4$ kHz. The magnetron frequency, which is only weakly dependent on the magnetic field, was additionally determined from a double-dip spectrum to be $\nu_- = 3969(1)$ Hz. It follows the magnetic field at the center of the magnetic bottle $B_{0,\mathrm{AT}} = 5.43352(4)$, which is then used to estimate the resonance frequencies of the electronic transitions in the AT, $\nu_{13} \approx 148.054$ GHz and $\nu_{24} \approx 156.719$ GHz. With a drive at these frequencies applied to the ion in the AT, the axial frequency jumps as depicted in Fig. 5.10 B could be observed, which can be interpreted as a change of the ion's magnetic moment due to the HFS transition. These axial frequency jumps $\Delta\nu_{\mathrm{z,SF}} = 22.638(5)$ Hz correspond to a magnetic bottle of $B_{2,\mathrm{AT}} = 124.119(27)$ kT/m^2. For both transitions resonance curves were measured, which allow to optimize the efficiency with which these transitions can be driven in the AT during the double-trap measurement. Fig. 5.10 C and Fig. 5.10 D show the resonances of transitions $|1\rangle \leftrightarrow |3\rangle$ and $|2\rangle \leftrightarrow |4\rangle$, respectively, where the plotted transition probabilities $P_{SF}(\nu_{RF})$ where determined from 40 attempts at each frequency step with a 0 dbm drive applied for 1 s. The fitted lines following Eq. (3.14), depicted in red in Fig. 5.10 C and D, yield the linewidths $\Delta\omega_{13}^{\mathrm{AT}}/(2\pi) = 8(1)$ MHz and $\Delta\omega_{24}^{\mathrm{AT}}/(2\pi) = 11(1)$ MHz, which gives an estimate for the axial temperature via the theoretical value $\Delta\omega_e^{\mathrm{AT}}/(2\pi) = T_{\mathrm{z,AT}} \cdot 1.088(3)\ \mathrm{MHz\,K^{-1}}$.

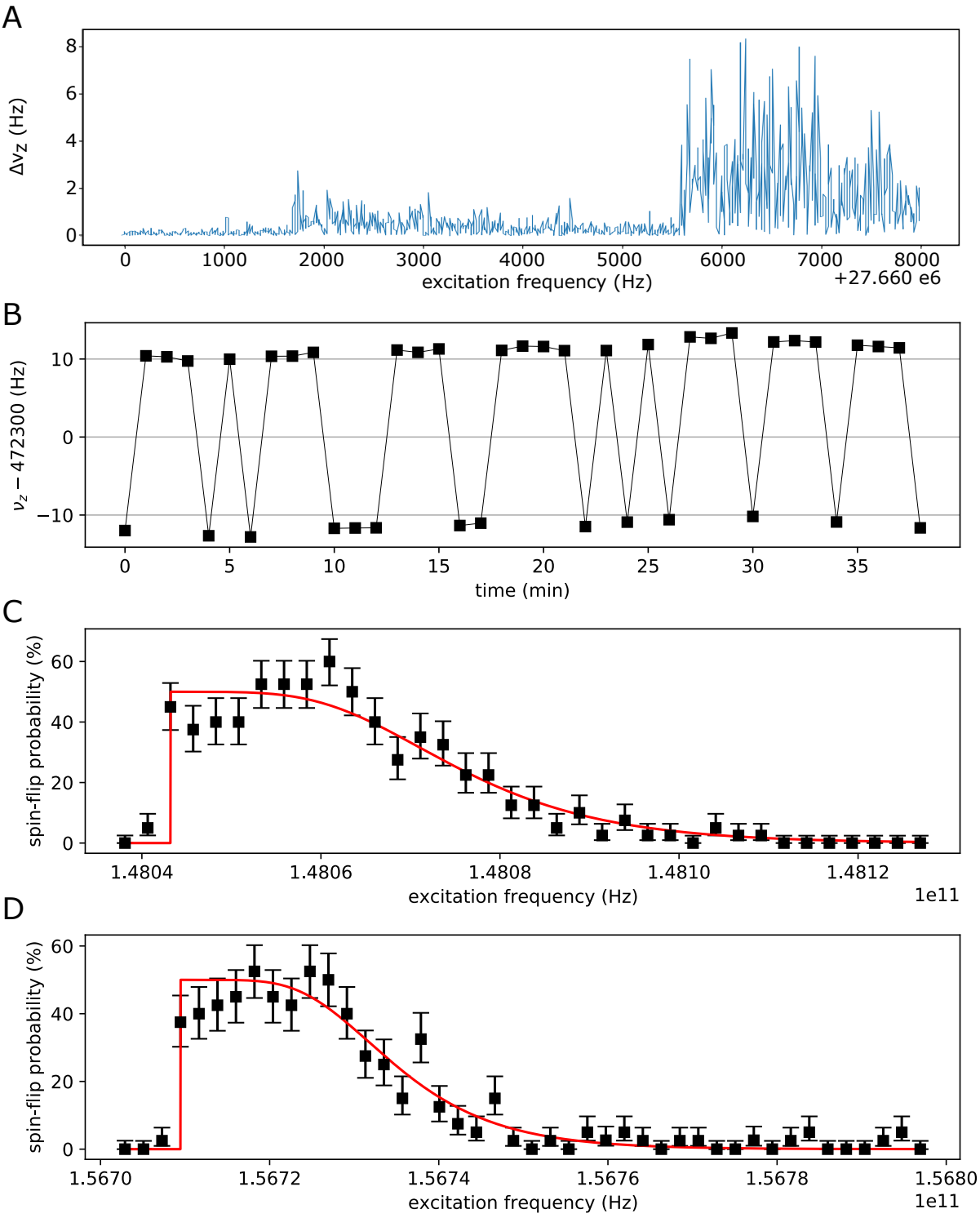

Figure 5.10. (A) Axial frequency shift in the AT after exciting the modified cyclotron mode. (B) Axial frequency jumps in the AT when driving the electronic transition $|1\rangle \leftrightarrow |3\rangle$. (C) and (D) Resonance curves of the electronic transition $|1\rangle \leftrightarrow |3\rangle$ and $|2\rangle \leftrightarrow |4\rangle$ in the AT. The red lines are fits with the lineshape given in Eq. (3.14).

Chapter 6

g-Factor and E_{HFS} Measurement Results

In the following, the zero-field splitting and the g-factors rather than the magnetic moments of $^3\mathrm{He}^+$ are determined directly. This allows to reformulate the HFS state energies $E_i\left(\mu_e, \mu_I, E_{\mathrm{HFS}}, B\right)$ in Eq. (3.4) combined with the measured magnetic field $B = m_{^3He^+}\omega_c/e$ in terms of mass ratios instead of masses in units of kg with relative uncertainty $3 \cdot 10^{-10}$ [63]. With the definition

$$E = \hbar\omega_c \frac{m_{^3He^+}}{4m_e}, \tag{6.1}$$

the eigenenergies can be expressed as

$$\begin{aligned} E_{1,4}\left(\omega_c, g_e, g_I', E_{\mathrm{HFS}}\right) &= \frac{E_{\mathrm{HFS}}}{4} \mp \left(g_e + g_I' \frac{m_e}{m_p}\right) E\,, \\ E_{2,3}\left(\omega_c, g_e, g_I', E_{\mathrm{HFS}}\right) &= -\frac{E_{\mathrm{HFS}}}{4} \pm \sqrt{\left(\frac{E_{\mathrm{HFS}}}{2}\right)^2 + \left(-g_e + g_I' \frac{m_e}{m_p}\right)^2 E^2}\,. \end{aligned} \tag{6.2}$$

The electron mass m_e and proton mass m_p in atomic mass units are known with relative precisions of $2.9 \cdot 10^{-11}$ and $5.3 \cdot 10^{-11}$, respectively [24, 63, 64]. The $^3\mathrm{He}^+$ mass $m_{^3He^+} = 3.015\,480\,768\,667(97)\ u$ used here was determined from the helion mass [63] corrected for the additional electron mass [63] and second ionization energy [63], so that the uncertainties of the mass ratios are negligible for the total systematic uncertainty given below. The $^3\mathrm{He}$ mass given in the recent atomic mass evaluation [65] corrected for the missing electron mass [63] and first ionization energy [66] leads to $m'_{^3He^+} = 3.015\,480\,768\,452(60)\ u$, which deviates from the value above by 1.9 σ. Using $m'_{^3He^+}$ instead would change the results by $\delta g_e/g_e = 7 \cdot 10^{-11}$, $\delta g_I'/g_I' = 1 \cdot 10^{-10}$ and $\delta E_{\mathrm{HFS}}/E_{\mathrm{HFS}} = 3 \cdot 10^{-13}$, one order of magnitude less than their total uncertainty given in Sec. 6.4.

6.1 Maximum likelihood fit procedure

Each measurement cycle n starts with a first cyclotron measurement $\omega_{c,n}^{(0)}$ in the PT. Afterwards a microwave frequency $\omega_{MW,n}$ is randomly picked from a uniform and continuous distribution of detunings from the expected resonance frequency $\omega_{ij}(\omega_{c,n}^{(0)}, g_e^{\text{theo}}, g'_{I,\text{ref}}, E_{\text{HFS,ref}}) = |E_i - E_j|/\hbar$. At this frequency $\omega_{MW,n}$ a hyperfine transition is excited while a second cyclotron measurement $\omega_{c,n}^{(1)}$ is performed simultaneously. It follows a third cyclotron measurement $\omega_{c,n}^{(2)}$ to investigate systematic effects. The detuning $\Delta = \omega_{MW,n} - \omega_{ij}(\omega_{c,n}^{(1)}, g_e^{\text{theo}}, g'_{I,\text{ref}}, E_{\text{HFS,ref}})$ during spin-flip excitation can then be calculated from the second cyclotron frequency measurement. For visual representation of the resonance curve, the resulting spin-flip probabilities are binned into appropriate intervals of the detuning defined in this way. However, this binned detuning depends on the expected parameters g_e^{theo}, $g'_{I,\text{ref}}$ and $E_{\text{HFS,ref}}$ and can thus not be used to fit the resonance line with the least square method. By this method the result would also depend on the chosen bin width, leading to an additional systematic uncertainty. Furthermore, the error assigned to the binned data points is determined by the binomial probability distribution and thus asymmetric, while the nonlinear regression based on the least squares method assumes normally distributed errors. Therefore, the maximum likelihood method is chosen instead, where the statistical probability of the complete set of detunings as a function of a set of lineshape parameters is optimized. For this purpose, the set of lineshape parameters is found which maximizes the log-likelihood function

$$\mathcal{L} = \sum_n \ln(p_n), \tag{6.3}$$

defined as the logarithm of the probability $\prod_n p_n$ to reach the given measurement outcome in all cycles assuming these lineshape parameters. Here, the probabilities p_n are determined for a particular lineshape $\chi_{1/2}$ from $\tilde{P}_{SF,1/2}$ given in Eq. (3.23) as

$$p_n(g_e, g'_I, E_{\text{HFS}}, \Omega) = \tilde{P}_{SF,1/2}(\omega_{MW,n}, \omega_{ij}(\omega_{c,n}^{(1)}, g_e, g'_I, E_{\text{HFS}}), \Omega, \Delta\omega_{ij}^{\text{PT}}) \tag{6.4}$$

in case of a spin-flip in cycle n and accordingly in case of no spin-flip in this cycle

$$p_n(g_e, g'_I, E_{\text{HFS}}, \Omega) = 1 - \tilde{P}_{SF,1/2}(\omega_{MW,n}, \omega_{ij}(\omega_{c,n}^{(1)}, g_e, g'_I, E_{\text{HFS}}), \Omega, \Delta\omega_{ij}^{\text{PT}}). \tag{6.5}$$

When combining N measured resonance curves in one fit, the log-likelihood function accordingly is the sum of the log-likelihood functions of the individual resonances and depends simultaneously on the free parameters $\{g_e,\, g'_I,\, E_{\text{HFS}},\, \Omega_1, ...,\, \Omega_N\}$. To simplify this, the two parameters g'_I and E_{HFS} are determined by combining one resonance curve of each of the two nuclear transitions using the theoretical electron g-factor (Eq. (6.21)), as the nuclear transition frequencies depend only weakly on g_e. The electron g-factor

is subsequently fitted using only one resonance curve of an electronic transition with g'_I and E_{HFS} fixed at the measured values. Changing the fixed parameters by 3σ of the theoretical g_e or the measured g'_I and E_{HFS}, respectively, leads to a shift of the result which is more than two orders of magnitude smaller than its statistical uncertainty.

6.2 Lineshape uncertainty

The resonance curves of the four transitions were measured several times for different microwave powers and are plotted in the appendix. Fitting the electronic resonances with the maximum likelihood procedure using either $\tilde{P}_{SF,1/2}$ or the Gaussian lineshape

$$P_{SF,G}(\omega_{MW}, \omega_{ij}(\omega_c, g_e, g'_I, E_{\mathrm{HFS}}), \sigma, p_{\max}) = p_{\max} \exp\left(\frac{-(\omega_{MW} - \omega_{ij}(\omega_c, g_e, g'_I, E_{\mathrm{HFS}}))^2}{2\sigma^2}\right) \tag{6.6}$$

leads to the results in Fig. 6.1. For high microwave powers, or Rabi frequencies, the electron g-factors fitted with the different lineshapes deviate significantly from each other. At low microwave powers the results using $\tilde{P}_{SF,1/2}$ or $P_{SF,G}$ agree, as in this case the Gaussian distribution of the magnetic field measurement in the convolution in Eq. (3.23) dominates the lineshapes $\tilde{P}_{SF,1/2}$, compare Fig. 3.2 (E) and (F). The deviation of $\tilde{P}_{SF,1/2}$ from a Gaussian $P_{SF,G}$ is plotted as function of the Rabi frequency in Fig. 6.2. Here, the two possible spin-flip probabilities $\tilde{P}_{SF,1/2}$ for different Rabi frequencies are fitted with a Gaussian line to determine the shift of the center frequency and correspondent difference of the deduced parameters g_e, g'_I and E_{HFS}.

For the final results each resonance is fitted with a Gaussian and ascribed a systematic uncertainty given by the maximum of the differences between a fit with a Gaussian and with $\tilde{P}_{1/2}$, as calculated in Fig. 6.2. In case of g_e only the three resonances at lowest amplitude, where the lineshape uncertainty is $\delta g_e/g_e = 1.5 \cdot 10^{-10}$, are taken into account for the final value. As shown in Fig. 6.2, the systematic shifts of the two nuclear transitions $|1\rangle \leftrightarrow |2\rangle$ and $|3\rangle \leftrightarrow |4\rangle$ that are combined in one fit largely cancel for E_{HFS} but not for g'_I. This is also indicated by the difference between the results measured at different amplitudes plotted in Fig. 6.3, while not with statistical significance. The conservative uncertainties due to lineshape ascribed to the three measurements according to the Rabi frequencies and Fig. 6.2 are summarized in Tab. 6.1.

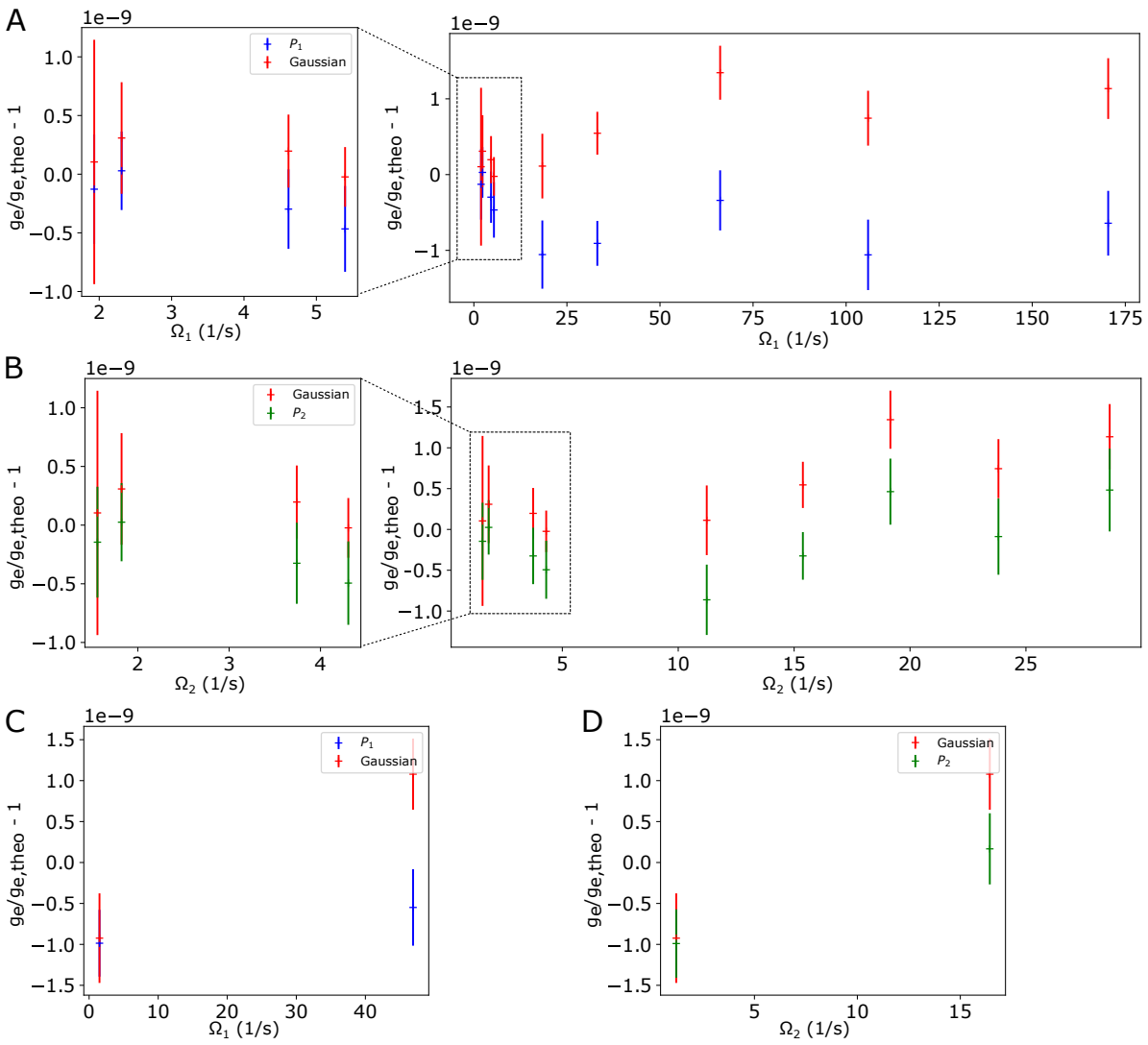

Figure 6.1. (A) and (B): transition $|2\rangle \leftrightarrow |4\rangle$. (C) and (D): transition $|1\rangle \leftrightarrow |3\rangle$. Shown is the electron g-factor fitted with a Gaussian or functions $\tilde{P}_{1/2}$ from Eq. (3.23) which is convoluted with a Gaussian. The x-axis is the Rabi frequency fitted with the respective lineshapes. The graphs on the left side in (A) and (B) show only the smallest Rabi frequencies, where the results for different lineshapes agree.

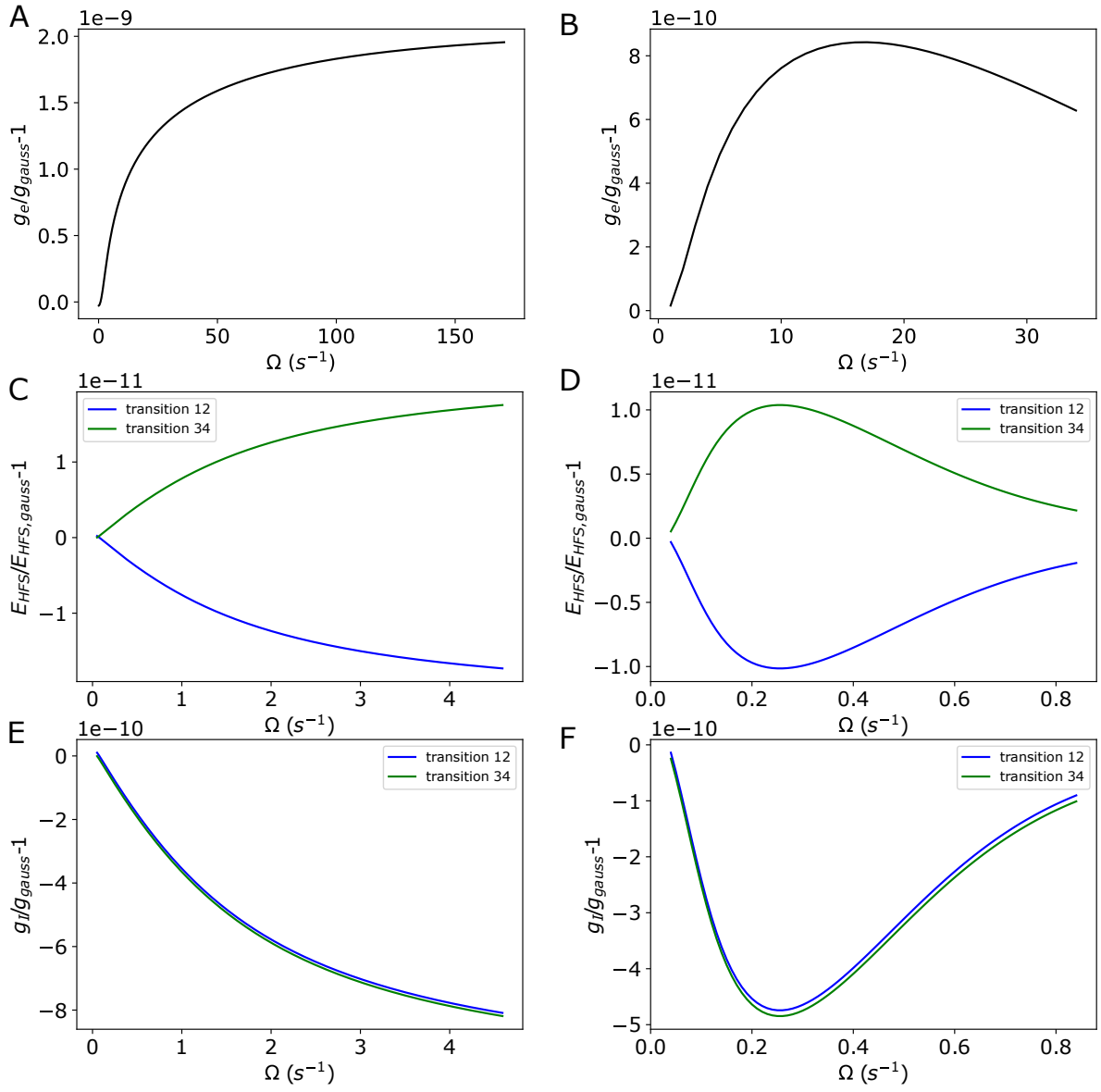

Figure 6.2. Difference of the fitted electron g-factor, nuclear g-factor and E_{HFS} with the models P_1 (A,C,E) and P_2 (B,D,F) compared to a Gaussian as a function of the Rabi frequency extracted from the fit.

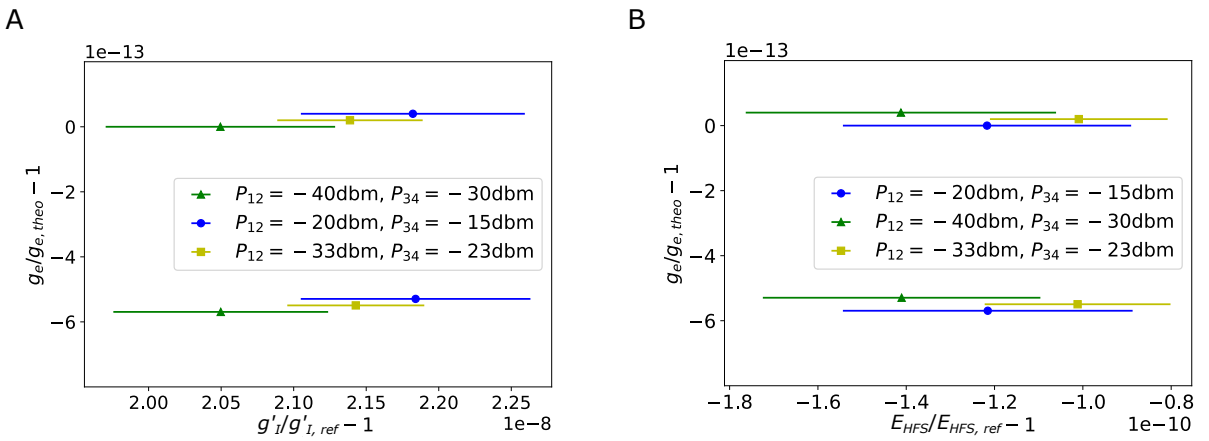

Figure 6.3. Results for (A) the shielded nuclear g-factor and (B) the zero-field hyperfine splitting with a maximum likelihood fit of a Gaussian, combining one resonance of each of the two nuclear transitions with microwave powers P_{12} and P_{34}. The y-axis gives the value assumed for g_e in the fit of g'_I and E_{HFS}. The results are plotted for $g_e = g_{e,theo}$ and for $g_e = g_{e,theo}(1 - 6 \cdot 10^{-13})$, which corresponds to a difference of 3σ of the theoretical value. In order to make the overlapping errorbars better visible, the datapoints are depicted slightly shifted from these two values along the y-axis. Changing g_e by 3σ shifts the fitted g'_I and E_{HFS} by two orders of magnitude less than their statistical uncertainties. For the final results, g_e is fixed to the theoretical value while the less precise experimental g_e would not significantly affect the result.

Table 6.1. Fit results for the Rabi frequencies Ω_1 and Ω_2 of the two measured nuclear transitions assuming lineshapes χ_1 and χ_2, respectively, which correspond to a systematic uncertainty shown in Fig. 6.2. As g_I and E_{HFS} are determined from a combined fit of one resonance of each nuclear transition, the combined uncertainty of both transitions are given for these parameters.

amplitude (dbm)	transition	Ω_1 (1/s)	Ω_2 (1/s)	$\delta g_I/g_I$	$\delta E_{\mathrm{HFS}}/E_{\mathrm{HFS}}$
−20	12	3.8(7)	0.76(7)		
−15	34	1.9(4)	0.53(6)	$7 \cdot 10^{-10}$	$5 \cdot 10^{-12}$
−33	12	0.9(2)	0.29(5)		
−23	34	0.5(1)	0.20(4)	$5 \cdot 10^{-10}$	$1 \cdot 10^{-12}$
−40	12	0.33(8)	0.15(3)		
−30	34	0.30(8)	0.13(3)	$4 \cdot 10^{-10}$	$1 \cdot 10^{-12}$

6.3 Systematic shifts of the eigenfrequencies

In this section, corrections of the fitted g-factors and zero-field splitting due to systematic shifts of the measured magnetic field are determined.
The resonant drive frequency during sideband coupling of the axial and cyclotron mode in case of systematic shifts $\Delta\nu_z$ and $\Delta\nu_+$ is $\nu_{\mathrm{RF}}(\delta = 0) = \nu_+ + \Delta\nu_+ - (\nu_z + \Delta\nu_+)$. The modified cyclotron frequency follows as

$$\begin{aligned}
\nu_{+,\mathrm{meas}} &= \nu_{\mathrm{l,meas}}(\delta) + \nu_{\mathrm{r,meas}}(\delta) - \nu_{\mathrm{z,meas}} + \nu_{\mathrm{RF}}(\delta) \\
&= \left(\nu_z + \Delta\nu_z - \frac{\delta}{4\pi} - \frac{\sqrt{\Omega^2+\delta^2}}{4\pi}\right) + \left(\nu_z + \Delta\nu_z - \frac{\delta}{4\pi} + \frac{\sqrt{\Omega^2+\delta^2}}{4\pi}\right) \\
&- (\nu_z + \Delta\nu_z) + \left(\nu_+ + \Delta\nu_+ - \nu_z - \Delta\nu_z + \frac{\delta}{2\pi}\right) \\
&= \nu_+ + \Delta\nu_+ \,, \qquad (6.7)
\end{aligned}$$

independently of the detuning δ of the drive from resonance. Thus, the measured value is shifted by $\Delta\nu_+$ while the systematic axial frequency shift cancels. The equivalent holds for the determination of the magnetron frequency via sideband coupling, while magnetron shifts are negligible for the extracted magnetic field due to $\nu_- \ll \nu_+$. The cyclotron frequency calculated via the invariance theorem Eq. (2.6), and therefore also the measured magnetic field are shifted by a factor

$$\begin{aligned}
\frac{\Delta\nu_c}{\nu_c} &= \frac{\sqrt{(\nu_+ + \Delta\nu_+)^2 + (\nu_z + \Delta\nu_z)^2 + (\nu_- + \Delta\nu_-)^2} - \nu_c}{\nu_c} \\
&\approx \frac{\nu_+\Delta\nu_+ + \nu_z\Delta\nu_z}{\nu_c^2}. \qquad (6.8)
\end{aligned}$$

When extracting the electron g-factor from the resonance frequencies of one of the transitions $|1\rangle \leftrightarrow |3\rangle$ and $|2\rangle \leftrightarrow |4\rangle$, this leads to the same relative shift for this parameter:

$$\begin{aligned}
\Delta g_e &= -\Delta\nu_c \frac{d\nu_{13}}{d\nu_c}\left(\frac{d\nu_{13}}{dg_e}\right)^{-1} \\
&= -\Delta\nu_c \frac{d\nu_{24}}{d\nu_c}\left(\frac{d\nu_{24}}{dg_e}\right)^{-1} \\
&= -1.00 \cdot \Delta\nu_c \frac{g_e}{\nu_c}\,. \qquad (6.9)
\end{aligned}$$

Similarly, for the nuclear g-factor determined from both nuclear transitions

$$\begin{aligned}
\Delta g_I' &= -\Delta\nu_c \frac{d\nu_{12}}{d\nu_c}\left(\frac{d\nu_{12}}{dg_I'}\right)^{-1} \\
&= -\Delta\nu_c \frac{d\nu_{34}}{d\nu_c}\left(\frac{d\nu_{34}}{dg_I'}\right)^{-1} \\
&= -1.60 \cdot \Delta\nu_c \frac{g_I'}{\nu_c}\,. \qquad (6.10)
\end{aligned}$$

The result for the zero-field splitting is weakly dependent on the magnetic field and furthermore the shift of both nuclear transitions mostly compensate due to

$$\frac{d\nu_{12}}{d\nu_c}\left(\frac{d\nu_{12}}{dE_{\mathrm{HFS}}}\right)^{-1} \approx \frac{-d\nu_{34}}{d\nu_c}\left(\frac{d\nu_{34}}{dE_{\mathrm{HFS}}}\right)^{-1} = 0.07\cdot\Delta\nu_c\frac{E_{\mathrm{HFS}}}{\nu_c}\,. \tag{6.11}$$

Therefore when combining the two nuclear resonances measured alternatingly in the same measurement run in one fit of g_I and E_{HFS} this averages to

$$\begin{aligned}\Delta E_{\mathrm{HFS}} &= -\Delta\nu_c\frac{1}{2}\left(\frac{d\nu_{12}}{d\nu_c}\left(\frac{d\nu_{12}}{dE_{\mathrm{HFS}}}\right)^{-1} + \frac{d\nu_{34}}{d\nu_c}\left(\frac{d\nu_{34}}{dE_{\mathrm{HFS}}}\right)^{-1}\right)\\ &= -4.02\cdot10^{-3}\cdot\Delta\nu_c\frac{E_{\mathrm{HFS}}}{\nu_c}\,.\end{aligned} \tag{6.12}$$

The results are accordingly corrected by factors $1-\Delta E_{\mathrm{HFS}}/E_{\mathrm{HFS}}$, $1-\Delta g_e/g_e$ or $1-\Delta g_I'/g_I'$ for the systematic effects described below, as summarized in Tab. 6.2.

Image charge

The electrostatic field generated by the image charges that are induced in the trap electrodes by the ion shifts the radial eigenfrequencies by [67]

$$\Delta\nu_{\pm} = \mp\frac{e^2}{8\pi^2\epsilon_0 m_{^3He^+}a^3\nu_c} = \mp 0.93\ \mathrm{mHz}, \tag{6.13}$$

where $a = 3.5$ mm is the trap radius.

Image current

With the damping $\gamma_{+/z}$ due to the axial or cyclotron detector, the solutions of Eq. (2.30) for $\rho_+(t)$ or $z(t)$ take the form $A\exp(-\gamma/2t)\exp\left(\sqrt{\omega_0^2-\gamma^2/4}t\right)$. Thus, the imaginary part of the damping constant leads to eigenfrequency shifts

$$\frac{\Delta\nu_{+/z}}{\nu_{+/z}} = \frac{-\,\mathrm{Im}(\gamma_{+/z})}{\omega_{+/z}} = \frac{-\Delta\omega}{\omega_{+/z}^2+4Q_{+/z}^2\Delta\omega^2}\frac{Q_{+/z}}{\tau_{+/z}}. \tag{6.14}$$

For all detunings $\Delta\omega$ of the resonator, the relative shift of the modified and therefore also the free cyclotron frequency is $|\Delta\nu_c/\nu_c| \le 3.5\cdot10^{-12}$, and $-\Delta\nu_c/\nu_c < 1\cdot10^{-12}$ when detuning the cyclotron resonator during the HFS measurements. Furthermore, a detuning $\delta\nu$ of the the axial dip from the resonator gives close to center $\Delta\nu_z/\delta\nu = -1.6\ \mathrm{mHz\,Hz^{-1}}$, and with $|\delta\nu| < 5$ Hz therefore $\Delta\nu_c/\nu_c = 0(5)\cdot10^{-12}\ \mathrm{Hz^{-1}}$.

Relativistic

The relativistic mass increase due to the ion's motion leads to a shift of the modified cyclotron mode by $\Delta\nu_+/\nu_+ = -\langle E_+\rangle/(m_{^3He^+}c^2) = 2.1(1)\cdot10^{-10}$, while shifts of the other eigenmodes and relativistic shifts of the Larmor frequency [68] can be neglected.

Magnetic field imperfections

The temperature dependent shifts of the average magnetic field are

$$\begin{aligned}\Delta B(T_z) &= \langle z^2 \rangle B_2 \\ &= 6.3(5) \cdot 10^{-10} B_0 \,, \end{aligned} \tag{6.15}$$

$$\begin{aligned}\Delta B(T_+) &= \frac{k_B T_+}{m_{^3He^+}\omega_z^2} \left(-\frac{B_1^2}{B_0} - B_2 \frac{\nu_z^2}{\nu_+^2} \right) \\ &= -1.2(1) \cdot 10^{-11} B_0 \,, \end{aligned} \tag{6.16}$$

see Sec. 2.3. This affects the microwave detuning averaged over the ion trajectory $\Delta = \omega_{MW} - \omega_{ij}(B_0 + \Delta B)$, which is taken into account by inserting the measured averaged cyclotron frequency $q/m(B_0 + \Delta B)$ into the Breit-Rabi equation and therefore does not require a correction of the extracted g-factors and E_{HFS}.

It remains the systematic shift of the axial frequency $\Delta\nu_z = B_2\langle\mu_+\rangle \propto B_2 T_+$ to be corrected for, which via the invariance theorem leads to $\Delta\nu_c/\nu_c = \nu_z \Delta\nu_z/\nu_c^2 = 1.1(1) \cdot 10^{-11}$. Here, the same T_+ during single and double dip spectra can be assumed as the cyclotron resonator is detuned so that the single-dip averaging time is 90 s $\ll \tau_{cyc}(\nu_+)$.

Electrostatic anharmonicity

The residual anharmonic term of the electrostatic potential $C_6 = 2(1) \cdot 10^{-6}$ mm^{-6} leads to a systematic axial frequency shift that corresponds to a relative cyclotron frequency shift of $\Delta\nu_c/\nu_c = -1.5(9) \cdot 10^{-12}$, according to Eqs. (2.20) and (6.8). Additionally, the uncertainty of $\Delta C_4 = D_4 \Delta T R$ due to the uncertainty of the optimal tuning ratio is taken into account, leading in total to $\Delta\nu_c/\nu_c = -1.5(2.5) \cdot 10^{-12}$.

Axial fit

The dependence of the fit result on a shift $\Delta\nu_{res}$ of the input resonator frequency is determined to $\Delta\nu_z/\Delta\nu_{res} = 9$ mHz Hz^{-1} by varying the input parameter of the axial fits. The resonator frequency in each cycle deviates by less than $\Delta\nu_{res} = \pm 5$ Hz from the assumed value, leading to a conservative estimate of $\Delta\nu_c/\nu_c = 0(3) \cdot 10^{-11}$ as given in Tab. 6.2.

Non-linear axial frequency drifts

After each transport to the PT, the eigenfrequency measurements start after a 10 min waiting period to suppress possible drifts from heating of the apparatus by the spin-flip excitation in the AT and allow voltages to settle. Systematic shifts of the measured

cyclotron frequency due to linear axial frequency drifts are cancelled, as the single dip spectra immediately before and after the double dip spectrum are averaged. The residual drift $\nu_{z1} - \nu_{z2}$ between the two frequencies that are averaged to determine the axial frequency $(\nu_{z1} + \nu_{z2})/2$ during spin-flip excitation is $\nu_{z1} - \nu_{z2} = -13(2)$ mHz combining the low amplitude electronic resonances that enter g_e and $\nu_{z1} - \nu_{z2} = -11(3)$ mHz for the nuclear resonance at lowest amplitude that enters g'_I. Taking the total drift as upper limit for the non-linear contribution implies a negligible additional systematic uncertainty of $\delta\nu_c/\nu_c < 8 \cdot 10^{-12}$. For the two nuclear resonances at higher amplitude the drift is $\nu_{z1} - \nu_{z2} = -11(3)$ mHz ($P_{12} = -33$ dbm, $P_{34} = -23$ dbm) and $\nu_{z1} - \nu_{z2} = -26(4)$ mHz ($P_{12} = -20$ dbm, $P_{34} = -15$ dbm). Assuming accordingly $\delta\nu_c/\nu_c = 1.5 \cdot 10^{-11}$ as additional systematic uncertainty for the resonance at highest microwave power does not contribute significantly to the total systematic uncertainty.

Axial amplitude modulation

The coupling of the axial and modified cyclotron modes during the double-dip measurement leads to a modulation of the axial amplitude $z(t) = z_0 \sin(\Omega_{DD} t/2) \sin(\omega_z t + \phi_0)$ and thus the magnetic field seen by the ion. The transition frequency ω_{ij} is therefore modulated with the Rabi frequency of the coupling $\Omega_{DD} = 22$ Hz, causing sidebands in the resonance. For the nuclear transitions this effect is not relevant as the modulation index is $h = \Delta\omega_{ij}/\Omega_{DD} \ll 1$. For the electronic transitions the modulation index is $h \approx 5$, however a shift of the resultant g_e is not expected as symmetric sidebands would not affect the center of the Gaussian. This has been checked by measuring the $|2\rangle \leftrightarrow |4\rangle$ resonance with and without a double-dip during the spin-flip drive at the same microwave power, giving results that agree within 1σ. In the measurement without simultaneous double-dip detection $\omega_c^{(1)}$, the cyclotron frequency was determined by averaging the measured frequencies before and after applying the drive $(\omega_c^{(0)} + \omega_c^{(2)})/2$, as these values were consistent with $\omega_c^{(1)}$ for the other measurement runs.

Table 6.2. Corrections to the nuclear g-factor, electron g-factor and zero-field hyperfine splitting due to systematic effects. The lineshape uncertainty in the last line relates to the resonances at low amplitude that enter the final result.

	$-\Delta g_I'/g_I'$ (10^{-10})	$-\Delta g_e/g_e$ (10^{-10})	$-\Delta E_{\mathrm{HFS}}/E_{\mathrm{HFS}}$ (10^{-12})
image charge	-0.514(3)	-0.321(2)	-0.128(1)
relativistic	-0.33(2)	-0.21(1)	-0.084(4)
magnetic inhomogeneity	0.17(2)	0.11(1)	0.044(4)
electrostatic anharmonicity	-0.03(5)	-0.02(3)	-0.01(1)
axial fit	0(0.5)	0(0.3)	0(0.1)
resonance lineshape	0(4)	0(1.5)	0(1)
Σ	-0.7(4.0)	-0.4(1.5)	-0.2(1.1)

6.4 Final experimental results

The bound electron g-factor of $^3\mathrm{He}^+$

$$g_e = -2.002\,177\,415\,79(34)_{stat}(30)_{sys} \tag{6.17}$$

is calculated as the weighted average of the measurements at the smallest Rabi frequencies and correcting the results for the systematic shifts. Here, two resonances of transition $|2\rangle \leftrightarrow |4\rangle$ and one of transition $|1\rangle \leftrightarrow |3\rangle$ are taken into account. The nuclear g-factor and zero-field splitting determined from all measured nuclear resonances $|1\rangle \leftrightarrow |2\rangle$ and $|3\rangle \leftrightarrow |4\rangle$ are summarized in Tab. 6.3. At lowest microwave amplitude one finds

$$g_I' = -4.255\,099\,606\,9(30)_{stat}(17)_{sys}\,, \tag{6.18}$$

$$E_{\mathrm{HFS}} = -8\,665\,649\,865.77(26)_{stat}(1)_{sys}\ \mathrm{Hz}\,. \tag{6.19}$$

6.5 Comparison to theory

6.5.1 Bound electron g-factor

The g-factor of the free electron can be expressed as the Dirac value $g_{\mathrm{Dirac}} = -2$ with QED corrections expanded in powers n of the fine-structure constant α and additional hadronic and electroweak contributions. Each term $c_n\alpha^n$ represents the sum of all n-loop QED Feynman diagrams, where the first-order term is the Schwinger term α/π. For an electron bound in a hydrogen-like ion, the leading relativistic binding term is

$$-g_{\mathrm{Dirac}} - 2 = \frac{4}{3}\left(\sqrt{1-(Z\alpha)^2} - 1\right)\,, \tag{6.20}$$

Table 6.3. Experimental results for the zero-field hyperfine splitting E_{HFS} and the shielded nuclear g-factor at different microwave powers or Rabi frequencies $\Omega_{1/2}$ according to lineshape $\tilde{P}_{1/2}$. For E_{HFS} the average of all runs is additionally given, as the effect of the lineshape asymmetry is suppressed for this parameter.

amp (dbm)	Ω_1 (1/s)	Ω_2 (1/s)	g'_I	E_{HFS} (Hz)
$P_{12} = -20$	3.8(7)	0.76(7)		
$P_{34} = -15$	1.9(4)	0.53(6)	-4.255 099 612 7$(34)_{stat}(30)_{sys}$	-8 665 649 865.94$(27)_{stat}(4)_{sys}$
$P_{12} = -33$	0.9(2)	0.29(5)		
$P_{34} = -23$	0.5(1)	0.20(4)	-4.255 099 610 8$(20)_{stat}(21)_{sys}$	-8 665 649 866.12$(18)_{stat}(1)_{sys}$
$P_{12} = -40$	0.33(8)	0.15(3)		
$P_{34} = -30$	0.30(8)	0.13(3)	-4.255 099 606 9$(30)_{stat}(17)_{sys}$	-8 665 649 865.77$(26)_{stat}(1)_{sys}$
average				-8 665 649 865.94$(14)_{stat}(2)_{sys}$

which follows from the Dirac equation for the $1s$ electron in the potential of a point-like charge Ze [69]. For low-Z ions as in case of He, the QED corrections to the value above can be calculated as the sum of the free-electron QED contributions and QED binding-terms, due to diagrams with photon exchange with the nucleus, expanded in powers of $Z\alpha$ [70–73]. Further terms correct for finite nuclear mass and size, the latter at the level of 1 ppt in $^3\mathrm{He}^+$. The sum of all contributions evaluated for $^3\mathrm{He}^+$ in [39] is

$$g_e^{\mathrm{theo}} = -2.002\,177\,416\,252\,23(39)\,, \tag{6.21}$$

where the uncertainty is dominated by α from [63] in the Schwinger term, giving $\Delta\alpha/\pi = 3.5 \cdot 10^{-13}$. The theoretical value above is three orders of magnitude more precise than the experimental result and both agree within 1σ.

6.5.2 Zero-field splitting and Zemach radius

The zero-field hyperfine splitting E_{HFS} is the difference between the hyperfine levels with the total angular momenta $F = 0$ and $F = 1$, that can be described by [74, 75]

$$\begin{aligned}\Delta E_{\mathrm{HFS}}(F) =& \alpha g_I \frac{m_e}{m_p} \frac{F(F+1) - I(I+1) - j(j+1)}{2j(j+1)} m_e c^2 (Z\alpha)^3 \mathcal{M} \\ & \times \left[A(Z\alpha) + \delta_{\mathrm{FS}} + \delta_{\mathrm{NP}} + \delta_{\mathrm{QED}} + \delta_{\mu\mathrm{VP}} + \delta_{\mathrm{hadVP}} + \delta_{\mathrm{ew}} + \delta_{\mathrm{rec}}\right] . \end{aligned} \tag{6.22}$$

Thus for the ground state with quantum numbers $j = 1/2$, $I = 1/2$:

$$\begin{aligned} E_{\mathrm{HFS}} &= \Delta E_{\mathrm{HFS}}(1) - \Delta E_{\mathrm{HFS}}(0) \\ &= E_F \left[A(Z\alpha) + \delta_{\mathrm{FS}} + \delta_{\mathrm{NP}} + \delta_{\mathrm{QED}} + \delta_{\mu\mathrm{VP}} + \delta_{\mathrm{hadVP}} + \delta_{\mathrm{ew}} + \delta_{\mathrm{rec}}\right] \end{aligned} \tag{6.23}$$

with the so-called Fermi energy

$$E_F = \alpha g_I \frac{m_e}{m_p} \frac{4}{3} m_e c^2 (Z\alpha)^3 \mathcal{M} \,. \tag{6.24}$$

Here, $A(Z\alpha) = (2\gamma+1)/(\gamma(4\gamma^2-1))$ is the relativistic factor with $\gamma = \sqrt{1-(Z\alpha)^2}$, and $\mathcal{M} = \left(1+\frac{m_e}{M_N}\right)^{-3}$ is the mass prefactor with the nuclear mass M_N. The correction terms in these equations denote finite nuclear size δ_{FS}, nuclear polarization δ_{NP}, QED δ_{QED}, muonic $\delta_{\mu\mathrm{VP}}$ and hadronic vacuum polarization δ_{hadVP}, electroweak δ_{ew} and nuclear recoil δ_{rec} contributions.

The finite-size correction δ_{FS} and the recoil correction δ_{rec} depend on both the electric and magnetic form factors of the nucleus $G_{E/M}$. The combined finite size charge and finite size magnetization distribution

$$\delta_{\mathrm{FS}} = -2\alpha Z \frac{m_e M_N}{m_e + M_N} r_{\mathrm{Z}} (1+\delta_{\mathrm{rel1}}) \delta_{\mathrm{rel2}} \tag{6.25}$$

can be expressed as the leading non-relativistic limit given by the Zemach term proportional to the Zemach radius r_Z and the relativistic corrections $\delta_{\mathrm{rel1/2}}$ [76–78]. Here, the Zemach radius is defined using the electric charge ρ_E and magnetization ρ_M distributions or in momentum space the electric $G_E(q^2)$ and magnetic $G_M(q^2)$ form factors:

$$r_Z = \int \mathrm{d}\mathbf{r}\mathrm{d}\mathbf{r}' \rho_E(\mathbf{r}) \rho_M(\mathbf{r}') |\mathbf{r}-\mathbf{r}'| \tag{6.26}$$

$$= -\frac{4}{\pi} \int_0^\infty \frac{\mathrm{d}q}{q^2} \left(\frac{1}{1+\kappa} G_E(q^2) G_M(q^2) - 1 \right) , \tag{6.27}$$

with $G_M(0) = 1+\kappa$ and the anomalous magnetic moment of the nucleus $(1+\kappa)/M_N = g_I/(2Zm_p)$. The Zemach radius as well as the charge and magnetic root-mean-square (rms) radii are deduced from elastic electron scattering experiments [79] to be

$$r_Z = 2.528(16)\ \mathrm{fm}\,, \sqrt{\langle r^2 \rangle_E} = 1.973(14)\ \mathrm{fm}\,, \sqrt{\langle r^2 \rangle_M} = 1.976(47)\ \mathrm{fm}. \tag{6.28}$$

The latter two are defined by

$$\langle r^2 \rangle_E = \int \mathrm{d}\mathbf{r} \rho_E(\mathbf{r}) r^2 = -6 \left. \frac{\mathrm{d}}{\mathrm{d}q^2} G_E(q^2) \right|_{q^2=0} \tag{6.29}$$

$$\langle r^2 \rangle_M = \int \mathrm{d}\mathbf{r} \rho_M(\mathbf{r}) r^2 = -\frac{6}{1+\kappa} \left. \frac{\mathrm{d}}{\mathrm{d}q^2} G_M(q^2) \right|_{q^2=0} . \tag{6.30}$$

Aside from electron scattering data, the charge radius of ^{3}He can also be determined from that of ^{4}He [80] combined with the measured isotope shift of the $2^3\mathrm{S} - 2^3\mathrm{P}$ and $2^3\mathrm{S} - 2^1\mathrm{S}$ transitions. However, currently the results of several such determinations differ by 4σ [81–84].

Evaluating all contributions to E_{HFS} with the finite-size and recoil terms based on the radii in Eq. (6.28) leads to [39]

$$E_{\mathrm{HFS}}^{\mathrm{theo}} = -8\,665\,701(19)\ \mathrm{kHz}. \tag{6.31}$$

Here, the uncertainty is in equal parts due to the Zemach radius in δ_{FS}, uncalculated contributions to δ_{rec} of higher orders in the electron-nucleus mass ratio and a conservative estimate for the uncertainty of the nuclear polarization correction δ_{NP}. Contributions to the uncertainties of $\delta_{\mathrm{rel}1/2}$ and δ_{rec} due to different nuclear model form factors $G_{E/M}(q)$, which were adjusted to fulfill the rms radii in Eq. (6.28), are small in comparison.

Alternatively, the experimental result $E_{\mathrm{HFS}}^{\mathrm{exp}} = -8\,665\,649\,865.77(26)_{stat}(1)_{sys}$ Hz can be inserted to determine the relevant $G_{E/M}$-dependent correction terms via

$$\delta_{\mathrm{FS}} + \delta_{\mathrm{rec}} = \frac{E_{\mathrm{HFS}}^{\mathrm{exp}}}{E_F} - A(Z\alpha) - \delta_{\mathrm{NP}} - \delta_{\mathrm{QED}} - \delta_{\mu\mathrm{VP}} - \delta_{\mathrm{hadVP}} - \delta_{\mathrm{ew}}\,. \tag{6.32}$$

It follows the Zemach radius [39]

$$r_Z^{\mathrm{theo}} = 2.608(24)\ \mathrm{fm} \tag{6.33}$$

and magnetic rms radius $\sqrt{\langle r^2\rangle_M} = 2.15(4)$ fm by assuming the charge radius $\sqrt{\langle r^2\rangle_E}$ from Eq. (6.28). As in $E_{\mathrm{HFS}}^{\mathrm{theo}}$ above, the dependence of δ_{rec} on different realistic model form factors is taken into account in the uncertainty.

The Zemach radius calculated from $E_{\mathrm{HFS}}^{\mathrm{exp}}$ and the value from electron scattering data differ by 2.8σ. The difference between the theoretically calculated $E_{\mathrm{HFS}}^{\mathrm{theo}}$ above and the experimental value is 6 ppm. In a previous theoretical work, the discrepancy is 46 ppm [85]. In [86], a difference of 222 ppm between the QED prediction and the previous experimental value $E_{\mathrm{HFS}} = -8\,665\,649\,867(10)$ [62] is taken as an estimate of contributions to HFS due to nuclear effects.

6.6 Bare nuclear g-factor and shielded nuclear g-factor in atomic ^{3}He

The modification of the coupling of the nuclear magnetic moment to the external magnetic field due to the electrons in an ion or atom is parameterized as $g_I' = (1-\sigma)g_I$, with the diamagnetic shielding σ that contains contributions analogous to the theory of the bound g_e and of E_{HFS}. In case of singly or doubly ionized ^{3}He, only QED and recoil corrections are relevant at the current precision with negligible nuclear size contributions, so that the uncertainties of the values given in the following are dominated by uncalculated higher

order QED terms. Theoretical results for $^3He^+$

$$\sigma_{^3He^+} = 35.507\,38(3) \cdot 10^{-6} \tag{6.34}$$

$$\sigma_{^3He^+} = 35.507\,434(9) \cdot 10^{-6} \tag{6.35}$$

were evaluated in [39] and [11], respectively. The shielding in atomic ^{3}He $\sigma_{^3He} = 59.967\,43(10) \cdot 10^{-6}$ was calculated in [87] and more recently in [11]

$$\sigma_{^3He} = 59.967\,029(23) \cdot 10^{-6}. \tag{6.36}$$

Here, the 4σ discrepancy is due to an updated QED theory of order $\alpha^2(Z\alpha)^3$ in [11], which also accounts for the 1.6σ difference between Eqs. (6.34) and (6.35). This difference is negligible compared to the experimental uncertainty when calculating the g-factor of $^3He^{2+}$. From the measured $g'_I = -4.255\,099\,606\,9(30)_{stat}(17)_{sys}$ and Eq. (6.35) follows the g-factor of the bare nucleus

$$\begin{aligned} g_I &= \frac{g'_I}{1 - \sigma_{^3He^+}} \\ &= -4.255\,250\,699\,9(30)_{stat}(17)_{sys}\,, \end{aligned} \tag{6.37}$$

or $g_I = -4.255\,250\,699\,7(30)_{stat}(17)_{sys}(1)_{theo}$ with Eq. (6.34). The shielded magnetic moment relevant for the ^{3}He NMR frequency $\nu'_{^3He} \propto \mu_{^3He}$ therefore is

$$\begin{aligned} \mu_{^3He} &= \mu_N/2 \cdot g_I(1 - \sigma_{^3He}) \\ &= -1.074\,553\,111\,92(93) \cdot 10^{-26}\ \mathrm{J\,T^{-1}}\,, \end{aligned} \tag{6.38}$$

limited by the uncertainty of g'_I. Here, Eq. (6.37), Eq.(6.36) and the nuclear magneton μ_N, which has a relative uncertainty of $3.1 \cdot 10^{-10}$ [63] are used.

6.6.1 Comparison to NMR measurements

The CODATA [63] value for the shielded magnetic moment

$$\mu_{^3He}^{\mathrm{codata}} = -1.074\,553\,090(13) \cdot 10^{-26}\ \mathrm{J\,T^{-1}} \tag{6.39}$$

differs from the result above by 21 ppb, or 1.7 σ. It is based on the NMR frequency ratio of ^{3}He and protons in water [9]

$$\frac{\nu'_{^3He}}{\nu'_{H_2O}(25°C)} = 0.761\,786\,131\,3(33) \tag{6.40}$$

and the shielding of protons in a spherical H_2O probe at 25°C $\sigma_{H_2O}^{\mathrm{codata}} = 25.689(11) \cdot 10^{-6}$. The latter follows from the ratio of the water NMR frequency at 34.7°C to the

hydrogen-maser frequency [88] and the separately measured temperature dependence of the shielding factor $d(1-\sigma_{\mathrm{H_2O}})/dT = -10.36(30)\cdot 10^{-9}$ K^{-1} [89]. Combining the NMR frequency ratio above with $\mu_{^3\mathrm{He}}$ determined in this thesis yields a deviating shielding in H_2O at 25°C

$$\sigma_{\mathrm{H_2O}}(25°\mathrm{C}) = 1 - \left(\frac{\nu'_{^3\mathrm{He}}}{\nu'_{\mathrm{H_2O}}(25°\mathrm{C})}\right)^{-1} \frac{|\mu_{^3\mathrm{He}}|}{\mu_p} = 25.6686(44)\cdot 10^{-6}\,. \tag{6.41}$$

Furthermore, the ^{3}He NMR frequency was compared to that of protons in molecular hydrogen in [90]. In this experiment, a measurement of the NMR frequency ratio of ^{3}He to protons in HD

$$\nu'_{^3\mathrm{He}}/\nu'_{\mathrm{HD}} = 0.761\,786\,625(2) \tag{6.42}$$

is combined with the measured difference of the NMR frequencies of protons in HD to protons in H_2 to extract

$$\nu'_{^3\mathrm{He}}/\nu'_{\mathrm{H_2}} = 0.761\,786\,594(2)\,. \tag{6.43}$$

This is in the following compared to the ^{3}He magnetic moment $\mu_{^3\mathrm{He}}$ determined in this thesis by assuming either the experimental or theoretical shielding parameter in molecular hydrogen.

The difference of shielding parameters of protons in molecular hydrogen and in water was measured to be [10]

$$\Delta_\sigma(25°\mathrm{C}) = \sigma_{\mathrm{H_2}} - \sigma_{\mathrm{H_2O}}(25°\mathrm{C}) = 0.6080(15)\cdot 10^{-6}\,. \tag{6.44}$$

This can be combined with Eq. (6.43) to indirectly get the ^{3}He-to-water NMR ratio

$$R = \frac{\nu'_{^3\mathrm{He}}}{\nu'_{\mathrm{H_2}}}\frac{1-\sigma_{\mathrm{H_2}}}{1-\sigma_{\mathrm{H_2O}}(25°\mathrm{C})} = \frac{\nu'_{^3\mathrm{He}}}{\nu'_{\mathrm{H_2}}}\left(1-\Delta_\sigma(25°\mathrm{C})\right) = 0.761\,786\,130\,8(23), \tag{6.45}$$

which is consistent with the directly measured value (Eq. (6.40)). It therefore leads to a magnetic moment that is consistent with $\mu^{\mathrm{codata}}_{^3\mathrm{He}}$

$$\begin{aligned}\mu^{(1)}_{^3\mathrm{He}} &= -\mu_p(1-\sigma^{\mathrm{codata}}_{\mathrm{H_2O}})R \\ &= -1.074\,553\,089(12)\cdot 10^{-26}\ \mathrm{J\,T^{-1}}\end{aligned} \tag{6.46}$$

and deviates from the result in this thesis by 20 ppb with an uncertainty limited by the shielding in water. Assuming instead the theoretical shielding parameter in molecular hydrogen H_2 or HD leads to more precise values for the magnetic moment:

$$\begin{aligned}\mu^{(2)}_{^3\mathrm{He}} &= -\mu_p(1-\sigma^{theo}_{\mathrm{H_2}})\frac{\nu'_{^3\mathrm{He}}}{\nu'_{\mathrm{H_2}}} \\ &= -1.074\,553\,099\,0(36)\cdot 10^{-26}\ \mathrm{J\,T^{-1}}\,,\end{aligned} \tag{6.47}$$

$$\begin{aligned}\mu^{(3)}_{^3\mathrm{He}} &= -\mu_p(1-\sigma^{theo}_{\mathrm{HD}})\frac{\nu'_{^3\mathrm{He}}}{\nu'_{\mathrm{HD}}} \\ &= -1.074\,553\,094\,5(31)\cdot 10^{-26}\ \mathrm{J\,T^{-1}}. \end{aligned} \tag{6.48}$$

Here, the theoretical shielding parameters of protons in H_2 $\sigma^{theo}_{\mathrm{H_2}} = 26.288(2)\cdot 10^{-6}$ and protons in HD $\sigma^{theo}_{\mathrm{HD}} = 26.3329(12)\cdot 10^{-6}$ [91] were combined with the frequency ratios in Eq. (6.43) and Eq. (6.42), respectively. These values are shifted compared to $\mu^{\mathrm{codata}}_{^3\mathrm{He}}$ and deviate from the result determined in this thesis by 12 ppb in case of $\mu^{(2)}_{^3\mathrm{He}}$ and 17 ppb in case of $\mu^{(3)}_{^3\mathrm{He}}$. Here, the relative uncertainties of 3.4 ppb and 2.9 ppb are due to the frequency uncertainties in [90], while according to [63, 92] these uncertainties are underestimated by a factor of three because of the deviation of the assumed lineshape from the data.

The 21 ppb difference between the magnetic moment $\mu_{^3\mathrm{He}}$ determined in this thesis and the CODATA value would correspond to a shift of the nuclear resonance frequencies by three times the resonance width or alternatively a relative shift of the measured B-field by $\Delta B/B = 1.4\cdot 10^{-8}$. A systematic shift in the magnetic field measurements of this order of magnitude can be excluded as $\Delta B/B = 1.4\cdot 10^{-8}$ would result in a 29σ shift of g_e^{exp}, which, however, agrees with g_e^{theo}.

Chapter 7

Conclusion and Outlook

The three directly determined parameters are summarized and compared to theory or previous experiments in Tab. 7.1. The ground-state zero-field hyperfine splitting $E_{\mathrm{HFS}}^{\mathrm{exp}}$ is in agreement with the previous most precise measurement $-8\,665\,649\,867(10)$ Hz [25], while improving the precision by two orders of magnitude. Through comparison to theory it yields the Zemach radius

$$r_Z = 2.608(24)\ \mathrm{fm}\,. \tag{7.1}$$

With the calculated shielding parameters [11] follows the g-factor of $^3\mathrm{He}^{2+}$

$$g_I = -4.255\,250\,699\,9(30)_{stat}(17)_{sys} \tag{7.2}$$

with negligible theoretical uncertainty, as well as the magnetic moment that calibrates ^{3}He NMR probes

$$\mu_{^3\mathrm{He}} = -1.074\,553\,111\,92(93)\cdot 10^{-26}\ \mathrm{J\,T^{-1}}\,. \tag{7.3}$$

This result is one order of magnitude more precise than the most precise determination based on water NMR probes [9].

Table 7.1. Experimental results of the bound electron g-factor g_e and the zero-field hyperfine splitting E_{HFS} compared to the theoretical values from [39] and the only previously measured value of the hyperfine splitting [25]. Furthermore, the experimental result for the shielded nuclear g-factor is given and for comparison the CODATA2018 value of the bare g_I-factor corrected by the calculated shielding parameter of $^3\mathrm{He}^+$ [11].

	g_e	E_{HFS} (Hz)	g'_I
this work	-2.002 177 415 79(34)$_{stat}$(30)$_{sys}$	-8 665 649 865.77(26)$_{stat}$(1)$_{sys}$	-4.255 099 606 9(30)$_{stat}$(17)$_{sys}$
theo	-2.002 177 416 252 23(39)	-8 665 701(19)	
exp		-8 665 649 867(10) [25]	-4.255 099 522(50) [63]

The results for the bound electron g-factor as well as the shielded or bare nuclear g-factor are limited by the uncertainty of the resonance lineshape and could thus be improved by reducing the magnetic inhomogeneity in the PT. With optimized positioning of the trap in the superconducting magnet and no ferromagnetic components other than the AT ring electrode this parameter should be reduced to 0.1 $\mathrm{T\,m^{-2}}$ instead of 1.1 $\mathrm{T\,m^{-2}}$. Secondly, a more precise magnetic field measurement could be achieved by introducing phase-sensitive detection methods [93]. Attempts at this failed in the setup described in this thesis, likely because of the residual C_6 present in the five-polar PT due to the limited manufacturing precision. This can be fixed in the seven-polar PT implemented in the new setup that is currently in operation, as the additional pair of correction electrodes allows tuning C_6 independently of C_4. Thus the statistical and systematic uncertainties of $g_e m_{^3He^+}/m_e$, $g'_I m_{^3He^+}/m_p$ and E_{HFS} can be decreased by around one order of magnitude, where $m_{^3He^+}/m_p$ is known to 0.062 ppb. The current relative uncertainty of the measured g_e is 0.23 ppb, so that with such an improvement the mass ratio $m_{^3He^+}/m_e$ (0.043 ppb) would follow with improved precision from the electronic resonances via $g_e^{\mathrm{theo}} m_{^3He^+}/m_e$ in the Breit-Rabi equation. This would not, however, allow an improved determination of $m_{^3He^+}$ in atomic mass units at the current precision of m_e (29 ppt). Furthermore, $\mathrm{He^+}$ is the only hydrogen-like ion where uncertainties arising from nuclear structure are small enough to in principle enable an extraction of α from g_e with competitive precision [27]. This would require an independent and more precise value for $m_{^3He^+}/m_e$ as well as a further significant improvement of the experimental precision to the level of $\Delta g_e/g_e < 0.1$ ppt.

Currently, the measurement of the magnetic moment of the bare ^{3}He nucleus is realized in an altered setup designed to allow for direct detection of nuclear spin-flips with the continuous Stern-Gerlach effect. Besides increasing the axial frequency jump induced by nuclear spin-flips with a different analysis trap [22], sympathetic laser cooling with $^9\mathrm{Be^+}$ ions in a separate trap next to the PT will be implemented for the necessary axial frequency stability [21]. The latter also requires an improved liquid helium level and pressure stabilization [56] and is further optimized by a Josephson junction as voltage reference for the AT ring electrode. The experiment is aimed at determining the Larmor-to-cyclotron frequency ratio with a relative precision of 1 ppb or better. This ratio can be expressed as

$$\frac{\omega_L}{\omega_c} = \mu_{^3\mathrm{He}} \left(\frac{q\hbar}{2 m_{^3\mathrm{He}}} \right)^{-1}, \tag{7.4}$$

directly applicable in the muon g-2 experiment as described in chapter 1, or as

$$\frac{\omega_L}{\omega_c} = g_I \frac{m_{^3\mathrm{He}}}{4 m_p} \tag{7.5}$$

to extract the g-factor with the helion-proton-mass ratio known at 44 ppt [63]. Combined with the result presented in this thesis, the result g_I constitutes a test of the theoretical value of the shielding factor 1-$\sigma_{^3\mathrm{He}^+} = g_I'/g_I$ at ppb level. Furthermore, the methods developed for this purpose will allow for direct bare nuclear magnetic moment measurements of other nuclei heavier than protons.

List of Publications

1. A. Mooser, A. Rischka, **A. Schneider**, K. Blaum, S. Ulmer, and J. Walz. A New Experiment for the Measurement of the g-Factors of $^3He^+$ and $^3He^{2+}$. *Journal of Physics: Conference Series*, 1138, 012004, (2018).
   Cited as [21]

2. **A. Schneider**, A. Mooser, A. Rischka, K. Blaum, S. Ulmer, and J. Walz. A novel Penning-trap design for the high-precision measurement of the $^3He^{2+}$ nuclear magnetic moment. *Annalen der Physik*, 531(5), 1800485, (2019).
   Cited as [22]

3. **A. Schneider**, B. Sikora, M. Müller, N. S. Oreshkina, A. Rischka, I. A. Valuev, S. Ulmer, J. Walz, Z. Harman, C. H. Keitel, A. Mooser, and K. Blaum. Direct measurement of the $^3He^+$ magnetic moments. *To be published* (2022).
   Cited as [39]

Bibliography

[1] D. Hanneke, S. Fogwell, and G. Gabrielse. New measurement of the electron magnetic moment and the fine structure constant. *Phys. Rev. Lett.*, 100(12):120801, 2008.

[2] S. Sturm, A. Wagner, B. Schabinger, J. Zatorski, Z. Harman, W. Quint, G. Werth, C. H. Keitel, and K. Blaum. g-factor of hydrogenlike $^{28}Si^{13+}$. *Phys. Rev. Lett.*, 107(2):023002, 2011.

[3] R. S. Van Dyck Jr., P. B. Schwinberg, and H. G. Dehmelt. New high-precision comparison of electron and positron g factors. *Phys. Rev. Lett.*, 59(1):26–29, 1987.

[4] G. Schneider et al. Double-trap measurement of the proton magnetic moment at 0.3 parts per billion precision. *Science*, 358(6366):1081, 2017.

[5] C. Smorra et al. A parts-per-billion measurement of the antiproton magnetic moment. *Nature*, 550:371, 2017.

[6] T. R. Gentile, P. J. Nacher, B. Saam, and T. G. Walker. Optically polarized ^{3}He. *Rev. Mod. Phys.*, 89:045004, 2017.

[7] M. Farooq, T. Chupp, J. Grange, A. Tewsley-Booth, D. Flay, D. Kawall, N. Sachdeva, and P. Winter. Absolute magnetometry with ^{3}He. *Phys. Rev. Lett.*, 124:223001, 2020.

[8] A. Nikiel, P. Blümler, W. Heil, M. Hehn, S. Karpuk, A. Maul, E. Otten, L. M. Schreiber, and M. Terekhov. Ultrasensitive ^{3}He magnetometer for measurements of high magnetic fields. *Eur. Phys. J. D*, 68(11):330, 2014.

[9] J. L. Flowers, B. W. Petley, and M. G. Richards. A measurement of the nuclear magnetic moment of the helium-3 atom in terms of that of the proton. *Metrologia*, 30(2):75, 1993.

[10] Yu I. Neronov and N. N. Seregin. Precision determination of the difference in shielding by protons in water and hydrogen and an estimate of the absolute shielding by protons in water. *Metrologia*, 51(1):54, 2014.

[11] D. Wehrli, A. Spyszkiewicz-Kaczmarek, M. Puchalski, and K. Pachucki. QED Effect on the Nuclear Magnetic Shielding of ^{3}He. *Phys. Rev. Lett.*, 127:263001, 2021.

[12] G. Gabrielse, S. E. Fayer, T. G. Myers, and X. Fan. Towards an improved test of the Standard Model's most precise prediction. *Atoms*, 7(2), 2019.

[13] X. Fan, S. E. Fayer, and G. Gabrielse. Gaseous ^{3}He nuclear magnetic resonance probe for cryogenic environments. *Rev. Sci. Instrum.*, 90(8):083107, 2019.

[14] G. W. Bennett et al. Measurement of the negative muon anomalous magnetic moment to 0.7 ppm. *Phys. Rev. Lett.*, 92(16):161802, 2004.

[15] Hiromi Iinuma and J-PARC New g-2/EDM experiment collaboration. New approach to the Muon g–2 and EDM experiment at J–PARC. *J. Phys.: Conf. Ser.*, 295(1):012032, 2011.

[16] B. Abi et al. Measurement of the positive muon anomalous magnetic moment to 0.46 ppm. *Phys. Rev. Lett.*, 126:141801, 2021.

[17] G. W. Bennett et al. Final report of the E821 muon anomalous magnetic moment measurement at BNL. *Phys. Rev. D*, 73:072003, 2006.

[18] M. Abe, Y. Murata, H. Iinuma, T. Ogitsu, N. Saito, K. Sasaki, T. Mibe, and H. Nakayama. Magnetic design and method of a superconducting magnet for muon $g-2$/EDM precise measurements in a cylindrical volume with homogeneous magnetic field. *Nucl. Instrum. Methods Phys. Res. A*, 890:51, 2018.

[19] Matthias W. Smith. *Developing the Precision Magnetic Field for the E989 Muon $g-2$ Experiment*. PhD thesis, University of Washington, 2017.

[20] W. Liu et al. High precision measurements of the ground state hyperfine structure interval of muonium and of the muon magnetic moment. *Phys. Rev. Lett.*, 82(4):711, 1999.

[21] A. Mooser, A. Rischka, A. Schneider, K. Blaum, S. Ulmer, and J. Walz. A New Experiment for the Measurement of the g-Factors of ^{3}He$^+$ and ^{3}He^{2+}. *J. Phys. Conf. Ser.*, 1138:012004, 2018.

[22] A. Schneider, A. Mooser, A. Rischka, K. Blaum, S. Ulmer, and J. Walz. A novel Penning-trap design for the high-precision measurement of the ^{3}He^{2+} nuclear magnetic moment. *Annalen der Physik*, 531(5):1800485, 2019.

[23] S. L. Zafonte and R. S.Van Dyck Jr. Ultra-precise single-ion atomic mass measurements on deuterium and helium-3. *Metrologia*, 52(2):280, 2015.

[24] S. Sturm, F. Köhler, J. Zatorski, A. Wagner, Z. Harman, G. Werth, W. Quint, C. H. Keitel, and K. Blaum. High-precision measurement of the atomic mass of the electron. *Nature*, 506:467, 2014.

[25] H. A. Schüssler, E. N. Fortson, and H. G. Dehmelt. Hyperfine structure of the ground state of $^3He^+$ by the ion-storage exchange-collision technique. *Phys. Rev.*, 187(1):5–38, 1969.

[26] E. Fermi. Über die magnetischen Momente der Atomkerne. *Zeitschrift für Physik*, 60(5):320–333, 1930.

[27] J. Zatorski, B. Sikora, S. G. Karshenboim, S. Sturm, F. Köhler-Langes, K. Blaum, C. H. Keitel, and Z. Harman. Extraction of the electron mass from g-factor measurements on light hydrogenlike ions. *Phys. Rev. A*, 96:012502, 2017.

[28] G. Gabrielse. Why is sideband mass spectrometry possible with ions in a Penning trap? *Phys. Rev. Lett.*, 102:172501, 2009.

[29] G. Gabrielse, L. Haarsma, and S.L. Rolston. Open-endcap penning traps for high precision experiments. *Int. J. Mass Spectrom.*, 88(2):319–332, 1989.

[30] J. Ketter, T. Eronen, M. Höcker, S. Streubel, and K. Blaum. First-order perturbative calculation of the frequency-shifts caused by static cylindrically-symmetric electric and magnetic imperfections of a Penning trap. *Int. J. Mass Spectrom.*, 358:1–16, 2014.

[31] Stefan Ulmer. *First Observation of Spin Flips with a Single Proton Stored in a Cryogenic Penning Trap*. PhD thesis, Ruperto-Carola University of Heidelberg, 2011.

[32] E. A. Cornell, R. M. Weisskoff, K. R. Boyce, and D. E. Pritchard. Mode coupling in a Penning trap: π pulses and a classical avoided crossing. *Phys. Rev. A*, 41:312–315, 1990.

[33] L. S. Brown and G. Gabrielse. Geonium theory: Physics of a single electron or ion in a Penning trap. *Rev. Mod. Phys.*, 58(1):233, 1986.

[34] H. G. Dehmelt. Continuous Stern-Gerlach effect: Principle and idealized apparatus. *Proc. Natl. Acad. Sci. USA*, 83(3):2291–2294, 1986.

[35] H. Häffner, T. Beier, N. Hermanspahn, H.-J. Kluge, W. Quint, S. Stahl, J. Verdú, and G. Werth. High-accuracy measurement of the magnetic moment anomaly of the electron bound in hydrogenlike carbon. *Phys. Rev. Lett.*, 85:5308–5311, 2000.

[36] W. Nagourney H. Dehmelt and J. Sandberg. Self-excited mono-ion oscillator. *Proc. Natl. Acad. Sci.*, 83:5761–5763, 1986.

[37] B. D'Urso, B. Odom, and G. Gabrielse. Feedback cooling of a one-electron oscillator. *Phys. Rev. Lett.*, 90:043001, 2003.

[38] R. P. Feynman, R. B. Leighton, and M. Sands. *The Feynman Lectures on Physics, Vol. III: The New Millennium Edition: Quantum Mechanics*. The Feynman Lectures on Physics. Basic Books, 2011.

[39] A. Schneider, B. Sikora, M. Müller, N. S. Oreshkina, A. Rischka, I. A. Valuev, S. Ulmer, J. Walz, Z. Harman, C. H. Keitel, A. Mooser, and K. Blaum. Direct measurement of the $^3He^+$ magnetic moments. 2022.

[40] D. L. Moskovkin and V. M. Shabaev. Zeeman effect of the hyperfine-structure levels in hydrogenlike ions. *Phys. Rev. A*, 73:052506, 2006.

[41] Stefan Dickopf. Design, installation and characterisation of a microwave transmission line for driving the transitions of the $^3He^+$ hyperfine structure in a Penning trap. Master's thesis, University of Heidelberg, 2020.

[42] H. Nagahama et al. Sixfold improved single particle measurement of the magnetic moment of the antiproton. *Nat. Commun.*, 8:14084, 2017.

[43] T. A. Savard, K. M. O'Hara, and J. E. Thomas. Laser-noise-induced heating in far-off resonance optical traps. *Phys. Rev. A*, 56(2):R1095, 1997.

[44] M. Bohman et al. Sympathetic cooling of protons and antiprotons with a common endcap Penning trap. *J. Mod. Opt.*, 65(5-6):568–576, 2018.

[45] Lowell S. Brown. Geonium lineshape. *Annals of Physics*, 159(1):62–98, 1985.

[46] J. L. Verdu Galiana. *Ultrapräzise Messung des elektronischen g-Faktors in wasserstoffähnlichem Sauerstoff*. PhD thesis, Johannes Gutenberg-Universität Mainz, Germany, 2004.

[47] S. Sellner et al. Improved limit on the directly measured antiproton lifetime. *New J. Phys.*, 19(8):083023, 2017.

[48] Jacob Maria Berner. Design einer Abschirmspule zur Minimierung äußerer Magnetfeldeinflüsse bei Präzisions-Penningfallen-Experimenten. Bachelor's thesis, University of Heidelberg, 2020.

[49] Cricia de Carvalho Rodegheri. *Neuartige kryogene* Penning-*Falle fuer den Nachweis von Spin-Uebergängen eines Protons und Bestimmung seines g-Faktors*. PhD thesis, Johannes Gutenberg-Universitaet Mainz, 2013.

[50] Antonia Schneider. Design of the Analysis Trap and He Ion Source for the $^3He^{2+}$ magnetic moment measurement. Master's thesis, University of Heidelberg, 2019.

[51] D. E. Swets, R. W. Lee, and R. C. Frank. Diffusion coefficients of helium in fused quartz. *J. Chem. Phys.*, 34(1):17–22, 1961.

[52] Francis J. Norton. Permeation of gases through solids. *J. Appl. Phys.*, 28(1):34–39, 1957.

[53] M. Redshaw, A. Benjamin, G. Bollen, R. Ferrer, D. Lincoln, R. Ringle, S. Schwarz, and A. Valverde. Fabrication and characterization of field emission points for ion production in penning trap applications. *Int. J. Mass Spectrom.*, 379, 2015.

[54] R. Rejoub, B. G. Lindsay, and R. F. Stebbings. Determination of the absolute partial and total cross sections for electron-impact ionization of the rare gases. *Phys. Rev. A*, 65:042713, 2002.

[55] M. B. Shah, D. S. Elliott, P. McCallion, and H. B. Gilbody. Single and double ionisation of helium by electron impact. *J. Phys. B*, 21(15):2751–2761, 1988.

[56] Maris Müller. Design and implementation of a non-destructive ion detection system for the ^3He g-factor experiment. Master's thesis, University of Heidelberg, 2020.

[57] Holger Kracke. Entwicklung der kryogenen Nachweis-Elektronik zur Bestimmung der axialen Frequenz des Protons in einer Penning-Falle. Diploma thesis, Johannes Gutenberg-University Mainz, 2007.

[58] Mustafa Besirli. Development of Single Sideband Down Converters for Precise Measurements of the Axial Frequency of a Single Trapped Antiproton. Bachelor's thesis, Sabanci University, 2016.

[59] Sascha Rau. *High-precision measurement of the deuteron's atomic mass*. PhD thesis, Ruperto-Carola University of Heidelberg, Germany, 2020.

[60] K. Jackowski, M. Jaszunski, and M. Wilczek. Alternative approach to the standardization of nmr spectra. direct measurement of nuclear magnetic shielding in molecules. *J. Phys. Chem. A*, 114(7):2471, 2010.

[61] Savely G. Karshenboim. Precision physics of simple atoms: QED tests, nuclear structure and fundamental constants. *Phys. Rep.*, 422(1):1–63, 2005.

[62] H. A. Schuessler, E. N. Fortson, and H. G. Dehmelt. Hyperfine Structure of the Ground State of $^3He^+$ by the Ion-Storage Exchange-Collision Technique. *Phys. Rev.*, 187:5–38, 1969.

[63] E. Tiesinga, P. J. Mohr, D. B. Newell, and B. N. Taylor. CODATA recommended values of the fundamental physical constants: 2018. *Rev. Mod. Phys.*, 93:025010, 2021.

[64] F. Heiße et al. High-precision measurement of the proton's atomic mass. *Phys. Rev. Lett.*, 119:033001, 2017.

[65] M. Wang, W. J. Huang, F. G. Kondev, G. Audi, and S. Naimi. The AME2020 atomic mass evaluation (II). Tables, graphs and references. *Chin. Phys. C*, 45(3):030003, 2021.

[66] D. C. Morton, Q. Wu, and G. Drake. Energy levels for the stable isotopes of atomic helium (^{4}He I and ^{3}He I). *Can. J. Phys.*, 84(2):83–105, 2006.

[67] H. Häffner. *Präzisionsmessung des magnetischen Moments des Elektrons in wasserstoffähnlichem Kohlenstoff*. PhD thesis, Johannes Gutenberg-Universität Mainz, Germany, 2000.

[68] S. Sturm. *The g-factor of the electron bound in $^{28}Si^{13+}$: The most stringent test of bound-state quantum electrodynamics*. PhD thesis, Johannes Gutenberg-Universität Mainz, Germany, 2011.

[69] Gregory Breit. The magnetic moment of the electron. *Nature*, 122:649–649, 1928.

[70] H. Grotch. Electron g factor in hydrogenic atoms. *Phys. Rev. Lett.*, 24(2):39–42, 1970.

[71] A. Czarnecki, K. Melnikov, and A. Yelkhovsky. Anomalous magnetic moment of a bound electron. *Phys. Rev. A*, 63:012509, 2000.

[72] K. Pachucki, U. D. Jentschura, and V. A. Yerokhin. Nonrelativistic QED Approach to the Bound-Electron g Factor. *Phys. Rev. Lett.*, 93(15):150401, 2004.

[73] K. Pachucki, A. Czarnecki, U. D. Jentschura, and V. A. Yerokhin. Complete two-loop correction to the bound-electron g factor. *Phys. Rev. A*, 72:022108, 2005.

[74] Thomas Beier. The g_j factor of a bound electron and the hyperfine structure splitting in hydrogenlike ions. *Phys. Rep.*, 339(2-3):79 – 213, 2000.

[75] V. M. Shabaev. Hyperfine structure of hydrogen-like ions. *J. Phys. B*, 27(24):5825–5832, 1994.

[76] A. V. Volotka, V. M. Shabaev, G. Plunien, and G. Soff. Nuclear size correction to the hyperfine splitting in low-Z hydrogen-like atoms. *Eur. Phys. J. D*, 23(1):51–56, 2003.

[77] Andrey V. Volotka. *High-precision QED calculations of the hyperfine structure in hydrogen and transition rates in multicharged ions*. PhD thesis, Technische Universität Dresden, 2006.

[78] A. C. Zemach. Proton structure and the hyperfine shift in hydrogen. *Phys. Rev.*, 104:1771–1781, 1956.

[79] Ingo Sick. Zemach moments of ^{3}He and ^{4}He. *Phys. Rev. C*, 90:064002, 2014.

[80] J.J. Krauth, K. Schuhmann, M. A. Ahmed, et al. Measuring the α-particle charge radius with muonic helium-4 ions. *Nature*, 589:527—531, 2021.

[81] D. Shiner, R. Dixson, and V. Vedantham. Three-nucleon charge radius: A precise laser determination using ^{3}He. *Phys. Rev. Lett.*, 74:3553–3556, 1995.

[82] R. van Rooij, J. S. Borbely, J. Simonet, M. D. Hoogerland, K. S. E. Eikema, R. A. Rozendaal, and W. Vassen. Frequency metrology in quantum degenerate helium: Direct measurement of the $2^3\mathrm{S}_1 \rightarrow 2^1\mathrm{S}_0$ transition. *Science*, 333(6039):196–198, 2011.

[83] X. Zheng, Y. R. Sun, J.-J. Chen, W. Jiang, K. Pachucki, and S.-M. Hu. Measurement of the Frequency of the $2\ ^3S - 2\ ^3P$ Transition of ^{4}He. *Phys. Rev. Lett.*, 119:263002, 2017.

[84] K. Pachucki, V. Patkóš, and V. A. Yerokhin. Testing fundamental interactions on the helium atom. *Phys. Rev. A*, 95:062510, 2017.

[85] J. L. Friar and G. L. Payne. Nuclear corrections to hyperfine structure in light hydrogenic atoms. *Phys. Rev. C*, 72:014002, 2005.

[86] S. G. Karshenboim and V. G. Ivanov. Hyperfine structure in hydrogen and helium ion. *Phys. Lett. B*, 524(3):259 – 264, 2002.

[87] A. Rudzinski, M. Puchalski, and K. Pachucki. Relativistic, QED, and nuclear mass effects in the magnetic shielding of ^{3}He. *J. Chem. Phys.*, 130(24):244102, 2009.

[88] W. D. Phillips, W. E. Cooke, and D. Kleppner. Magnetic Moment of the Proton in H_2O in Bohr Magnetons. *Metrologia*, 13(4):179–195, 1977.

[89] P. W. Petley and R. W. Donaldson. The Temperature Dependence of the Diamagnetic Shielding Correction for Proton NMR in Water. *Metrologia*, 20:81–83, 1984.

[90] Yu I. Neronov and N. N. Seregin. High-precision evaluation of the magnetic moment of the helion. *Metrologia*, 115(5):777–781, 2012.

[91] D. Sundholm and J. Gauss. Isotope and temperature effects on nuclear magnetic shieldings and spin-rotation constants calculated at the coupled-cluster level. *Molecular Physics*, 92(6):1007, 1997.

[92] P. J. Mohr, D. B. Newell, and B. N. Taylor. CODATA recommended values of the fundamental physical constants: 2014*. *Rev. Mod. Phys.*, 88:035009, 2016.

[93] S. Rau, F. Heiße, F. Köhler-Langes, S. Sasidharan, R. Haas, D. Renisch, C. Duellmann, W. Quint, S. Sturm, and K. Blaum. Penning trap mass measurements of the deuteron and the HD^+ molecular ion. *Nature*, 585:43–47, 2020.

Appendix A

Resonance curves

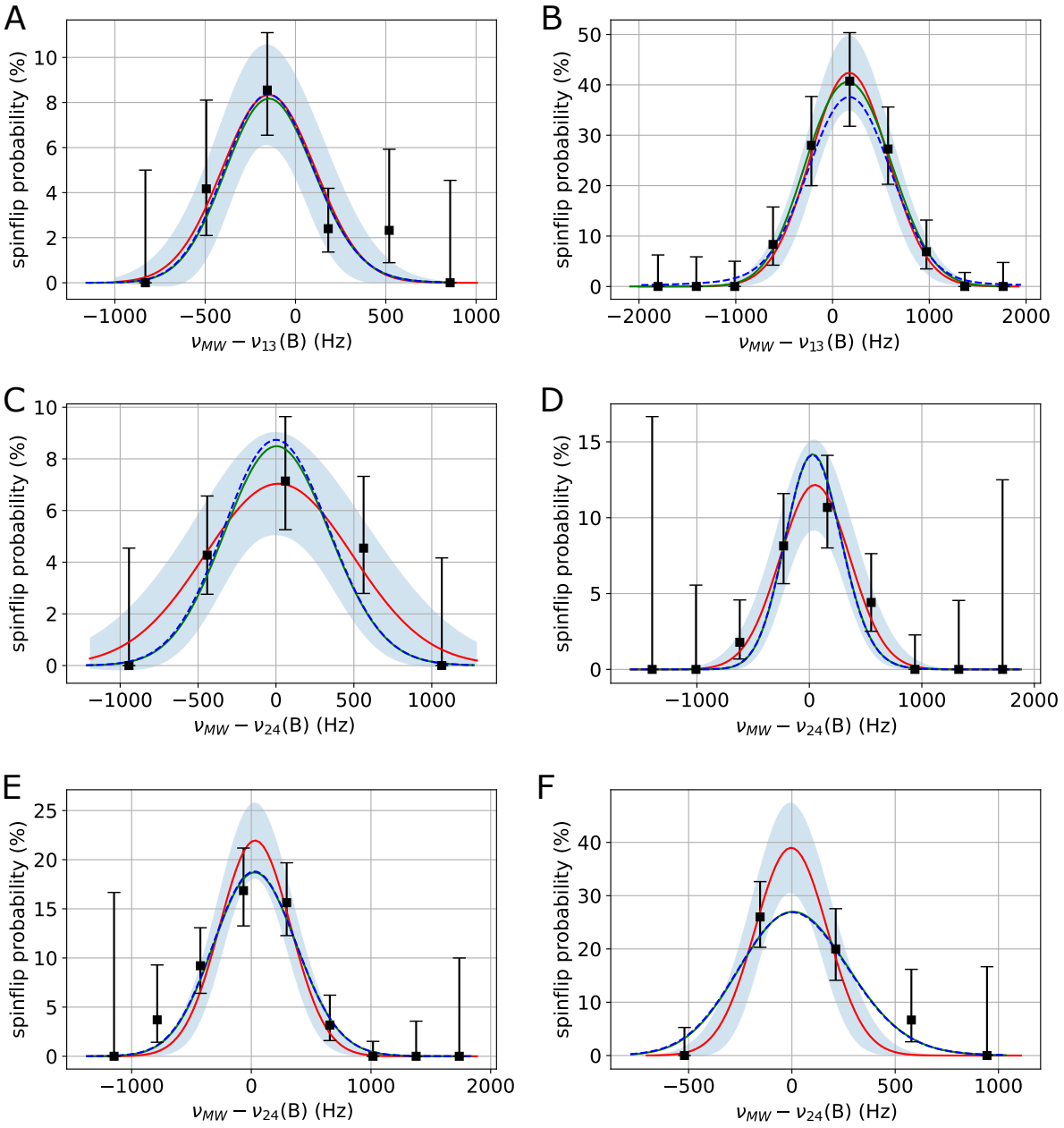

Figure A.1. Electronic transition resonance resonance curves with fitted lines assuming a Gaussian (Red line) or lineshape models $\tilde{P}_1$ (Green line), $\tilde{P}_2$ (Blue dashed line), compare Eq. (3.23). The shaded area indicates the 1σ interval of the Gaussian line parameters. (A) and (B): transition $|1\rangle \leftrightarrow |3\rangle$. (C)-(F): transition $|2\rangle \leftrightarrow |4\rangle$ at increasing Rabi frequencies.

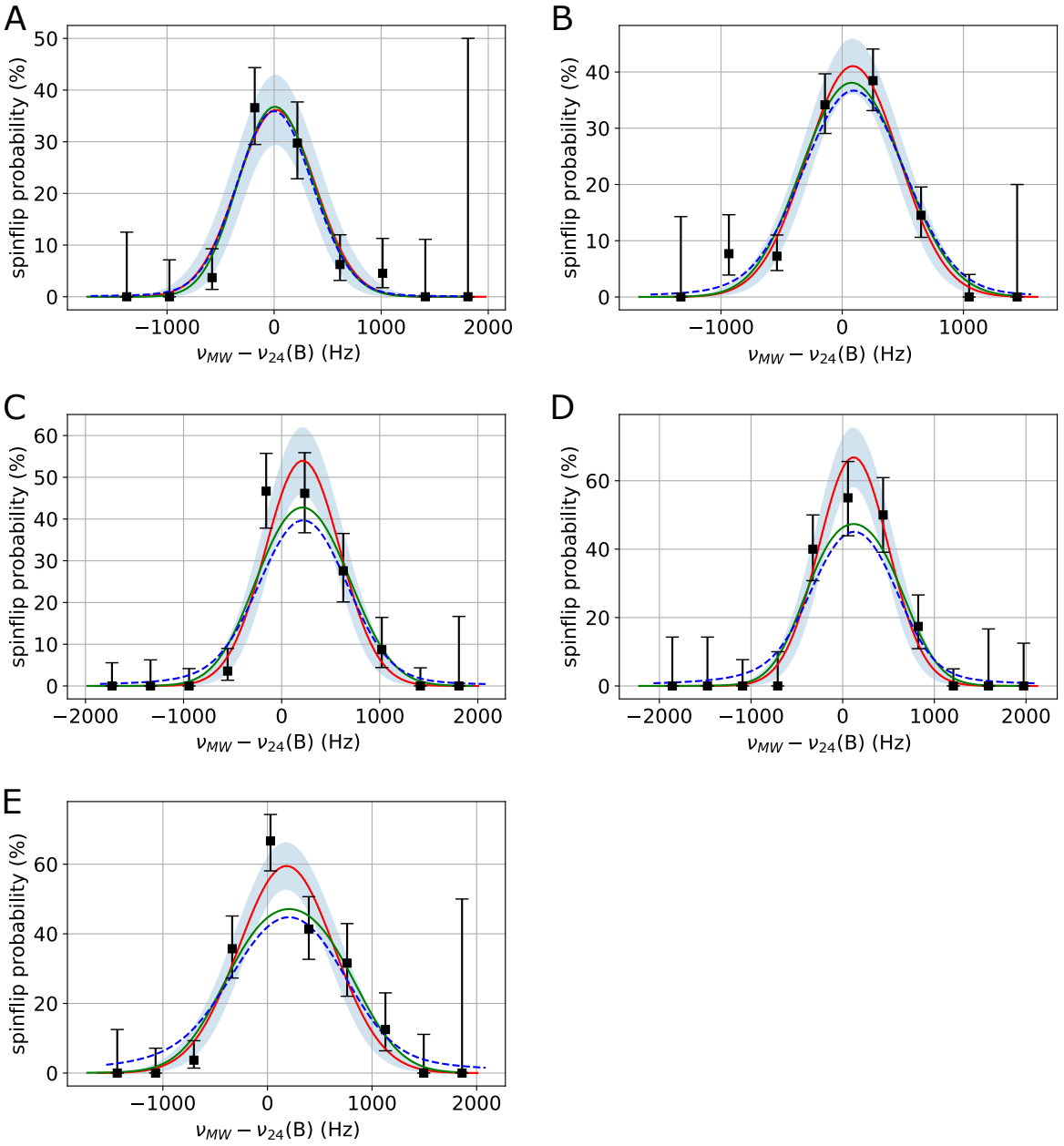

Figure A.2. Resonance curves of transition $|2\rangle \leftrightarrow |4\rangle$ at increasing Rabi frequencies with fitted lines assuming a Gaussian (Red line) or lineshape models $\tilde{P}_1$ (Green line), $\tilde{P}_2$ (Blue dashed line), compare Eq. (3.23). The shaded area indicates the 1σ interval of the Gaussian line parameters.

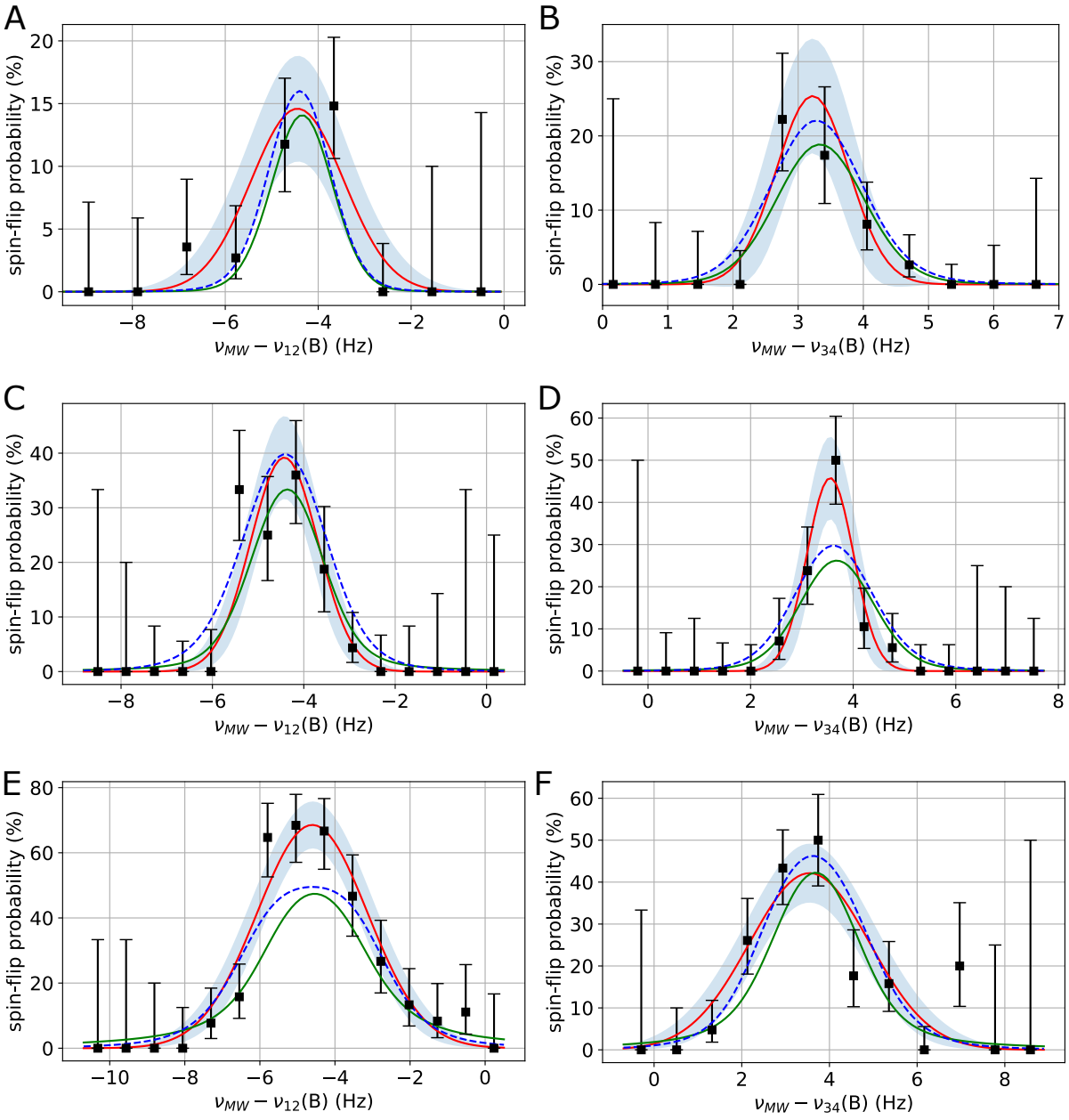

Figure A.3. Resonance curves the of nuclear transitions $|1\rangle \leftrightarrow |2\rangle$ (A, C, E) and $|3\rangle \leftrightarrow |4\rangle$ (B, D, F) at increasing Rabi frequencies with fitted lines assuming a Gaussian (Red line) or lineshape models $\tilde{P}_1$ (Green line), $\tilde{P}_2$ (Blue dashed line), compare Eq. (3.23). The shaded area indicates the 1σ interval of the Gaussian line parameters.